

*Non-invasive assessment of human brown adipose tissue
Development of robust imaging methods to facilitate clinical translation*

Aashley Sardjoe Mishre

Non-invasive assessment of human brown adipose tissue

Development of robust imaging methods to facilitate clinical translation

Aashley Sardjoe Mishre

Non-invasive assessment of human brown adipose tissue

Development of robust imaging methods to facilitate clinical translation

Proefschrift

ter verkrijging van

de graad van doctor aan de Universiteit Leiden,

op gezag van rector magnificus prof.dr.ir. H. Bijl,

volgens besluit van het college voor promoties

te verdedigen op dinsdag 5 september 2023

klokke 15.00 uur

door

Aashley Sardjoe Mishre

Non-invasive assessment of human brown adipose tissue

Development of robust imaging methods to facilitate clinical translation

DISSERTATION

to obtain the degree of Doctor at the Leiden University,
on the authority of the Rector Magnificus, Prof. dr. Hester Bijl
in accordance with the decision of the Board of Deans,

to be defended in public

on September 5, 2023 at 15.00 hours

by

Aashley Sardjoe Mishre

Promotores:

Prof. dr. A.G. Webb

Prof. dr. P.C.N. Rensen

Co-promotor:

Dr. H.E. Kan

Leden promotiecommissie:

Prof. dr. M. Staring

Prof. dr. L.F. de Geus-Oei

Prof. dr. V.B. Schrauwen-Hinderling

Maastricht University Medical Center, Maastricht, The Netherlands

Dr. M. Savas

Erasmus MC, University Medical Center Rotterdam, Rotterdam, The Netherlands

Supervisor

Prof. dr. Andrew Webb

Prof. dr. Patrick Rensen

Co-supervisors

Dr. Hermien Kan

Assessment Committee

Prof. dr. Marius Staring (chairman)

Prof. dr. Lioe-Fee de Geus-Oei

Prof. dr. Vera Schrauwen-Hinderling

Dr. Mesut Savas

TABLE OF CONTENTS

Chapter 1	General introduction	7
Chapter 2	Association of shivering threshold time with body composition and brown adipose tissue in young adults <i>Sardjoe Mishre ASD*, Martinez-Tellez B*, Acosta FM, Sanchez-Delgado G, Straat ME, Webb AG, Kan HE, Rensen PCN, Ruiz JR Journal of Thermal Biology (2022) Doi: 10.1016/j.jtherbio.2022.103277</i>	19
Chapter 3	The infrared thermography toolbox: an open-access semi-automated segmentation tool for extracting thoracic skin temperatures including supraclavicular brown adipose tissue <i>Sardjoe Mishre ASD, Straat ME, Martinez-Tellez B, Mendez Gutierrez A, Kooijman S, Boon MR, Dzyubachyk O, Webb AG, Rensen PCN, Kan HE Journal of Medical Systems (2022) Doi: 10.1007/s10916-022-01871-7</i>	41
Chapter 4	Human brown adipose tissue estimated with magnetic resonance imaging undergoes changes in composition after cold exposure: an in vivo MRI study in healthy volunteers <i>Abreu-Vieira G*, Sardjoe Mishre ASD*, Burakiewicz J, Janssen LGM, Nahon KJ, van der Eijk AJ, Riem TT, Boon MR, Dzyubachyk O, Webb AG, Rensen PCN, Kan HE Frontiers in Endocrinology (2020) Doi: 10.3389/fendo.2019.00898</i>	59
Chapter 5	Image registration and mutual thresholding enable low inter-image variability across dynamic MRI measurements of supraclavicular brown adipose tissue during mild-cold exposure <i>Sardjoe Mishre ASD, Martinez-Tellez B, Straat ME, Boon MR, Dzyubachyk O, Webb AG, Rensen PCN, Kan HE. Submitted for publication</i> <i>*contributed equally</i>	93
Chapter 6	Summary, general discussion and future perspectives	111
Chapter 7	List of abbreviations	124
	Nederlandse samenvatting	125
	List of publications	130
	Curriculum vitae	132
	Dankwoord	133



Chapter 1

General introduction



Historically, the primary function of brown adipose tissue (BAT) was thought to be to maintain core body temperature in infants and hibernating mammals. In 2009, it was discovered that BAT is still present, and is functionally active during adulthood¹⁻³. Since then, the presence of metabolically active BAT in human adults has been irrefutably confirmed. Reports from preclinical- and clinical studies have shown that enhanced BAT activity, as assessed with [¹⁸F]fluorodeoxyglucose PET-CT scans relates to insulin sensitivity and inversely relates to cardiovascular events⁴⁻⁸, which hold promise for future treatment strategies against obesity and cardiometabolic diseases. Non-invasive methods to determine the activity of human BAT are under constant development. This thesis focusses on the improvement of non-invasive methods for BAT detection to facilitate research on treatment strategies (in)directly targeting BAT.

1.1 BROWN ADIPOSE TISSUE PHYSIOLOGY AND MORPHOLOGY

In mammals, there are two main types of adipose tissue: BAT and white adipose tissue (WAT), that each have their own physiology, morphology and function. The main function of WAT is energy storage, and as a result, white adipocytes contain a single large lipid droplet. In contrast, the main function of BAT is to regulate core body temperature by converting chemical energy stored in glucose and lipids into heat. To facilitate this, BAT contains numerous smaller lipid droplets. In addition, BAT has a high abundance of mitochondria and uncoupling protein (UCP)-1 expression and is more vascularized and innervated compared to WAT⁹. Cold exposure stimulates cation channels in the skin, which stimulate afferent nerves that transfer the cold perception to the hypothalamic temperature regulation center¹⁰. Once the signal is received by the hypothalamus, via efferent sympathetic outflow, norepinephrine is released from nerve endings in BAT. Norepinephrine subsequently binds to β -adrenergic receptors that are located on the cell surface of brown adipocytes, which induces a signaling cascade via the messenger cyclic adenosine monophosphate (cAMP) that, via protein kinase A (PKA) activation, promotes the hydrolysis of triglycerides within the lipid droplets to liberate fatty acids¹¹. These fatty acids then enter the mitochondria where they are broken down by β -oxidation into substrates to enter the citric acid cycle. This activates the electron transport chain to induce a proton gradient across the inner membrane of mitochondria, which in most tissues is used to drive the synthesis of adenosine triphosphate (ATP) via complex V. In BAT, the uncoupling protein (UCP-1) dissipates the proton gradient to generate heat instead of ATP by forming a pore in the inner mitochondrial membrane resulting in release of energy as heat. Subsequently, intracellular lipids are replenished by extracting fatty acids and glucose from the systemic circulation via cluster of differentiation protein 36 (CD36) and fatty acid transport protein (FATP), and glucose transporters (GLUT 1 and 4), respectively^{12,13}.

The extracted glucose is amongst others used for the synthesis of fatty acids, which is referred to as de novo lipogenesis. A schematic representation of human BAT physiology is presented in Fig. 1. In infants, brown adipocytes are clustered and mostly separated from white adipocytes. In adults, brown adipocytes are dispersed in WAT, making the depot much more heterogeneous in composition. The average amount of BAT volume in human adults is 50-150 mL¹⁴. BAT depots are typically located in the deep cervical, supraclavicular, supra-aortic and perirenal regions, with the supraclavicular BAT depot (scBAT) being the largest BAT depot in human adults (**Fig. 1**).

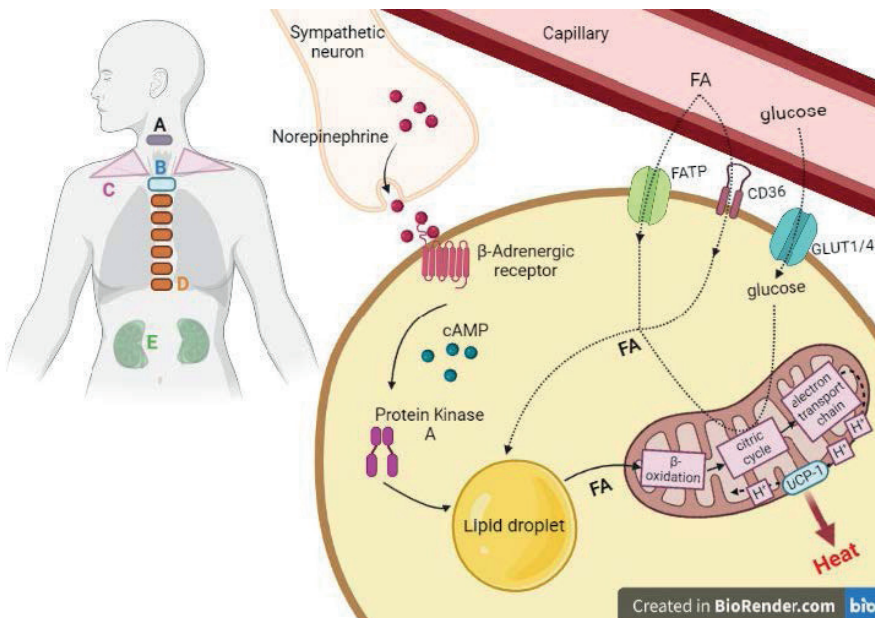


Figure 1. A schematic representation of brown adipose tissue (BAT) morphology and physiology.

Human BAT is located in (A) cervical, (B) supra-aortic, (C) supraclavicular, (D) paravertebral and (E) perirenal areas. Adrenergic stimulation of brown adipocytes by norepinephrine leads to intracellular lipolysis via the messenger cyclic adenosine monophosphate (cAMP) that activates protein kinase A (PKA). Liberated fatty acids subsequently enter the mitochondria where they are broken down by β -oxidation into substrates to enter the citric acid cycle and activate the electron transport chain to generate a proton gradient over the inner mitochondrial membrane. The uncoupling protein (UCP-1), uniquely present in BAT, increases the conductance of the inner mitochondrial membrane, which diverts the proton gradient from adenosine triphosphate (ATP) synthesis to generation of heat. Subsequently, intracellular lipids are replenished by extracting fatty acids and glucose from the bloodstream via cluster of differentiation protein 36 (CD36) and fatty acid transport protein (FATP), and glucose transporters (GLUT 1 and 4), respectively.

1.2 IMAGING MODALITIES FOR THE ASSESSMENT OF BROWN ADIPOSE TISSUE ACTIVITY

Since BAT is activated by the sympathetic nervous system, plasma norepinephrine levels in blood have been used as a proxy of BAT activation¹⁵. The cold-induced change in resting energy expenditure (Δ REE), up to the shivering temperature, has been used as another measure of the thermogenic BAT response¹⁶⁻¹⁸, where REE is defined as the amount of energy an individual uses for maintaining essential body functions at rest. These methods, however, estimate BAT on whole-body level, and are less sensitive to assess changes in the BAT depot. Imaging methods that assess properties of BAT directly could solve this issue.

The most commonly used imaging technique to assess BAT activity is by quantifying the glucose uptake of a radioactively-labelled glucose analog, [¹⁸F]fluorodeoxyglucose (FDG), using positron emission tomography/computed tomography (PET-CT)¹⁹ in the supraclavicular area (scBAT). However, this imaging modality is invasive and depends on harmful radiation, which increases the participation burden and hampers longitudinal studies. In addition, BAT is an insulin sensitive organ, and since [¹⁸F]FDG-PET-CT relies on quantifying the glucose uptake, this technique could produce unreliable measurements of scBAT activity in individuals who are insulin resistant. Moreover, it has been shown that BAT predominantly combusts fatty acids rather than glucose during cold exposure²⁰.

Safer and non-invasive alternatives have been explored for the assessment of scBAT activity. For instance, infrared thermography (IRT) is an imaging technique that converts emitted infrared energy from an object into a two-dimensional surface temperature map²¹. Since heat is generated by BAT, IRT has been used for assessing skin temperature changes near the scBAT depot²²⁻²⁵. Although IRT is readily available and cheaper compared to PET-CT, it only quantifies surface temperatures, such that changes inside the scBAT depot cannot be assessed. In addition, IRT could produce misleading results in obese subjects as the amount of subcutaneous fat in the area of interest influences this read-out²⁶.

Alternatively, magnetic resonance imaging (MRI) is increasingly being used for estimating scBAT activity *in vivo* using sequences such as Dixon's method for quantitative fat fraction (FF) mapping^{27,28}. MRI produces images, which map the distribution of hydrogen-containing molecules, predominantly water and lipid. The hydrogen nuclei in lipid and water precess at slightly different frequencies ($Df = 440$ Hz on a 3 Tesla scanner). This can be detected as a difference in the phase ($D\phi$) of the detected MRI signals from water and fat,

$$Df = 2\pi\Delta f\tau$$

1

where τ is the time at which the signal is measured. For example, in a 2-point Dixon sequence, two MR images are acquired, one in which water and fat signals are in-phase at $\theta = k\pi$, where k is an even integer, and the other out-of-phase where k is an odd integer. Water and fat signals can then theoretically be produced by addition and subtraction from these in-and out-of-phase images²⁹. However, in practice there are several other factors which need to be considered, including non-uniformities in the main magnetic field (which by themselves cause spatially-dependent phase differences) and noise. In order to account for these factors, multi-point Dixon sequences are run, in which more than two images are acquired at different τ values. Since the magnitude of each signal is proportional to $\exp(-t/T2^*)$, where $T2^*$ is a characteristic relaxation time related to tissue structure and magnetic field homogeneity, there is a limit to how many time points are acquired in practice for the best fitting to be performed. Iterative methods are used to estimate each of the parameters, water fraction, fat fraction, static field homogeneity and $T2^*$. Finally, quantitative fat fraction (FF) maps are produced on a pixel-by-pixel basis. An example of images that can be obtained with the three imaging modalities: [¹⁸F]FDG-PET-CT, IRT and MRI are visualized in **Fig. 2A-C** in three different participants.

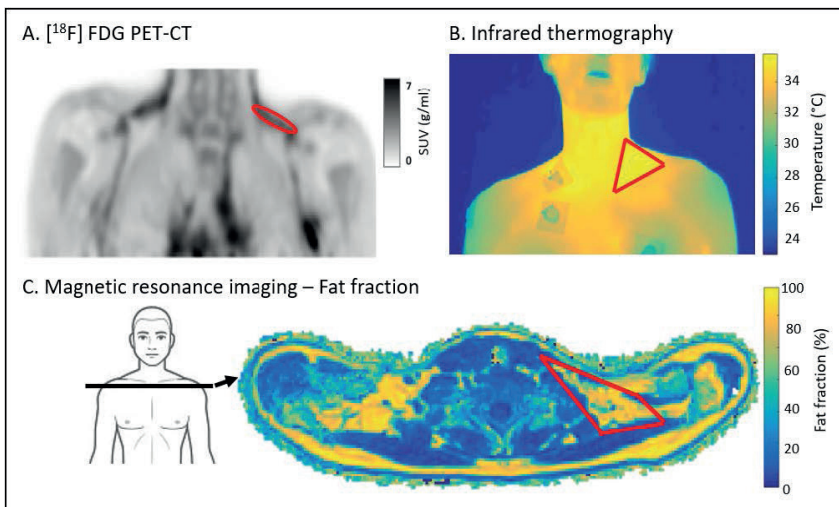


Figure 2. Examples of imaging modalities for assessing supraclavicular BAT activity.

A) [¹⁸F]FDG-PET-CT indirectly quantifies metabolic scBAT activity based on the glucose uptake. B) Infrared thermography is used to assess changes in supraclavicular skin temperature. C) Magnetic resonance imaging using fat fraction mapping estimates scBAT activity based on changes in the relative fat content. Regions of interest (ROIs) are drawn in the scBAT area and shown in red. A different participant is shown for each technique. SUV, standardized uptake value.

1.3 CURRENT CHALLENGE FOR BROWN ADIPOSE TISSUE ACTIVATION

Cold exposure is the main physiological activator of BAT³⁰. Different cooling protocols have been used in previous studies³¹, which differ by duration, intensity, medium (i.e., water or air), garment and strategy (i.e., personalized or standardized). In standardized cooling protocols, the temperature is kept constant at a pre-determined value for a certain duration. In personalized cooling protocols, the temperature is gradually lowered and individualized to some participants' features, such as the onset of shivering or skin temperature. In addition to cold exposure, several pharmacological strategies have been evaluated for targeting BAT. For instance, Mirabegron, a drug used to treat overactive bladder, increases metabolic BAT activity, as assessed with [¹⁸F]FDG PET-CT, while increasing resting energy expenditure^{16,32}. Likewise, Exenatide and Spironolactone increase [¹⁸F]FDG uptake by BAT after treatment^{32,33}

It is important that the activation strategy sufficiently invokes the thermogenic BAT response since BAT can only be measured when it is metabolically activated. Despite the variety of cooling protocols used, there is no optimized procedure to activate BAT. Ideally, a cooling procedure should invoke a similar cold perception among individuals with different phenotypical features (e.g., sex, body size and composition), thereby ensuring maximal BAT stimulation. It has been shown that large individuals characterized by a small body surface area to volume ratio can preserve more heat compared to small individuals³⁴. Moreover, individuals characterized by a higher fat mass and/or skeletal muscle mass could insulate heat better or produce more heat, respectively^{35–37}. Currently, limited research focuses on the physiological mechanisms that drive the human cold tolerance capacity, which is defined as the ability to withstand cold temperatures. This hampers the optimization and standardization of cooling protocols among different research centers.

1.4 CURRENT CHALLENGES FOR QUANTIFYING BROWN ADIPOSE TISSUE ACTIVITY

While non-invasive and safe imaging modalities such as MRI and IRT are increasingly used to measure scBAT activity in humans, there are several technical challenges that need to be addressed before translating these techniques into clinical research. One of these challenges is the presence of motion. For instance, when moderate displacement is present within a repeated dataset consisting of e.g., baseline and follow-up images, regions of interest (ROIs) (**Fig. 1A**) need to be delineated on each image for analysis. This can be very time-consuming, and results can be variable due to differences in ROI sizes and manual ROI placement.

Moreover, recent MRI studies have used dynamic protocols where multiple MR scans were acquired during one session to detect scBAT FF changes during cooling^{17,38,39}. Since scBAT is located in the supraclavicular area, and thus prone to motion-induced artefacts, results may be more variable. The influence of motion on the analysis time and data variability could be minimized by using non-rigid image registration. This technique enables a stepwise deformation of a target image towards a reference image to ensure a full image overlap⁴⁰. Correct delineation of the active scBAT area is another challenge in the assessment of scBAT activity. Since “true” BAT (i.e., brown adipocytes) is mixed with other tissues, such as WAT, muscle and vessels, a micrometer resolution would be required to separate brown fat cells from white fat cells. The resolution of MRI is typically in the order of millimeters, and thus BAT cannot be separated from WAT in the supraclavicular area.

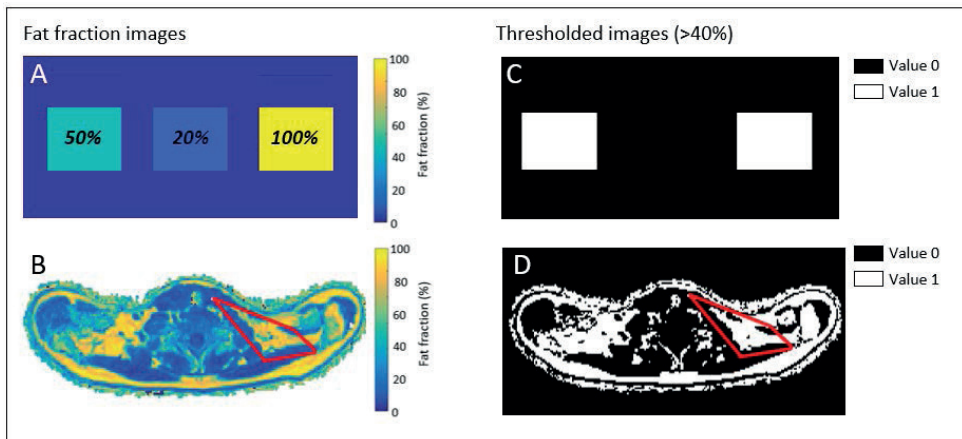


Figure 3. A simplified fat fraction (FF) image (A) and an MRI FF image (B) are shown in the left column. After applying a 40% FF threshold, values below this threshold are given a value of 0, whereas values above this threshold are given a value of 1 (C,D). FF values that are located within the ROI shown in red and that correspond to a value of 1 (white regions; D) are only included for analysis

This results in a segmentation challenge that hampers the extraction of “true” BAT within the supraclavicular depot. Post-processing techniques such as image thresholding could be used to exclude non-fatty tissue from the analysis. Image thresholding is a technique that is used to segment structures from an image, where image values above a certain threshold (e.g., 40%; see **Fig. 3A,C**) are set to 1 and values below this threshold are given a value of 0 or vice versa. Previous MRI studies^{38,41,42} have used image thresholding on FF maps. This is illustrated in **Fig. 3B,D** where values below 40% FF are given a value of 0 and values above 40% are given a value of 1. Only the FF values that are located within the delineated scBAT ROI and correspond to a value of 1 (white regions) are included in the analysis. The remaining FF values are usually averaged across the thresholded ROI, and the difference between the average baseline and post-cooling FF is used to estimate the

cold-induced scBAT FF change. Reports on the extent of cold-induced scBAT FF changes, however, vary in the literature [-0.4%,-4.7%]^{27,28}. An explanation for this inconsistency may be the differences in applied FF thresholds (e.g., 0-100%, 40-100%, 50-100%)^{38,41,42}.

1.5 AIM OF THIS THESIS

The primary aim of this thesis was to improve the overall methodology for assessing scBAT activity in human adults to enable evaluation of therapies (in)directly targeting BAT. First, we aimed to gain insight into the role of body composition and BAT activity on the human cold tolerance capacity. This will facilitate the optimization of cooling protocols to ensure maximal BAT stimulation in heterogenous study populations. In **chapter 2**, we therefore investigated the association between the shivering threshold time, as a proxy for the human cold tolerance capacity, with body composition, cold perception and scBAT activity and volume, quantified using [¹⁸F]FDG-PET-CT.

In the next chapters, we shifted our focus towards the non-invasive imaging modalities, IRT (**chapter 3**) and MRI (**chapter 4** and **chapter 5**), where we aimed to improve several technical challenges in order to provide reliable estimates of scBAT activity. IRT imaging has been previously used to study cold-induced changes in supraclavicular skin temperature. Most of these studies, however, still rely on manual segmentations, which can be very time consuming in large datasets and subjected to drawing variability. In **chapter 3**, we developed an open-access semiautomated segmentation tool (the IRT-toolbox) for measuring skin temperatures in the thoracic area to estimate scBAT activity, and compared it to manual segmentations.

In **chapter 4** and **5**, we focused on MR imaging for estimating scBAT FF in healthy adults. More specifically, since BAT cannot be easily distinguished from WAT, we aimed to explore the effect of different FF threshold ranges on different MRI-based outcomes in **chapter 4**, where we scanned once before and after cooling. Pre- and post-cooling assessments, however, do not provide sufficient insight into the time course of cold-induced scBAT FF changes. In addition, scBAT is located in the supraclavicular area, and thus prone to motion-induced variability. As such, in **chapter 5**, we aimed to minimize this variability by applying breath-holds and non-rigid image registration in a dynamic MRI protocol with a high temporal resolution for assessing FF changes in scBAT during cold exposure. In **chapter 6**, we summarized the main findings of this thesis, brought our results into perspective with the literature, and provided suggestions for future research.

REFERENCES

1. Cypess AM, Lehman S, Williams G, et al. Identification and importance of brown adipose tissue in adult humans. *N Engl J Med*. 2009;360(15):1509-1517. doi:10.1056/NEJMoa0810780
2. Virtanen KA, Lidell ME, Orava J, et al. Functional Brown Adipose Tissue in Healthy Adults. *N Engl J Med*. 2009;360(15):1518-1525. doi:10.1056/nejmoa0808949
3. Van Marken Lichtenbelt WD, Vanhommerig JW, Smulders NM, et al. Cold-activated brown adipose tissue in healthy men. *N Engl J Med*. 2009;360(15):1500-1508. doi:10.1056/NEJMoa0808718
4. Hanssen MJW, Hoeks J, Brans B, et al. Short-term cold acclimation improves insulin sensitivity in patients with type 2 diabetes mellitus. *Nat Med*. 2015;21(8):863-865. doi:10.1038/nm.3891
5. Becher T, Palanisamy S, Kramer DJ, et al. Brown adipose tissue is associated with cardiometabolic health. *Nat Med*. 2021;27(1):58-65. doi:10.1038/S41591-020-1126-7
6. Takx RAP, Ishai A, Truong QA, MacNabb MH, Scherrer-Crosbie M, Tawakol A. Supraclavicular Brown Adipose Tissue 18F-FDG Uptake and Cardiovascular Disease. *J Nucl Med*. 2016;57(8):1221-1225. doi:10.2967/JNUMED.115.166025
7. Oikonomou EK, Antoniadou C. The role of adipose tissue in cardiovascular health and disease. *Nat Rev Cardiol*. 2019;16(2):83-99. doi:10.1038/s41569-018-0097-6
8. Hoeke G, Kooijman S, Boon MR, Rensen PCN, Berbée JFP. Role of Brown Fat in Lipoprotein Metabolism and Atherosclerosis. *Circ Res*. 2016;118(1):173-182. doi:10.1161/CIRCRESAHA.115.306647
9. Saely CH, Geiger K, Drexel H. Brown versus white adipose tissue: A mini-review. *Gerontology*. 2011;58(1):15-23. doi:10.1159/000321319
10. Tan CL, Knight ZA. Regulation of Body Temperature by the Nervous System. *Neuron*. 2018;98(1):31-48. doi:10.1016/j.neuron.2018.02.022
11. Blondin DP, Frisch F, Phoenix S, et al. Inhibition of Intracellular Triglyceride Lipolysis Suppresses Cold-Induced Brown Adipose Tissue Metabolism and Increases Shivering in Humans. *Cell Metab*. 2017;25(2):438-447. doi:10.1016/j.cmet.2016.12.005
12. Bartelt A, Bruns OT, Reimer R, et al. Brown adipose tissue activity controls triglyceride clearance. *Nat Med*. 2011;17(2):200-206. doi:10.1038/nm.2297
13. Hoeke G, Kooijman S, Boon MR, Rensen PCN, Berbee JFP. Role of Brown Fat in Lipoprotein Metabolism and Atherosclerosis. *Circ Res*. 2016;118(1):173-182. doi:10.1161/CIRCRESAHA.115.306647
14. Carpentier AC, Blondin DP, Virtanen KA, Richard D, Haman F, Turcotte EE. Brown adipose tissue energy metabolism in humans. *Front Endocrinol (Lausanne)*. 2018;9(AUG):1-21. doi:10.3389/fendo.2018.00447
15. Weir G, Ramage LE, Akyol M, et al. Substantial Metabolic Activity of Human Brown Adipose Tissue during Warm Conditions and Cold-Induced Lipolysis of Local Triglycerides. *Cell Metab*. 2018;27(6):1348-1355.e4. doi:10.1016/j.cmet.2018.04.020
16. Nahon KJ, Janssen LGM, Sardjoe Mishre ASD, et al. The effect of mirabegron on energy expenditure and brown adipose tissue in healthy lean South Asian and European men. *Diabetes, Obesity Metab*. 2020;22(11):2032-2044. doi:10.1111/DOM.14120
17. Gashi G, Madoerin P, Maushart CI, et al. MRI characteristics of supraclavicular brown adipose tissue in relation to cold-induced thermogenesis in healthy human adults. *J Magn Reson Imaging*. 2019;50(4):1160-1168. doi:10.1002/jmri.26733
18. Ouellet V, Labbé SM, Blondin DP, et al. Brown adipose tissue oxidative metabolism contributes to energy expenditure during acute cold exposure in humans. *J Clin Invest*. 2012;122(2):545-552. doi:10.1172/JCI60433

19. Chen KY, Cypess AM, Laughlin MR, et al. Brown Adipose Reporting Criteria in Imaging Studies (BARCIST 1.0): Recommendations for Standardized FDG-PET/CT Experiments in Humans. *Cell Metab.* 2016;24(2):210-222. doi:10.1016/j.cmet.2016.07.014
20. Schilperoort M, Hoeke G, Kooijman S, Rensen PCN. Relevance of lipid metabolism for brown fat visualization and quantification. *Curr Opin Lipidol.* 2016;27(3):242-248. doi:10.1097/MOL.0000000000000296
21. Speakman J, Fischer Verlag G, Speakman JR, Ward S. Infrared thermography : principles and applications. *ZOOLOGY.* 1998;101:224-232.
22. Sun L, Verma S, Michael N, et al. Brown Adipose Tissue: Multimodality Evaluation by PET, MRI, Infrared Thermography, and Whole-Body Calorimetry (TACTICAL-II). *Obesity.* 2019;27(9):1434-1442. doi:10.1002/oby.22560
23. Jang C, Jalapu S, Thuzar M, et al. Infrared thermography in the detection of brown adipose tissue in humans. *Physiol Rep.* 2014;2(11):e12167. doi:10.14814/PHY2.12167
24. J L, DE M, C I-E, et al. Thermal Imaging Is a Noninvasive Alternative to PET/CT for Measurement of Brown Adipose Tissue Activity in Humans. *J Nucl Med.* 2018;59(3):516-522. doi:10.2967/JNUMED.117.190546
25. Hadi H El, Frascati A, Granzotto M, et al. Infrared thermography for indirect assessment of activation of brown adipose tissue in lean and obese male subjects. *Physiol Meas.* 2016;37(12):N118. doi:10.1088/0967-3334/37/12/N118
26. Neves EB, Vilaça-Alves J, Regina I, et al. Influence of Subcutaneous Fat Layer in Skin Temperature. *Motricidade.* 2016;11(4):120-126. doi:10.6063/motricidade.5999
27. Wu M, Junker D, Branca RT, Karampinos DC. Magnetic Resonance Imaging Techniques for Brown Adipose Tissue Detection. *Front Endocrinol (Lausanne).* 2020;11:421. doi:10.3389/FENDO.2020.00421/FULL
28. Karampinos DC, Weidlich D, Wu M, Hu HH, Franz D. Techniques and Applications of Magnetic Resonance Imaging for Studying Brown Adipose Tissue Morphometry and Function. *Handb Exp Pharmacol.* 2019;251:299-324. doi:10.1007/164_2018_158
29. Coombs BD, Szumowski J, Coshov W. Two-point Dixon technique for water-fat signal decomposition with B0 inhomogeneity correction. *Magn Reson Med.* 1997;38(6):884-889. doi:10.1002/MRM.1910380606
30. Cannon B, Nedergaard J. Brown Adipose Tissue: Function and Physiological Significance. *Physiol Rev.* 2004;84(1):277-359. doi:https://doi.org/10.1152/physrev.00015.2003
31. Van Der Lans AAJJ, Wierts R, Vosselman MJ, et al. Cold-activated brown adipose tissue in human adults: methodological issues. *Am J Physiol Regul Integr Comp Physiol.* 2014;307:103-113. doi:10.1152/ajpregu.00021.2014.-The
32. Janssen LGM, Nahon KJ, Bracké KFM, et al. Twelve weeks of exenatide treatment increases [18F] fluorodeoxyglucose uptake by brown adipose tissue without affecting oxidative resting energy expenditure in nondiabetic males. *Metabolism.* 2020;106:154167-154167. doi:10.1016/J.METABOL.2020.154167
33. Thuzar M, Law WP, Dimeski G, Stowasser M, Ho KKY. Mineralocorticoid antagonism enhances brown adipose tissue function in humans: A randomized placebo-controlled cross-over study. *Diabetes Obes Metab.* 2019;21(3):509-516. doi:10.1111/DOM.13539
34. JW C, AJ Y. Human physiological responses to cold exposure: Acute responses and acclimatization to prolonged exposure. *Auton Neurosci.* 2016;196:63-74. doi:10.1016/J.AUTNEU.2016.02.009
35. Toner MM, McArdle WD. Human Thermoregulatory Responses to Acute Cold Stress with Special Reference to Water Immersion. *Compr Physiol.* December 1996:379-397. doi:10.1002/CPHY.CP040117

36. Nahon KJ, Boon MR, Doornink F, Jazet IM, Rensen PCN, Abreu-Vieira G. Lower critical temperature and cold-induced thermogenesis of lean and overweight humans are inversely related to body mass and basal metabolic rate. *J Therm Biol.* 2017;69:238-248. doi:10.1016/j.jtherbio.2017.08.006
37. Human Adaptation and Accommodation - A. Roberto Frisancho. University of Michigan press. 1993.
38. Lundström E, Strand R, Johansson L, Bergsten P, Ahlström H, Kullberg J. Magnetic resonance imaging cooling-reheating protocol indicates decreased fat fraction via lipid consumption in suspected brown adipose tissue. *PLoS One.* 2015;10(4). doi:10.1371/journal.pone.0126705
39. Oreskovich S, Ong F, Ahmed B, et al. Magnetic resonance imaging reveals human brown adipose tissue is rapidly activated in response to cold. *J Endocr Soc.* October 2019. doi:10.1210/2019-00309
40. Klein S, Staring M, Murphy K, Viergever MA, Pluim JPW. Elastix: A toolbox for intensity-based medical image registration. *IEEE Trans Med Imaging.* 2010;29(1):196-205. doi:10.1109/TMI.2009.2035616
41. Coolbaugh CL, Damon BM, Bush EC, Welch EB, Towse TF. Cold exposure induces dynamic, heterogeneous alterations in human brown adipose tissue lipid content. *Sci Rep.* 2019;9(1):13600. doi:10.1038/s41598-019-49936-x
42. Holstila M, Virtanen KA, Grönroos TJ, et al. Measurement of brown adipose tissue mass using a novel dual-echo magnetic resonance imaging approach: A validation study. *Metabolism.* 2013;62(8):1189-1198. doi:10.1016/j.metabol.2013.03.002



Chapter 2

Association of shivering threshold time with body composition and brown adipose tissue in young adults

This chapter has been published in: Journal of Thermal Biology (2022) PMID: 36031206.

Aashley S.D. Sardjoe Mishre*
Borja Martinez-Tellez*
Francisco M. Acosta
Guillermo Sanchez-Delgado
Maaïke E. Straat
Andrew G. Webb
Hermien E. Kan
Patrick C.N. Rensen
Jonatan R. Ruiz

* Shared first authorship

ABSTRACT

Purpose: Brown adipose tissue (BAT) increases metabolic heat production in response to cold exposure. Body size and composition are involved in the human cold response, yet the influence of BAT herein have not fully been explored. Here, we aimed to study the association of the cold-induced shivering threshold time with body composition, BAT, the perception of shivering and skin temperature in young adults.

Methods: 110 young healthy adults (81 females; age=21.7±2.1 years, BMI=24.2±4.3 kg/m²) underwent 2 hours of individualized cooling, followed by the quantification of BAT using a ¹⁸F-fluorodeoxyglucose ([¹⁸F]FDG) positron emission tomography-computed tomography (PET-CT) scan. Body mass index (BMI), lean mass, fat mass and body surface area (BSA) were also measured. Shivering threshold time was defined as the time until shivering occurred using an individualized cooling protocol.

Results: The shivering threshold time was on average 116.1 minutes for males and 125.8 minutes for females, and was positively associated to BMI ($\beta=3.106$; $R^2=0.141$; $p=0.001$), lean mass ($\beta=2.295$; $R^2=0.128$; $p=0.001$) and fat mass ($\beta=1.492$; $R^2=0.121$; $p=0.001$) in females, but not in males (all $p\geq 0.409$). The shivering threshold time was positively associated with BSA in males ($p=0.047$) and females ($p=0.001$), but it was not associated with BAT volume or [¹⁸F]FDG uptake nor with the perception of shivering and skin temperature perception in both sexes.

Conclusion: The shivering threshold time is positively associated with whole-body adiposity and lean mass in females, but not in males. The shivering threshold time was positively associated with BSA, but no association was observed with BAT nor with the perception of shivering or skin temperature. Future research should consider the influence of body composition when applying cooling protocols among individuals with different phenotypical features.

2.1 INTRODUCTION

Since the discovery of metabolically activated brown adipose tissue (BAT) in human adults¹⁻³, many studies have addressed the physiological implication of this tissue in energy metabolism and cardiovascular health⁴. BAT has been identified as a thermogenic tissue due to its ability to dissipate energy as heat via uncoupling protein 1 (UCP-1), a process that mainly utilizes intracellular triglyceride-derived fatty acids as an energy source. A well-established physiological BAT activator is cold exposure^{5,6}. To maintain core body temperature during cooling, heat production will increase, a process that is known as cold-induced thermogenesis (CIT). CIT is divided into shivering and non-shivering thermogenesis (NST)^{7,8}, shivering thermogenesis is defined as the increase in heat production due to skeletal muscle contraction, whereas NST is defined as heat production that does not involve contractions of skeletal muscles, such as BAT activation⁹. However, recent studies¹⁰⁻¹² demonstrate that skeletal muscles may contribute to NST via futile cycles, which is a mechanism that generates heat independently of skeletal muscle contractions.

The most common technique to assess human BAT activity is by quantifying the uptake of a radioactively-labeled glucose tracer, ¹⁸F-fluorodeoxyglucose ([¹⁸F]FDG), after intravenous injection, by using a static positron emission tomography/computed tomography (PET-CT)¹³ scan. To ensure BAT activation, a variety of cooling strategies have been described¹⁴. These strategies differ in terms of duration, intensity, type of the cold stimulus (e.g., air-conditioned room, ice-blocks, water-perfused vests) or cooling strategy (i.e., standardized or individualized)¹³. In standardized cooling protocols, participants are exposed to a predetermined temperature for a certain duration, whereas in individualized cooling protocols the temperature is tailored to certain participant responses, such as heat production, skin temperature, perception of skin temperature, or the estimated onset of shivering¹⁵. Individualized cooling protocols based on the shivering threshold were developed to maximally stimulate NST in order to avoid an underestimation of BAT activity¹⁶.

Body composition refers to the amount of relative fat to muscle that is present in the body, which seems to be involved in the individualization of a cooling protocol. For instance, large individuals that are commonly characterized by a small body surface area to volume ratio can preserve heat better compared to smaller individuals¹⁷. Differences in body size may, therefore alter the cold tolerance, defined as the ability to withstand low temperatures¹⁸. Additionally, the cold tolerance may increase with the abundance of subcutaneous white adipose tissue (WAT)^{19,20} and lean mass²¹. Thus, larger individuals may have a higher cold tolerance capacity, although this response is quite variable between individuals⁶. Moreover, it has been shown that 10-days of cold acclimation in overweight individuals^{22,23} increases BAT volume and BAT [¹⁸F]FDG uptake. Curiously, the authors also

found that cold perception of skin temperature decreases after 10-days of cold acclimation, although subcutaneous WAT and lean mass were not altered. These findings suggest that human BAT may be involved in the cold tolerance capacity of an individual. Therefore, we hypothesize that individuals with a higher cold tolerance capacity have different body composition characteristics (i.e., a higher lean mass and/or fat mass), and higher BAT volume and activity compared to individuals with a lower cold tolerance capacity.

The aim of the present study was to investigate whether the shivering threshold time, as a proxy of the cold tolerance capacity, is associated with body composition (i.e., body mass index, body surface area, lean mass and fat mass), BAT volume, [^{18}F]FDG uptake, mean radiodensity (i.e., as a proxy of BAT fat content)²⁴, and with the perception of shivering and skin temperature during cold exposure, in young adults.

2.2 MATERIAL AND METHODS

2.2.1 Study subjects, experimental procedures, and ethics statement

Participants that were initially included in the present study (n=147) were enrolled in the ACTIBATE study²⁵ (ClinicalTrials.gov, ID: NCT02365129). The study was conducted in accordance with the Declaration of Helsinki (revised in 2013), and approved by the Human Research Ethics Committee of the University of Granada (n° 924) and of the “Servicio Andaluz de Salud” (Centro de Granada, CEI-Granada). All participants were healthy, non-smokers, non-vigorous exercisers, and did not use any medication that could affect their energetic or neuromuscular responses to cold exposure. Before the start of the study visits, participants were instructed to refrain from vigorous exercise (during 24 hours before the visit), and from alcohol and stimulant beverages (during 6 hours before the visit).

Participants were asked to come to the research center after a 8 hours fasting period. During the first visit, the shivering threshold test was conducted to determine the water temperature of the cooling vest at the onset of shivering (shivering threshold temperature). During the second visit, a 2-hour individualized cooling protocol was conducted using the pre-determined shivering threshold temperature. After 2-hours of cooling, a static [^{18}F]FDG-PET-CT scan was acquired. The time between the study visits was 48-72 hours. In a third visit, body composition was measured. The procedures per visit are outlined below and are described in detail elsewhere²⁶. The measurements were conducted during four time periods of approximately 12 participants in each period, from October 15th to November 28th, 2015 and 2016 in Granada (Spain).

2.2.2 Body composition and anthropometrics

Body composition (i.e., lean and fat mass) was assessed on a separate day by Dual Energy X-ray Absorptiometry (DEXA; HOLOGIC, Discovery Wi). Body weight and height were measured using a SECA scale and stadiometer (model 799, Electronic Column Scale, Hamburg, Germany), during which participants were wearing a T-shirt and shorts without shoes on. Lean mass (LM) and fat mass (FM) values were obtained from the DEXA software. Body mass index (BMI) was calculated as body weight divided by height squared (kg/m^2). The body surface area (BSA) was determined according to the du Bois formula²⁷, in which the height is expressed in centimeters and the weight in kilograms:

$$BSA = 0.007184 * Height^{0.725} * Weight^{0.452} \quad [3]$$

2.2.3 Determination of the shivering threshold

At first, participants changed into standardized clothes [sandals, T-shirt and shorts, clo-value: 0.20^{28}], and entered a warm room ($22.1 \pm 1.6^\circ\text{C}$) for approximately 30 minutes. Subsequently, they entered an air-conditioned room ($19.8 \pm 0.5^\circ\text{C}$) and sat down in a chair in the same position. After 15 minutes, participants were asked to wear a temperature-controlled water perfused cooling vest (Polar Products Inc., Ohio, USA). The water temperature was initially set at 16.6°C , and decreased every 10 minutes until the temperature reached 5.5°C . Participants were asked to self-report the occurrence of shivering, and one researcher visually monitored whether shivering occurred throughout the experiment. If participants did not report shivering and the researcher did not observe it either, the water temperature was decreased by 0.6°C every 15 minutes until 3.8°C . If shivering had not occurred, participants remained exposed to 3.8°C for another 45 minutes, after which the test was finished. The shivering threshold time was determined as the total time period, during which participants were exposed to cold until shivering occurred.

2.2.4 Perception of shivering and skin temperature

Perception of shivering was measured by a numeric rate scale of 10 points, where 0 represented “I am not shivering” and 10 represented “I am shivering a lot”. Additionally, the perception of skin temperature was measured using a seven-point scale from the American Society of Heating, Refrigerating and Air Conditioning Engineers (ASHRAE)²⁹. This scale ranges from cold (-3), cool (-2), slightly cool (-1), neutral (0), slightly warm (1), warm (2) to hot (3). Participants were asked to score their perception of skin temperature for several anatomical areas, including the clavicular area, abdomen, arms, hands, legs, feet and whole-body areas. All scales were measured throughout the entire study, but only the measurements in the warm period and at end of the shivering threshold test were used in the analyses³⁰.

2.2.5 Individualized cooling protocol prior to the [¹⁸F]FDG-PET-CT acquisition

Upon arrival, all participants confirmed that they followed all pre-study instructions. Similar to the first visit, participants changed into standardized clothes [sandals, T-shirt and shorts, clo-value: 0.20²⁸], and entered a warm room for 30 min (22.2±0.5°C) before they entered an air-conditioned room (20.2±0.3°C). Participants were then asked to wear the temperature-controlled water perfused cooling vest (Polar Products Inc., Ohio, USA) for 60 minutes. The water temperature was set at ~4°C above the water temperature that caused the onset of shivering during the first visit. The water temperature was set at 3.8°C for those participants who did not report shivering during the shivering threshold test^{14,31}. During 60 minutes of individualized cooling, participants were asked to report whether they experienced shivering. In that case, the water temperature was increased by 1°C and participants wore a bathrobe until shivering subsided. After 60 minutes of cold exposure, [¹⁸F]FDG was administered intravenously (185 MBq; ~2.78 MBq/kg), and the water temperature was increased by 1°C. This temperature was kept stable for the remaining 60 minutes of cooling. After two hours of individualized cooling, a [¹⁸F]FDG PET-CT scan (Siemens Biograph 16 PET/CT, Siemens, Germany) was acquired. A CT scan was used for anatomical localization with an attenuation correction at a peak voltage of 120, and for the PET acquisition, a scan time of six minutes per bed position was implemented. Two bed positions were scanned ranging from the *cerebellum* to thoracic vertebrae 4 to 6, depending on the size of the person. The date of the PET/CT scan was annotated, as January 1st, day 1, and December 31st, day 365/366. The date (as a discrete number) of the PET/CT acquisition was used as a proxy of the outdoor temperature.

2.2.6 PET-CT data analysis

PET-CT scans were analyzed using Beth Israel plugin for FIJI¹ software (<http://sourceforge.net/projects/bifijiplugins/>)³². The standard uptake value (SUV) and the SUV threshold (SUV_{thres}) were calculated as follows¹³:

$$SUV = \frac{[^{18}F]FDG \text{ uptake (kBq/mL)}}{\text{injected dose [kBq]/patient weight [g]}} \quad [1]$$

$$SUV_{thres} \cdot SUV \geq \frac{1.2}{\text{lean body mass/body mass}} \quad [2]$$

A fixed segmentation range of [-190, -10] Hounsfield units was applied¹³. According to the pre-determined SUV and HU thresholds, regions of interest (ROIs) were outlined from the *atlas vertebrae* (Cervical 1) to the *thoracic vertebrae* 4. BAT volume and [¹⁸F]FDG uptake outcomes (SUV_{mean} and SUV_{peak}) were determined based on the BARCIST 1.0 recommendations^{13,33}. As a measure for BAT metabolic activity, we multiplied BAT SUV_{mean} by BAT volume. BAT mean radiodensity was calculated as the average radiodensity of those voxels meeting the aforementioned criteria in a single ROI from the atlas to thoracic ver-

tebrae 4, excluding the mouth. Twenty-five individuals presented several voxels classified as BAT which were outside these anatomical areas, and these participants were therefore excluded from the BAT mean radiodensity analyses. The [^{18}F]FDG uptake in skeletal muscle was retrieved from a single slice ROI placed in several skeletal muscles i.e., *cervical, scalene, longus colli, paravertebral, subscapular, sternocleidomastoid, supraspinous, trapezius, deltoid, pectoralis major, and triceps braquii*), which were averaged⁸.

2.2.7 Statistical analysis

Data normality was confirmed using the Shapiro-Wilk test, visual histograms, and Q-Q plots. Unpaired t-tests were performed to compare participant characteristics between males and females, and between participants who reported shivering vs. who did not report shivering. For the main analysis, linear regression analyses were performed to study the association of the shivering threshold time with i) body composition (i.e. BMI, BSA, lean mass and fat mass) and ii) BAT volume, [^{18}F]FDG uptake (SUVmean and SUVpeak), and BAT mean radiodensity. These linear regression analyses were repeated with the date of the PET/CT acquisition as a confounder. Data were analyzed for males and females separately. In addition, the cohort was divided in tertiles based on the shivering threshold time for males and females [males: low (from 52 to 114 min)], medium (from 118 to 151 min) and high tertiles (from 153 to 175 min); and females: low (from 53 to 92 min), medium (from 93 to 120 min) and high tertiles (from 121 to 205 min)]. Based on these tertiles, one-way analyses of variance (ANOVA) were performed, where the perception of shivering and skin temperature were compared across the different groups. We repeated these ANOVAs adjusting for potential confounders, including BMI, BSA or the date of the PET/CT acquisition. All statistical analyses were performed using SPSS (Statistical Package for the Social Sciences; version 22) and the level of significance was set to <0.05 . All figures were made using GraphPad Prism (version 8.0.0).

2.3 RESULTS

2.3.1 Participant characteristics

A total of 37 participants were not included in the main analysis: five participants because the [^{18}F]FDG tracer was not correctly injected, seven participants due to technical problems with the cooling device, and 25 individuals were included in a secondary analysis because no shivering was visually detected by the researcher. The 25 individuals that did not shiver showed a higher whole-body adiposity and BAT volume³⁴, and reported a lower perception of shivering and skin temperature than individuals who shivered ($n=110$; all $p\leq 0.034$, **Table S1**). **Table 1** shows the characteristics of participants who reached the shivering threshold and were included in the main analyses. Males had a higher whole-body adiposity than females (all $p\leq 0.004$), but the shivering threshold time and BAT were

similar between sexes (all $p \geq 0.05$, **Table 1**). However, significant sex interaction effects were detected in many of the associations, and thus the results are separately presented for males ($n=29$) and females ($n=81$).

Table 1. Characteristics of participants.

	All (n=110)		Male (n=29)		Female (n=81)		P
Age (years)	21.7	(2.1)	22.0	(2.1)	21.7	(2.1)	0.521
Weight (kg)	68.1	(14.7)	80.5	(15.6)	63.7	(11.7)	<0.001
Height (m)	1.67	(8.2)	174.8	(6.7)	164.0	(6.6)	<0.001
Body mass index (kg/m ²)	24.4	(4.3)	26.3	(5.0)	23.6	(3.9)	0.004
Lean mass (kg)	40.1	(8.7)	51.5	(6.5)	35.8	(5.0)	<0.001
Fat mass (kg)	24.2	(8.1)	24.3	(9.9)	24.2	(7.5)	0.945
Body surface area (m ²)	1.7	(0.2)	1.9	(0.2)	1.7	(0.2)	<0.001
Visceral adipose tissue mass (kg)	0.31	(0.17)	0.41	(0.17)	0.28	(0.16)	<0.001
Shivering threshold time (min)	116	(34)	126	(36)	113	(32)	0.072
BAT volume (ml)	64	(54)	69	(61)	62	(51)	0.542
BAT metabolic activity (g)	316	(327)	289	(329)	326	(327)	0.775
BAT SUVmean	3.7	(1.9)	3.2	(1.4)	3.9	(2.1)	0.064
BAT SUVpeak	10.8	(7.8)	9.1	(7.3)	11.4	(8.0)	0.171
BAT mean radiodensity (HU)*	-58.5	(13.3)	-55.7	(9.9)	-59.5	(14.3)	0.200

All data are presented as mean and standard deviation (SD). P values obtained from student t-test. *109 participants had valid data on this outcome (28 males and 65 females). BAT: brown adipose tissue; HU: Hounsfield units. SUV: standardized uptake value.

2.3.2 Association between the shivering threshold time with body composition

There were positive and significant associations between the shivering threshold time and BMI ($\beta=3.106$; $R^2=0.141$; $p=0.001$; **Fig. 1B**), lean mass ($\beta=2.295$; $R^2=0.128$; $p=0.001$; **Fig. 1D**) and fat mass ($\beta=1.492$; $R^2=0.121$; $P=0.001$; **Fig. 1F**) in females, but not in males (all $p \geq 0.409$, **Fig. 1A-C**). The shivering threshold time was positively associated with BSA in both sexes (males: $\beta=73.056$; $R^2=0.138$; $p=0.047$, **Fig. 1G**; and females: $\beta=70.519$; $R^2=0.122$; $p=0.001$, **Fig. 1H**).

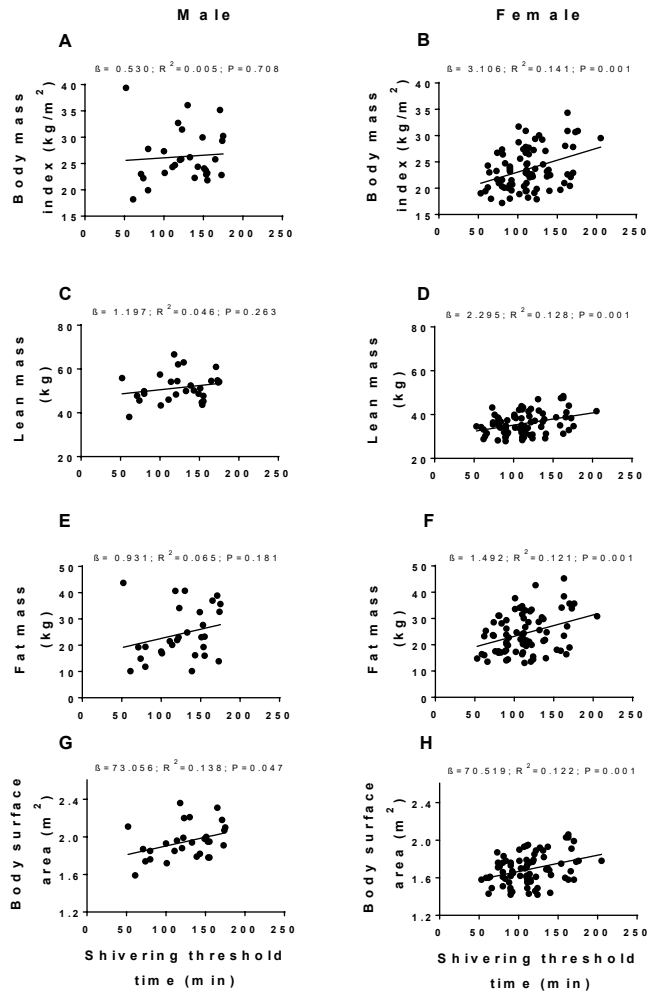


Figure 1. Associations between the shivering threshold time (minutes) and body composition: body mass index (A and B), lean mass (C and D), fat mass (E and F), and body surface area (G and H) by sex. Beta values, adjusted R squared (R^2) and P-values are shown.

The associations persisted when the date of the PET/CT acquisition was included as a confounder (data not shown). No associations were found between the shivering threshold time and BAT volume (Fig. 2A and B), BAT SUVmean (Fig. 2C and D), BAT SUVpeak (Fig. 2E and F), BAT mean radiodensity (Fig. 2G and H) or BAT metabolic activity (Fig. S1A and B) in both sexes (all $p > 0.05$). This lack of significant associations between the shivering threshold time and BAT-related outcomes persisted when the date of the PET/CT acquisition was included as a confounder (data not shown). We repeated all the analyses including the participants who did not report shivering ($n=25$) and the linear regressions remained unaltered (data not shown).

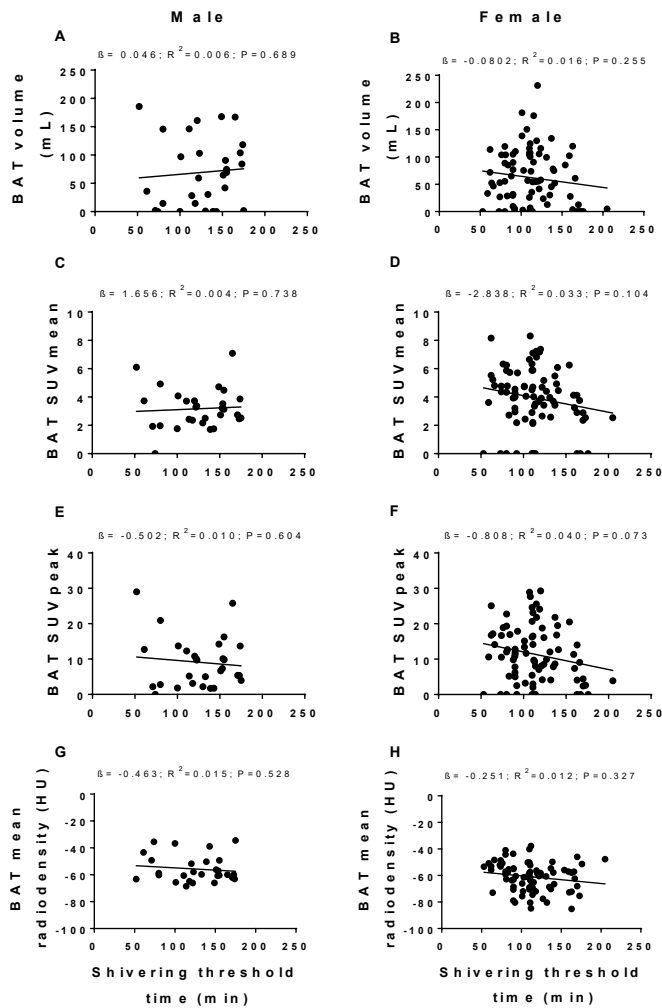


Figure 2. Associations between the shivering threshold time (minutes) and brown adipose tissue (BAT) related outcomes. BAT volume [mL] (**A** and **B**), BAT standardized uptake value (SUV) mean (**C** and **D**), BAT SUVpeak (**E** and **F**), and BAT mean radiodensity (**G** and **H**) by sex. 28 male and 65 female had valid data on BAT mean radiodensity. Beta values, adjusted R squared (R^2) and P-values are shown. HU: Hounsfield units.

2.3.3 Association between the shivering threshold time with the perception of shivering and skin temperature

Subsequently, we determined the tertiles in terms of the shivering threshold time (i.e., low, medium and high) for males and females separately. Similar perceptions of shivering at the end of cold exposure were reported by males and females (all $p > 0.05$, **Fig. 3A** and **B**) across tertiles of the shivering threshold time. Males also reported a similar perception of skin temperature of the clavicular area (**Fig. 3C**); however, females in the highest tertile (i.e., longest shivering threshold time) reported a colder perception on skin temperature

of the clavicular area than females in the lowest tertile (average perception on skin temperature of clavicular area \pm standard deviation: -2.4 ± 0.7 points vs. -1.8 ± 1.2 points; $p=0.035$, **Fig. 3D**). For other anatomical areas, no significant differences were observed across tertiles for both sexes (**Table S2**). We repeated all these analyses adjusting for BMI, BSA, and date of the PET/CT acquisition, and the results were unaltered (all $p>0.05$; data not shown).

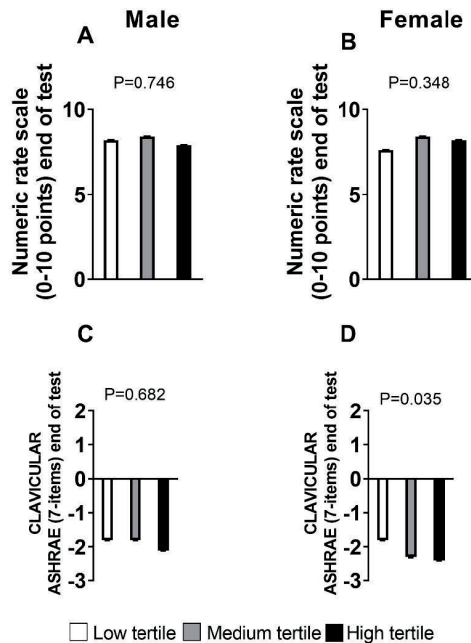


Figure 3. The perception of shivering and skin temperature in the clavicular area in males (A, C) and females (B, D). The perception of shivering was measured by a numeric rate scale, where 0 represented “I am not shivering” and 10 represented to “I am shivering a lot”. Perception of skin temperature at clavicular area was measured by an ASHRAE scale that ranges from cold (-3), cool (-2), slightly cool (-1), neutral (0), slightly warm (1), warm (2) and hot (3). Data are divided by tertiles of shivering threshold time by males (i.e., 52-114, 118-151 and 153-175 minutes) and females (i.e., 53-92, 93-120 and 121-205 minutes) separately.

2.4 DISCUSSION

The present study shows that the shivering threshold time is positively related to whole-body adiposity and lean mass in females, but not in males. In both sexes, the shivering threshold time is positively associated with BSA, but it is not associated with BAT parameters nor with the perception of shivering and skin temperature in young adults. Thus, these findings suggest that the cold tolerance capacity might not be related to BAT activation in humans.

2.4.1 Role of body composition and brown adipose tissue in the shivering threshold time

Our data shows that the shivering threshold time is weakly related to both fat and lean mass in females (LM: $\beta=2.295$; $R^2=0.128$; $p=0.001$; FM: $\beta=1.492$; $R^2=0.121$; $p=0.001$), but not in males. This may be due to differences in body composition between both genders (**Table 1**). For instance, men had a higher average BMI than women (26.3 kg/m^2 vs. 23.6 kg/m^2 ; **Table 1**), with adipose tissue stored mainly in the trunk/abdominal area vs. hip/thigh area in females³⁵. In the present study, we used a water-perfused cooling vest, which only covered the trunk and the abdomen. Thus, it might be possible that this specific protocol locally cooled several areas at which adipose tissue is more abundant in men than in women, which may have induced different physiological responses. Albeit not significant, females tended to shiver faster compared to males ($p=0.072$), which is in agreement with previous results³⁶. This may be due to a better insulation in male participants considering that the BMI was higher in males than in females. Future studies using air-conditioning cooling protocols, or whole-body water-perfused cooling mattresses/suits, might be of interest to investigate the role of body composition in the regulation of the cold tolerance capacity in men versus women. Interestingly, the shivering threshold time was positively related to BSA, which is a well-known determinant of heat loss³⁷. This finding concurs with studies showing that larger male individuals have an increased cold tolerance capacity^{19,21}. In addition, it has been shown that total body weight and BSA were the main factors that explained sex differences in the thermogenic response during cold exposure³⁸.

Contrary to our hypothesis, we found no association between the shivering threshold time and BAT volume, [¹⁸F]FDG uptake or BAT mean radiodensity in young adults, which suggests that BAT activity might not influence the cold tolerance. Interestingly, Van Der Lans et al.³⁹ reported that the shivering threshold time did not change after 10-days of cold exposure in young and lean individuals³⁹. However, they observed that BAT volume and [¹⁸F]FDG uptake substantially increased after the intervention, which was accompanied by a decrease in the perception of shivering. It is biologically plausible that the cold-induced recruitment of BAT may have contributed to the decrease in the perception of shivering, thereby improving cold tolerance capacity, although this finding was not replicated in another cohort of individuals with overweight⁴⁰. In another study¹⁵, it has been shown that shivering intensity was substantially reduced, while NST increased in healthy males after 7-days of cold exposure. It was suggested that these effects might be mediated by an enhancement in skeletal muscle function rather than an improvement in BAT function. In our study, we were not able to objectively quantify shivering. Therefore, we cannot distinguish between NST and shivering thermogenesis. Based on previous studies¹⁰⁻¹², we believe that skeletal muscles may be involved in the early stages of NST, but in this study, we cannot make any assumption on the contribution of thermogenic tissues during the

process of NST and shivering. Therefore, future studies are needed to gain further insight into the interplay between cold tolerance capacity, BAT and skeletal muscle activity.

2.4.2 The shivering threshold time does not relate to the perception of shivering and skin temperature for individuals who reported shivering

The shivering threshold time was not related to the perception of shivering and skin temperature. This might be explained by various factors: First, the range of the ASHRAE thermal perception scale may be too limited, as it only ranges from 0 to -3 points (for cooling), which could result in low sensitivity to detect whether participants perceived colder skin temperatures (below -3 points). Second, there could be a delay in processing of thermal perception and the onset of shivering as these physiological processes may be independently regulated. Shivering thermogenesis is regulated in the preoptic area within the hypothalamus, whereas afferent signals related to thermal perception are received by the thalamus and relayed onto the somatosensory cortex⁴¹, and these might be independently regulated. Third, there was a subgroup of participants for whom shivering was not visually detected by the researcher (n=25; **Table S1**), and they self-reported a lower perception of shivering and skin temperature, even though they were exposed to cold for a substantially longer period (+1 h, **Table S1**) than individuals who reported shivering (n=110). Interestingly, the participants who did not shiver had a higher BSA, BMI, fat mass and lean mass, which suggests that they might have a higher cold tolerance capacity due to better insulation traits compared to the group that reported shivering. However, although this group had a higher BAT volume, they showed a similar BAT [¹⁸F]FDG uptake compared to individuals who did report shivering, suggesting no differences in metabolic activity of BAT. Collectively, these hypotheses need to be further investigated to fully understand the possible mechanisms that are driving the two different phenotypes.

2.4.3 Limitations

A limitation of the present study is that no causality can be established, which however is inherent to all cross-sectional studies. The study population only included young and relatively healthy adults, which does not allow for extrapolation of results to populations of other age or health status. Additionally, there was a substantial sample size difference between male and female participants, and therefore, the results were not corrected for the False Discovery Rate. Another limitation is that we did not measure steroid hormones in this cohort, which hampers the possibility to perform further analyses investigating the role of sex in these associations. Moreover, a main limitation of the study is that the shivering threshold time was determined visually by the researcher and self-reported by participants; thus, no objective measurements were used. As such, visual inspection of shivering and self-reported shivering do not allow for the detection of invisible micro-shivering, which is defined as the thermoregulatory tonus prior to shivering⁴². Future studies should, therefore, use more objective measurements of shivering to confirm or

refute the present findings. Finally, although the static [^{18}F]FDG-PET/CT scan is commonly used for assessing BAT volume *in vivo*, it has some limitations. For example, it does not allow the observation of small brown fat deposits within white adipose tissue. Consequently, this study should be replicated if a new technology for BAT volume assessment *in vivo* becomes available. Alternatively, BAT detection can also be improved by using a multi-modality approach, for example by combining [^{18}F]FDG-PET/CT, magnetic resonance imaging and infrared thermography⁴³.

In conclusion, the shivering threshold time is positively, but weakly, related to whole-body adiposity and lean mass in females, but not in males. In addition, in both sexes, the shivering threshold time was positively related to BSA, but neither with BAT-related outcomes nor with perception of shivering and skin temperature. Future research could further explore the relation between the cold tolerance capacity and BAT by using objective study settings and a multi-modality approach to increase the sensitivity for BAT detection. Additionally, future studies should consider the potential influences of body composition more carefully when applying cooling protocols to heterogenous study populations.

SUPPLEMENTARY FIGURES

Table S1. Characteristics of participants who reported and did not report shivering

	Reporting shivering (n=110)		Not reporting shivering (n=25)		P
Age (years)	21.7	(2.1)	22.9	(2.1)	0.016
Sex (n; % male)	n=29;	26%	n=16;	64%	<0.001
Weight (kg)	68.1	(14.8)	84.7	(20.5)	<0.001
Height (m)	166.9	(8.2)	174.8	(7.7)	<0.001
Body mass index (kg/m ²)	24.4	(4.3)	27.5	(5.6)	0.002
Lean mass (kg)	40.1	(8.7)	49.9	(10.7)	<0.001
Fat mass (kg)	24.2	(8.1)	29.9	(11.7)	0.005
Body surface area (m ²)	1.7	(0.2)	2.0	(0.2)	<0.001
Visceral adipose tissue mass (g)	313.5	(169.8)	448.2	(206.6)	0.001
Shivering threshold time (min)	116.1	(33.6)	173.4	(20.2)	<0.001
BAT volume (ml)	64.0	(53.7)	99.0	(71.6)	0.007
BAT metabolic activity (g)	316	(327)	486	(363)	0.340
BAT SUVmean	3.7	(1.9)	4.1	(2.0)	0.389
BAT SUVpeak	10.8	(7.8)	14.1	(10.0)	0.078
BAT mean radiodensity (HU)*	-58.5	(13.3)	-56.5	(13.3)	0.489
Perception of shivering	8.1	(1.9)	5.8	(2.2)	<0.001
Cold perception on the clavicular	-2.1	(0.9)	-1.7	(0.9)	0.074
Cold perception on the abdomen	-2.5	(0.8)	-2.1	(0.9)	0.008
Cold perception on the arms	-2.7	(0.5)	-2.2	(0.7)	<0.001
Cold perception on the hands	-2.8	(0.5)	-2.2	(0.9)	<0.001
Cold perception on the legs	-2.6	(0.6)	-2.3	(0.8)	0.034
Cold perception on the feet	-2.8	(0.5)	-2.6	(0.6)	0.100
Cold perception on the whole body	-2.7	(0.5)	-2.3	(0.8)	0.005

All data are presented as mean and standard deviation (SD). P values from student t-test. P value from the sex outcome was obtained from chi-square test. *109 participants had valid data on this outcome (108 participants who reported and 25 who did not report shivering). The perception of shivering was measured by a numeric rate scale, where 0 represented “I am not shivering” and 10 represented to “I am shivering a lot”. Perception of skin temperature areas were measured by ASHRAE scales that ranges from cold (-3), cool (-2), slightly cool (-1), neutral (0), slightly warm (1), warm (2) and hot (3). These scores were determined in the clavicular, abdomen, arms, hands, legs, feet and whole-body areas. BAT: brown adipose tissue; HU: Hounsfield Units; SUV: standardized uptake value.

Table S2. Perception of skin temperature (i.e., abdomen, arms, hands, legs, feet and whole-body areas) at the end of the shivering threshold test in males and females.

	Male (n=29)				Female (n=81)			
	Low (n=10)	Medium (n=10)	High (n=9)	p	Low (n=27)	Medium (n=27)	High (n=27)	p
Cold perception on the abdomen	-2.7 (0.7)	-2.7 (0.5)	-2.8 (0.4)	0.939	-2.4 (1.0)	-2.5 (0.6)	-2.6 (0.8)	0.687
Cold perception on the arms	-2.7 (0.5)	-2.7 (0.5)	-2.3 (0.5)	0.194	-2.8 (0.4)	-2.8 (0.4)	-2.7 (0.5)	0.580
Cold perception on the hands	-3.0 (0.0)	-2.6 (0.7)	-2.6 (0.5)	0.120	-2.9 (0.3)	-2.7 (0.6)	-2.7 (0.6)	0.263
Cold perception on the legs	-2.7 (0.5)	-2.2 (0.6)	-2.6 (0.5)	0.135	-2.6 (0.7)	-2.6 (0.6)	-2.6 (0.6)	0.967
Cold perception on the feet	-2.8 (0.4)	-2.7 (0.5)	-2.9 (0.3)	0.624	-2.8 (0.5)	-2.8 (0.5)	-2.8 (0.7)	0.962
Cold perception on the whole body	-2.9 (0.3)	-2.6 (0.5)	-2.7 (0.5)	0.315	-2.7 (0.6)	-2.7 (0.5)	-2.7 (0.5)	0.960

Data are divided by tertiles of shivering threshold time by male and female separately, and are presented as mean and standard deviation. P values obtained from univariate analyses of variance. Perception of skin temperature areas were measured by ASHRAE scales that ranges from cold (-3), cool (-2), slightly cool (-1), neutral (0), slightly warm (1), warm (2) and hot (3). These scores were determined in the abdomen, arms, hands, legs, feet and whole-body areas. These tertiles range from 52-114, 118-151 and 153-175 minutes of shivering threshold time in male, and from 53-92, 93-120 and 121-205 minutes in female. L: Low tertile; M: Medium tertile; H: High tertile.

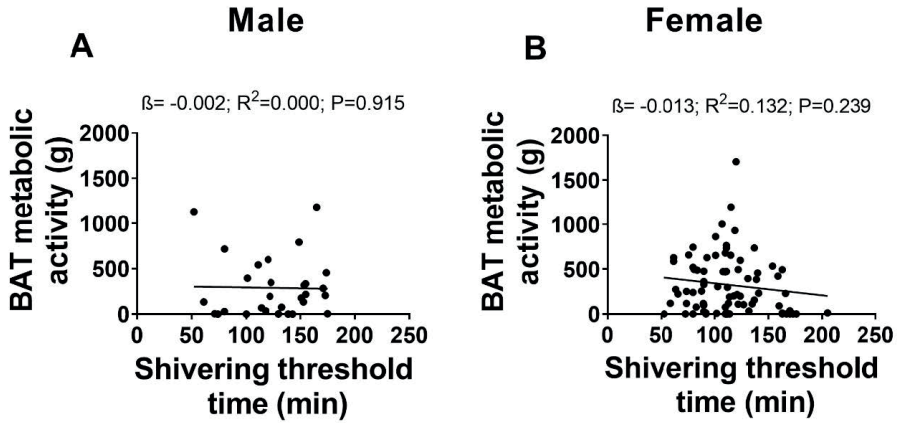


Figure S1. Associations between the shivering threshold time (minutes) and brown adipose tissue (BAT) metabolic activity, defined as BAT SUVmean * volume in males (A) and females (B). Unstandardized Beta values, adjusted R squared (R^2) and P-values are shown.

REFERENCES

1. Cypess AM, Lehman S, Williams G, et al. Identification and importance of brown adipose tissue in adult humans. *N Engl J Med*. 2009;360(15):1509-1517. doi:10.1056/NEJMoa0810780
2. Van Marken Lichtenbelt WD, Vanhommerig JW, Smulders NM, et al. Cold-activated brown adipose tissue in healthy men. *N Engl J Med*. 2009;360(15):1500-1508. doi:10.1056/NEJMoa0808718
3. Virtanen KA, Lidell ME, Orava J, et al. Functional Brown Adipose Tissue in Healthy Adults. *N Engl J Med*. 2009;360(15):1518-1525. doi:10.1056/nejmoa0808949
4. Oikonomou EK, Antoniades C. The role of adipose tissue in cardiovascular health and disease. *Nat Rev Cardiol*. 2019;16(2):83-99. doi:10.1038/s41569-018-0097-6
5. Cannon B, Nedergaard J. Brown Adipose Tissue: Function and Physiological Significance. *Physiol Rev*. 2004;84(1):277-359. doi:https://doi.org/10.1152/physrev.00015.2003
6. Brychta RJ, Chen KY. Cold-induced thermogenesis in humans. *Eur J Clin Nutr*. 2017;71(3):345-352. doi:10.1038/ejcn.2016.223
7. u Din M, Raiko J, Saari T, et al. Human brown adipose tissue [15O]O₂ PET imaging in the presence and absence of cold stimulus. *Eur J Nucl Med Mol Imaging*. 2016;43(10):1878-1886. doi:10.1007/s00259-016-3364-y
8. Blondin DP, Labbé SM, Phoenix S, et al. Contributions of white and brown adipose tissues and skeletal muscles to acute cold-induced metabolic responses in healthy men. *J Physiol*. 2015;593(3):701-714. doi:10.1113/jphysiol.2014.283598
9. IUPS Thermal Commission (2001) Glossary of terms for thermal physiology. Third ed. Revised by The Commission for Thermal Physiology of the International Union of Physiological Sciences. *Jap J Physiol* 51: 245–280. - Open Access Library.
10. Nowack J, Giroud S, Arnold W, Ruf T. Muscle non-shivering thermogenesis and its role in the evolution of endothermy. *Front Physiol*. 2017;8(NOV):889. doi:10.3389/FPHYS.2017.00889/BIBTEX
11. Bal NC, Sahoo SK, Maurya SK, Periasamy M. The Role of Sarcolipin in Muscle Non-shivering Thermogenesis. *Front Physiol*. 2018;9:1217. doi:10.3389/FPHYS.2018.01217/BIBTEX
12. Grigg G, Nowack J, Bicudo JEPW, Bal NC, Woodward HN, Seymour RS. Whole-body endothermy: ancient, homologous and widespread among the ancestors of mammals, birds and crocodylians. *Biol Rev*. 2022;97(2):766-801. doi:10.1111/BRV.12822
13. Chen KY, Cypess AM, Laughlin MR, et al. Brown Adipose Reporting Criteria in Imaging Studies (BARCIST 1.0): Recommendations for Standardized FDG-PET/CT Experiments in Humans. *Cell Metab*. 2016;24(2):210-222. doi:10.1016/j.cmet.2016.07.014
14. van der Lans AAJJ, Wierts R, Vosselman MJ, Schrauwen P, Brans B, van Marken Lichtenbelt WD. Cold-activated brown adipose tissue in human adults: Methodological issues. *Am J Physiol - Regul Integr Comp Physiol*. 2014;307(2):R103-13. doi:10.1152/ajpregu.00021.2014
15. Gordon K, Blondin DP, Friesen BJ, Tingelstad HC, Kenny GP, Haman F. Seven days of cold acclimation substantially reduces shivering intensity and increases nonshivering thermogenesis in adult humans. *J Appl Physiol*. 2019;126(6):1598-1606. doi:10.1152/jappphysiol.01133.2018
16. U Din M, Saari T, Raiko J, et al. Postprandial Oxidative Metabolism of Human Brown Fat Indicates Thermogenesis. *Cell Metab*. 2018;28(2):207-216.e3. doi:10.1016/j.cmet.2018.05.020
17. JW C, AJ Y. Human physiological responses to cold exposure: Acute responses and acclimatization to prolonged exposure. *Auton Neurosci*. 2016;196:63-74. doi:10.1016/J.AUTNEU.2016.02.009
18. Bligh J, Johnson KG. Glossary of terms for thermal physiology. *J Appl Physiol*. 1973;35(6):941-961. doi:10.1152/jappphysiol.1973.35.6.941

19. Human Adaptation and Accommodation - A. Roberto Frisancho. University of Michigan press. 1993.
20. Toner MM, McArdle WD. Human Thermoregulatory Responses to Acute Cold Stress with Special Reference to Water Immersion. *Compr Physiol*. December 1996:379-397. doi:10.1002/CPHY.CP040117
21. Nahon KJ, Boon MR, Doornink F, Jazet IM, Rensen PCN, Abreu-Vieira G. Lower critical temperature and cold-induced thermogenesis of lean and overweight humans are inversely related to body mass and basal metabolic rate. *J Therm Biol*. 2017;69:238-248. doi:10.1016/j.jtherbio.2017.08.006
22. Hanssen MJW, Van Der Lans AAJJ, Brans B, et al. Short-term cold acclimation recruits brown adipose tissue in obese humans. *Diabetes*. 2016;65(5):1179-1189. doi:10.2337/db15-1372
23. Hanssen MJW, Hoeks J, Brans B, et al. Short-term cold acclimation improves insulin sensitivity in patients with type 2 diabetes mellitus. *Nat Med*. 2015;21(8):863-865. doi:10.1038/nm.3891
24. Din MU, Raiko J, Saari T, et al. Human brown fat radiodensity indicates underlying tissue composition and systemic metabolic health. *J Clin Endocrinol Metab*. 2017;102(7):2258-2267. doi:10.1210/jc.2016-2698
25. Sanchez-Delgado G, Martinez-Tellez B, Olza J, et al. Activating brown adipose tissue through exercise (ACTIBATE) in young adults: Rationale, design and methodology. *Contemp Clin Trials*. 2015;45(Pt B):416-425. doi:10.1016/j.cct.2015.11.004
26. Martinez-Tellez B, Sanchez-Delgado G, Garcia-Rivero Y, et al. A new personalized cooling protocol to activate brown adipose tissue in young adults. *Front Physiol*. 2017;8(NOV):863. doi:10.3389/fphys.2017.00863
27. Du Bois D, Du Bois EF. A formula to estimate the approximate surface area if height and weight be known. 1916. *Nutrition*. 1989;5(5):303-311; discussion 312.
28. ISO. 9920:2007, *Ergonomics of the Thermal Environment - Estimation of Thermal Insulation and Water Vapour Resistance of a Clothing Ensemble.*; 2007. <https://www.iso.org/standard/39257.html>. Accessed July 15, 2021.
29. Wang SK. HANDBOOK OF AIR CONDITIONING AND REFRIGERATION. *McGraw-Hil*. 2001.
30. Lundgren P, Henriksson O, Kuklane K, Holmér I, Naredi P, Björnstig U. Validity and reliability of the Cold Discomfort Scale: A subjective judgement scale for the assessment of patient thermal state in a cold environment. *J Clin Monit Comput*. 2014;28(3):287-291. doi:10.1007/s10877-013-9533-7
31. Bakker LEH, Boon MR, van der Linden RAD, et al. Brown adipose tissue volume in healthy lean south Asian adults compared with white Caucasians: A prospective, case-controlled observational study. *Lancet Diabetes Endocrinol*. 2014;2(3):210-217. doi:10.1016/S2213-8587(13)70156-6
32. Schindelin J, Arganda-Carreras I, Frise E, et al. Fiji: An open-source platform for biological-image analysis. *Nat Methods*. 2012;9(7):676-682. doi:10.1038/nmeth.2019
33. Hasenclever D, Kurch L, Mauz-Körholz C, et al. qPET - A quantitative extension of the Deauville scale to assess response in interim FDG-PET scans in lymphoma. *Eur J Nucl Med Mol Imaging*. 2014;41(7):1301-1308. doi:10.1007/s00259-014-2715-9
34. Sanchez-Delgado G, Martinez-Tellez B, Acosta FM, et al. Brown Adipose Tissue Volume and Fat Content are Positively Associated with Whole-Body Adiposity in Young Men, Not in Women. *Diabetes*. April 2021:db210011. doi:10.2337/db21-0011
35. Bredella MA. Sex differences in body composition. In: *Advances in Experimental Medicine and Biology*. Vol 1043. Springer New York LLC; 2017:9-27. doi:10.1007/978-3-319-70178-3_2

36. Kaikaew K, van den Beukel JC, Neggers SJM, Themmen APN, Visser JA, Grefhorst A. Sex difference in cold perception and shivering onset upon gradual cold exposure. *J Therm Biol.* 2018;77:137-144. doi:10.1016/j.jtherbio.2018.08.016
37. Havenith G. Human surface to mass ratio and body core temperature in exercise heat stress - A concept revisited. *J Therm Biol.* 2001;26(4-5):387-393. doi:10.1016/S0306-4565(01)00049-3
38. Ivanova YM, Swibas T, Haman F, et al. Sex Disparities in Thermoregulatory and Metabolic Responses to Mild Cold Exposure Largely Explained by Differences in Body Mass and Body Surface Area. *J Endocr Soc.* 2021;5(Suppl 1):A326. doi:10.1210/JENDSO/BVAB048.665
39. Van Der Lans AAJJ, Hoeks J, Brans B, et al. Cold acclimation recruits human brown fat and increases nonshivering thermogenesis. *J Clin Invest.* 2013;123(8):3395-3403. doi:10.1172/JCI68993
40. Remie CME, Moonen MPB, Roumans KHM, et al. Metabolic responses to mild cold acclimation in type 2 diabetes patients. *Nat Commun.* 2021;12(1):1-10. doi:10.1038/s41467-021-21813-0
41. Tan CL, Knight ZA. Regulation of Body Temperature by the Nervous System. *Neuron.* 2018;98(1):31-48. doi:10.1016/j.neuron.2018.02.022
42. Lømo T, Eken T, Bekkestad Rein E, Njå A. Body temperature control in rats by muscle tone during rest or sleep. *Acta Physiol (Oxf).* 2020;228(2). doi:10.1111/APHA.13348
43. Sun L, Verma S, Michael N, et al. Brown Adipose Tissue: Multimodality Evaluation by PET, MRI, Infrared Thermography, and Whole-Body Calorimetry (TACTICAL-II). *Obesity.* 2019;27(9):1434-1442. doi:10.1002/oby.22560



Chapter 3

The Infrared Thermography Toolbox:
An Open-access Semi-automated
Segmentation Tool for Extracting Skin
Temperatures in the Thoracic Region
including Supraclavicular Brown
Adipose Tissue

This chapter has been published in: Journal of Medical Systems (2022) PMID:
36319877.

Aashley S.D. Sardjoe Mishre
Maaike E. Straat
Borja Martinez-Tellez
Andrea Mendez Gutierrez
Sander Kooijman
Mariëtte R. Boon
Oleh Dzyubachyk
Andrew Webb
Patrick C. N. Rensen
Hermien E. Kan

ABSTRACT

Introduction: Infrared thermography (IRT) is widely used to assess skin temperature in response to physiological changes. Yet, it remains challenging to standardize skin temperature measurements over repeated datasets. We developed an open-access semi-automated segmentation tool (the IRT-toolbox) for measuring skin temperatures in the thoracic area to estimate supraclavicular brown adipose tissue (scBAT) activity, and compared it to manual segmentations.

Methods: The IRT-toolbox, designed in Python, consisted of image pre-alignment and non-rigid image registration. The toolbox was tested using datasets of 10 individuals (BMI=22.1±2.1 kg/m², age=22.0±3.7 years) who underwent two cooling procedures, yielding four images per individual. Regions of interest (ROIs) were delineated by two raters in the scBAT and deltoid areas on baseline images. The toolbox enabled direct transfer of baseline ROIs to the registered follow-up images. For comparison, both raters also manually drew ROIs in all follow-up images. Spatial ROI overlap between methods and raters was determined using the Dice coefficient. Mean bias and 95% limits of agreement in mean skin temperature between methods and raters were assessed using Bland-Altman analyses.

Results: ROI delineation time was four times faster with the IRT-toolbox (01:04min) than with manual delineations (04:12min). In both anatomical areas, there was a large variability in ROI placement between methods. Yet, relatively small skin temperature differences were found between methods (scBAT: 0.10°C, 95%LoA[-0.13 to 0.33°C] and deltoid: 0.05°C, 95%LoA[-0.46 to 0.55°C]). The variability in skin temperature between raters was comparable between methods.

Conclusion: The IRT-toolbox enables faster ROI delineations, while maintaining inter-user reliability compared to manual delineations.

3.1 INTRODUCTION

Infrared thermography (IRT) is a non-invasive, safe and inexpensive imaging technique for assessing surface temperature. The working principle behind IRT is that all objects emit infrared radiation¹. The intensity and wavelength of the emanated radiation can be used to calculate surface temperatures, which are displayed as colored heatmaps.

IRT is used to study the relation between thermal physiology and skin temperature in humans², and has been utilized for the diagnosis of breast cancer, diabetic neuropathy and peripheral vascular disorders³. There has been increasing interest in utilizing IRT for assessing thermogenic activity induced by brown adipose tissue (BAT)⁴. BAT is a thermogenic tissue found in mammals, with cold exposure being its most potent physiological activator^{5,6}. Upon activation, BAT combusts triglyceride-derived fatty acids and glucose, producing heat due to the presence of uncoupling protein 1 (UCP-1) in its mitochondria. Previous studies have employed IRT to assess BAT activity by measuring skin temperature in the supraclavicular region, the location of the largest BAT depot in humans⁷⁻⁹.

Although IRT has been used for many clinical applications, it is challenging to standardize repeated measurements from a region of interest (ROI). Manual ROI delineations are time-consuming and have a poor spatial reproducibility^{4,10}. Fully automated ROI extraction methods have been developed for several anatomical regions^{10,11}. However, these methods rely on approaches such as clustering, thresholding or edge-detection, which cannot be easily applied to regions with irregular structures or low tissue contrast such as in the supraclavicular area¹⁰. Semi-automated ROI extraction methods, requiring some manual input, are faster than manual methods¹²⁻¹⁴. Law et al. developed a semi-automated ROI method for extracting supraclavicular skin temperature¹², which improved analysis speed while maintaining reproducibility of manual delineations.

However, these semi-automated ROI methods still require manual input for defining the ROI on all images within a dataset. This makes the analysis in studies with large cohorts and/or multiple interventions challenging, particularly when there are differences in subject orientation and positioning with respect to the thermal camera. These challenges can potentially be overcome by using non-rigid image registration, which enables a pixel-by-pixel overlap between the baseline image and every follow-up image. A single baseline ROI can be chosen, which can be directly transferred to all registered follow-up images. In this work, we have developed an open access semi-automated toolbox using non-rigid image registration for measuring skin temperatures in two regions of the thoracic area. We compared the toolbox with manual delineations for analysis time, ROI placement and inter-user reliability.

3.2 MATERIALS AND METHODS

3.2.1 The main features of the IRT-toolbox

The IRT-toolbox was implemented using Python (Python Software Foundation. Python Language Reference (v3.8.5)). Thermal images were initially saved in JPEG format and subsequently converted to temperature maps using the Python package: Flir Image Extractor (v1.4.0). The ExifTool application was used to extract metadata from the thermal images¹⁵. We did not use any commercially available software development kit to analyse our images. The main features of the toolbox are: image pre-alignment, non-rigid image registration and semi-automated ROI segmentation.

Image pre-alignment and non-rigid image registration

The challenge of repeated measurements is summarized in **Figs. 1a** and **1b**. Four images were acquired at different times, and ROIs were manually drawn in the supraclavicular and deltoid regions on each image. The data show that there are differences in the position and orientation of the subject. These lead, as shown in **Fig. 1b**, to spatial differences in the ROIs drawn for the two areas in the four images. **Figs. 1c-e** show the main features of the toolbox. In **Fig. 1c**, image pre-alignment was used to correct for large displacements between images: the neck was used as an anatomical landmark. The spatial coordinates of the neck were calculated for all images in each dataset and used to align each follow-up image to the baseline image. The neck coordinates were determined based on image thresholding, wherein the background was separated from the subject. Along each row of the image (*x*-direction; see **Fig. 1**), temperature differences were determined for consecutive pixels. This yielded a temperature gradient for each row, with minor differences in homogenous regions, and large peaks at transitions between the background (room temperature $\sim 22^\circ\text{C}$) and the body ($34.3\pm 0.5^\circ\text{C}$, at thermoneutrality and $29.9\pm 1.7^\circ\text{C}$ after cooling¹⁶). Pixels that were located between the transition peaks were given a value of 1 if their temperature values were above 25°C (foreground pixels), whereas the other pixels in that same row were given a value of zero (background pixels). This was applied to all rows, until the body was fully separated from the background. Subsequently, the neck was located as the row corresponding to the smallest number of foreground pixels. The outer left *x* and *y* coordinates of the neck were used to shift each follow-up image towards the outer left *x* and *y* coordinates of the neck in the baseline image. The number of pixels were converted to centimeters, and reported as the amount of subject displacement prior to the image pre-alignment and registration steps.

The next step was to account for any geometric differences in the acquired images. Non-rigid image registration was integrated into the toolbox using the open-source image registration toolbox Elastix¹⁷. Non-rigid image registration enables a stepwise deformation of an image until it fully overlaps with a given reference image (*e.g.*, a baseline image).

Registration parameters including the number of resolutions, number of iterations and the maximum step length of the optimizer were systematically optimized based on an image similarity metric, Mattes mutual information. As a quantitative indicator for the registration quality, it was evaluated whether the Mattes mutual information stabilized along the stepwise image deformation for each registration case. Image pre-alignment and non-rigid image registration were both implemented to obtain a pixel-wise image overlap between the reference image and every subsequent image within a participant's dataset (**Fig. 1c**). As a result, ROIs only needed to be delineated on the reference image and this reference ROI could be subsequently transferred to the registered follow-up images (**Fig. 1d**), requiring no redrawing as shown in **Fig. 1e**.

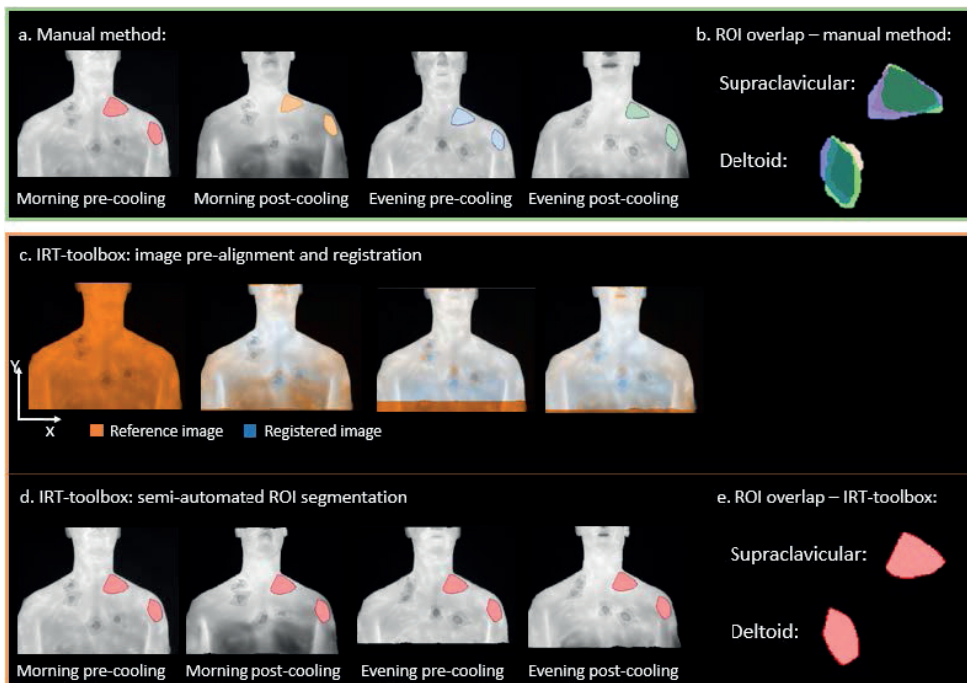


Figure 1. A schematic overview of manual delineations and the IRT-toolbox

a. Manual method: regions of interest were manually delineated on the reference image (morning pre-cooling) and the follow-up images (morning post-cooling, evening pre-cooling and evening post-cooling) in each dataset. **b.** The overlap between manually-delineated ROIs in the supraclavicular and deltoid areas is shown for one participant. Follow-up ROIs were aligned with the reference ROI. **c.** IRT-toolbox: image pre-alignment and image registration were applied to obtain a pixel-wise image correspondence between registered follow-up images (blue) and the reference image (orange) within a single dataset. **d.** The ROI that was manually drawn on the reference image (step **a**), was mapped to the registered follow-up images. **e.** Mapping of the reference ROI removed the variability in manual ROI placement. ROI: region of interest.

3.2.2 Study subjects and experimental procedures

Data were obtained from four healthy males and six healthy females (BMI=22.1±2.1 kg/m², age=22.0±3.7 years) who were enrolled in a clinical trial studying the circadian rhythm of cold-induced thermogenesis¹⁶. This study was approved by the Medical Ethical Committee of the Leiden University Medical Center and performed in accordance with the principles of the revised Declaration of Helsinki. Informed consent was obtained from all participants. The clinical trial was registered at ClinicalTrials.gov NCT04406922. The study design is extensively described elsewhere¹⁶.

Participants underwent a personalized cooling procedure on two separate study days: in the morning (07:30 AM) and in the evening (07:30 PM). The examination room had an average room temperature of 22.0±0.3°C in the morning and 22.4±0.4°C in the evening. At the start of each study visit, an IRT image of the upper thorax/neck region was obtained using the FLIR T530 camera (FLIR Systems, Inc., Wilsonville, OR, USA). The camera was equipped with a 24° AutoCal™ lens and had an image capture rate of 30 Hz. The distance between the camera and the participant was 1.5 meters and the camera was held orthogonally (90°) with respect to the participant. At the end of the cooling procedure, a second IRT image of the upper thorax/neck region was made. Overall, four IRT images were acquired per participant: morning pre-cooling, morning post-cooling, evening pre-cooling and evening post-cooling. The camera acquired an image with the size of 320 pixels (x direction) and 240 pixels (y direction) (**Fig. 1**), which was converted to centimeters¹⁸ using the focal length (17 mm) and distance (1.5 m) between the camera and subject: the image size was 63 x 47 cm.

3.2.3 ROI segmentation

Two researchers (ASM and AMG; hereinafter ‘raters’) delineated ROIs in the supraclavicular and deltoid areas manually on the baseline image (morning pre-cooling, **Fig. 1a**). The supraclavicular depot was segmented using a triangular shape placed between the end of the neck and above the clavicular bone, which has been used in previous IRT studies to simplify manual delineations between raters¹⁹. The deltoid area was delineated by placing a polygon in the upper arm. The raters drew ROIs on all follow-up images to compare results with semi-automated segmentations. The manual morning pre-cooling ROI was used in the semi-automated analysis (IRT-toolbox), and directly applied to the registered follow-up images (*i.e.* morning post-cooling, evening pre-cooling and evening post-cooling) in each dataset. We refer to the morning pre-cooling image as the “reference image”, and the morning pre-cooling ROI as the “reference ROI”. ROIs were delineated in Matlab (version 2016a) using a custom-built function that enabled the user to draw polygons by mouse-clicking. ROIs were subsequently exported to Python for analysis. Of note, the current version of the IRT-toolbox is fully designed in Python, including the delineation step.

3.2.4 Statistical analysis

Mean and maximum skin temperatures were determined for all four imaging conditions from manually drawn ROIs and from the reference ROI directly applied to the registered images in each dataset (IRT-toolbox). These outcome measures were used to assess the variability between segmentation methods (intra-rater variability) and between raters (inter-rater variability). Data normality was tested using the Shapiro-Wilk test.

The assessment of spatial agreement and temperature outcomes between the IRT-toolbox and manual segmentations

In the first analysis, we assessed the spatial overlap between methods, where we compared the overlap of the reference ROI (*i.e.* the ROI drawn on the reference image, that was directly used on registered follow-up images with the IRT-toolbox) with each manually drawn follow-up ROI. Since there were large displacements between the reference image and follow-up images, follow-up ROIs needed to be registered first to match the location of the reference ROI. The spatial overlap was then quantified using the Dice coefficient. The Dice coefficient was determined based on formula (1), wherein the overlapping area of two ROIs A and B is divided by the total number of pixels in both ROIs.

$$Dice(A,B) = \frac{2|A \cap B|}{|A| + |B|} = \frac{2 \cdot \text{Area of overlap}}{\text{total number of pixels in both ROIs}} \quad (1)$$

This overlap coefficient is reported for each anatomical region as mean and range: [min, max], wherein ROIs from both raters were included. The qualitative scores for the Dice coefficient were defined as 0–0.49 (poor), 0.5–0.69 (moderate), 0.7–0.89 (good), and >0.9 (excellent)²⁰. Subsequently, mean and maximum skin temperatures from the two raters were averaged to determine the mean skin temperature difference (mean bias) between methods, and to detect the variability between methods using the 95% limits of agreement (95%LoA) using a repeated measures Bland-Altman analysis (R Core Team v4.1.0 (2021), R Foundation for Statistical Computing, Vienna, Austria; R package: SimplyAgree).

The assessment of the inter-user reliability with the IRT-toolbox versus manual segmentations

In the second analysis, the performance of the IRT-toolbox and the manual method were assessed by evaluating the outcomes between raters. The Dice coefficient was used to determine the spatial agreement between ROIs delineated by the two raters. For the IRT-toolbox, the spatial agreement between the reference ROIs was assessed, resulting in 10 ROIs (*i.e.*, 1 ROI per subject) being compared between raters. For the manual method, all manually drawn reference and follow-up ROIs were included, and therefore 40 ROIs (*i.e.*, 4 ROIs per subject) were compared between raters. Subsequently, the mean bias and 95% LoA in mean and maximum skin temperature between raters were determined for each method. Finally, the ROI drawing time of the supraclavicular region of the whole

dataset was recorded for both segmentation methods for one rater. The registration time for a single image and the time required to register the entire dataset were also recorded. Statistical analyses were performed using SPSS (Statistical Package for the Social Sciences; v25).

3.3 RESULTS

3.3.1 The IRT-toolbox reduces the ROI delineation time to a single image per dataset

The average amount of subject displacement in the follow-up images relative to the reference image, prior to applying the IRT-toolbox, was 3.6 ± 2.5 cm along the y direction and 7.5 ± 5.4 cm along the x direction. After performing the image pre-alignment step, this initial displacement between images was reduced to zero. The optimized image registration parameters were: two-dimensional B-spline transform with a 10×10 mm² grid, adaptive stochastic gradient descent with four resolutions, maximum step length of 0.5 and 450 iterations. In all datasets, image overlap and convergence of the image similarity index were visually assessed by one rater. Image registration took 38 seconds per image pair, and 21:13 min for the entire dataset. The total time for drawing supraclavicular ROIs for the entire dataset, *i.e.*, on all reference-and follow-up images, was 04:12 min using the manual method and 01:04 min with the IRT-toolbox.

3.3.2 Intra-rater analysis: the agreement between ROIs from the IRT-toolbox and manual method showed a wide range, but skin temperature differences were less than 1°C

First, we assessed the spatial overlap and skin temperature outcomes between the IRT-toolbox and manual segmentations. To assess the spatial overlap between methods, we compared the overlap between the reference ROI with each manually drawn follow-up ROI. We found a good agreement, albeit with a wide range, between reference ROIs and manually drawn follow-up ROIs in the supraclavicular area (Dice=0.75, range: [0.42-0.93]), and a moderate agreement in the deltoid area (Dice=0.66, range: [0.30-0.92]; see **Table 1**).

A mean temperature difference of 0.10°C, 95% LoA=[-0.13 °C,0.33 °C] was found for the supraclavicular area, and 0.05°C, 95% LoA=[-0.46 °C,0.55 °C] for the deltoid area; see **Figs. 2a,b**. The results for maximum skin temperature are shown in **Online resource 1; Fig. S1**

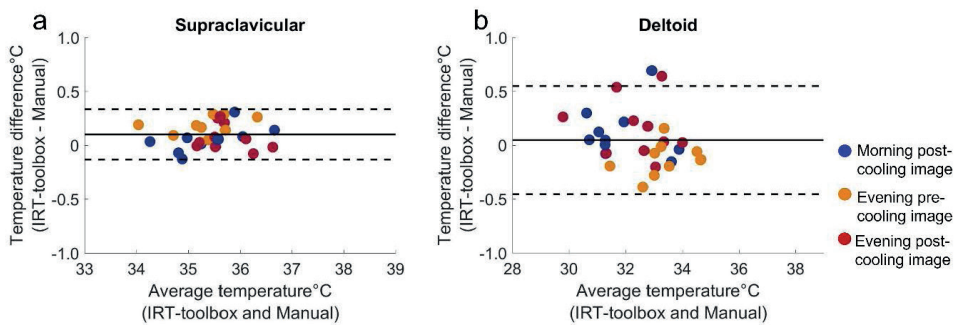
Table 1. The agreement in ROI placement between methods and raters

	1. Methods	2. Raters	
		IRT-toolbox	Manual method
Supraclavicular area	Dice=0.75, range: [0.42,0.93]	Dice=0.73, range: [0.62-0.84]	Dice=0.70, range: [0.56-0.86]
Deltoid area	Dice= 0.66, range: [0.30,0.92]	Dice=0.75, range: [0.58-0.83]	Dice=0.65, range: [0.38-0.83]

Table 1. The agreement in ROI placement between methods and raters

1. Methods: the spatial agreement between ROIs from the IRT-toolbox (reference ROI) and all manually-drawn follow-up ROIs. 2. Raters: the spatial agreement between raters when using the IRT-toolbox and the manual method. The spatial agreement was quantified with the Dice coefficient and the qualitative scores were: 0–0.49 (poor), 0.5–0.69 (moderate), 0.7–0.89 (good) and >0.9 (excellent). Dice coefficient is presented as mean, range: [min,max].

Intra-rater variability in mean skin temperature

**Figure 2. The mean difference and variability in mean skin temperature between methods**

The mean difference and variability in mean skin temperature between methods for the supraclavicular area (a) and the deltoid area (b) are shown. Data for all ten participants are shown; different colors represent different imaging sessions. The solid line represents the mean difference and the dashed lines represent the upper and the lower 95% limits of agreement.

3.3.3. Inter-rater analysis: the IRT-toolbox has a similar inter-user variability to manual segmentations

Secondly, we assessed spatial agreement and temperature outcomes between the two raters for both methods. The IRT-toolbox revealed a good spatial overlap between reference ROIs from the two raters in the supraclavicular region (Dice=0.73, range: [0.62-0.84]), and in the deltoid region (Dice=0.75, range: [0.58-0.83]). For the manual method, a good spatial overlap in the supraclavicular region (Dice=0.70, range: [0.56-0.86]), and a moderate overlap in the deltoid region (Dice=0.65, range: [0.38-0.83]) were found; see **Table 1**.

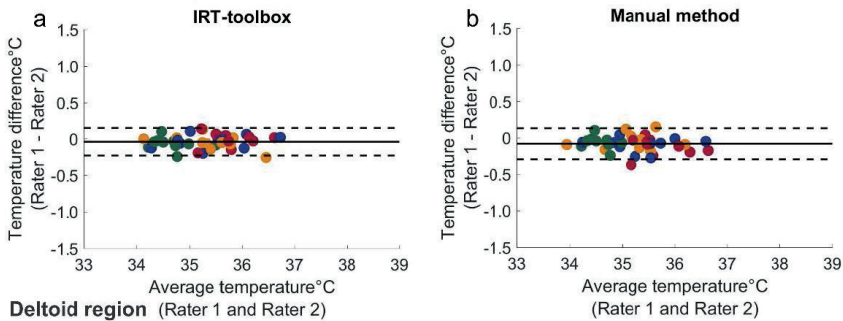
Regarding the skin temperature outcomes between the two raters, the mean supraclavicular skin temperature differences between raters were -0.04 °C, 95% LoA= $[-0.23$ °C, 0.14 °C]

using the IRT-toolbox, and $-0.09\text{ }^{\circ}\text{C}$, 95% LoA= $[-0.30\text{ }^{\circ}\text{C}, 0.12\text{ }^{\circ}\text{C}]$ using manual segmentations; see **Figs. 3a,b**.

The mean deltoid skin temperature difference between raters was $0.14\text{ }^{\circ}\text{C}$, 95% LoA= $[-0.32\text{ }^{\circ}\text{C}, 0.59\text{ }^{\circ}\text{C}]$ using the IRT-toolbox, and $0.14\text{ }^{\circ}\text{C}$, 95% LoA= $[-0.33\text{ }^{\circ}\text{C}, 0.62\text{ }^{\circ}\text{C}]$) with manual segmentations; see **Figs. 3c,d**. The results for the maximum skin temperature are shown in **Online resource 1; Fig. S2**. Temperature gradients in the supraclavicular area and the deltoid region were determined to evaluate the homogeneity of the temperature distributions in both areas. Results are shown in **Online resource 1; Fig. S3**.

Inter-rater variability in mean skin temperature

Supraclavicular region



Deltoid region (Rater 1 and Rater 2)

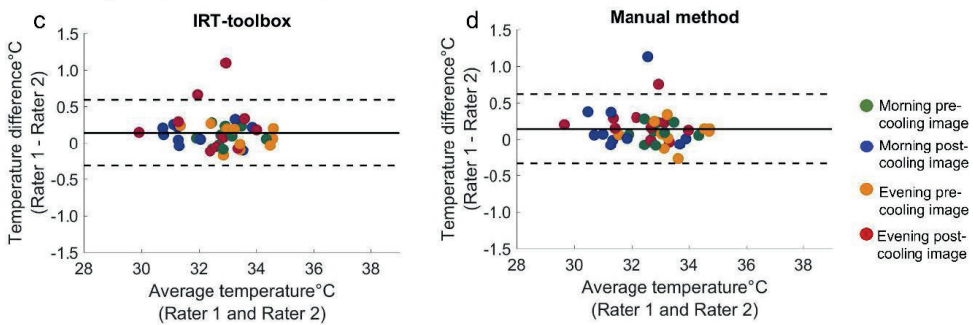


Figure 3. The mean difference and variability in mean skin temperature between raters

The mean difference and variability in mean skin temperature in the supraclavicular area (a, b) and deltoid area (c, d) between two raters using the IRT-toolbox and the manual method are shown. Data for all ten participants are shown; different colors indicate different imaging sessions. The solid line represents the mean difference and the dashed lines represent the upper and the lower 95% limits of agreement.

3.4 DISCUSSION

In this work, we developed an open-access semi-automated segmentation method, and compared it to manual delineations. The IRT-toolbox effectively reduced the ROI drawing time to a single image per dataset. Importantly, our method showed a similar inter-user variability to manual segmentations.

In previous work, semi-automated ROI delineations took longer when moderate displacements were present¹²: in a semi-automated analysis without non-rigid registration, manual input is still needed on all images. Our results show that the image pre-alignment and image registration steps of the IRT-toolbox successfully accounted for displacements. This enabled ROI drawing on the reference image only, and therefore the total drawing time was reduced.

The mean spatial overlap between the reference ROI and manually delineated ROIs was good for the supraclavicular region, and moderate for the deltoid region. For both regions, however, a large variability in spatial overlap was found between methods, which is likely due to differences in ROI placement and size of manually drawn follow-up ROIs. The IRT-toolbox minimizes such variability by utilizing a single ROI applied to all registered follow-up images. Although a large variability was found in ROI placement between methods, skin temperature differences were relatively small ($< 1^{\circ}\text{C}$) for both areas.

The IRT-toolbox showed the same inter-user variability in skin temperature outcomes as manual segmentations in both areas. The IRT-toolbox improved the spatial agreement between the ROIs from the two raters in the deltoid area compared to manual segmentations (good versus moderate), whereas both methods scored the same for the supraclavicular area (good). This difference may be due to the larger size of the deltoid area compared to the supraclavicular area.

The variability in ROI placement and ROI size between methods and raters do not seem to influence differences in skin temperature outcomes, most likely due to relatively small temperature gradients between the region of interest and surrounding tissues (**Online resource 1; Fig. S3**). Hence, the IRT-toolbox may further minimize the variability between users in future applications that involve tissues with more heterogenous temperature distributions.

3.4.1 Practical implications, limitations and future directions

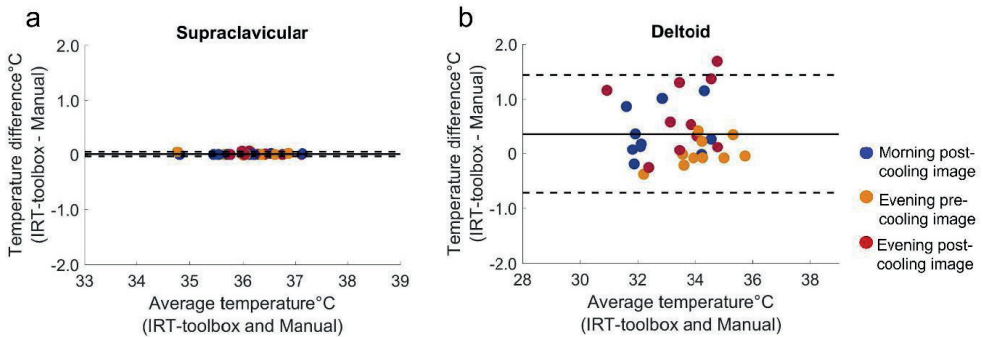
The IRT-toolbox is an open-access, freely available method for temperature analyses and available for clinical applications. The semi-automated part of the program reduces drawing time to a single image per participant, which makes it favorable in studies with

repeated measurements. A limitation of this study is that no calibration procedures were performed prior to imaging, and no corrections were made for the environmental variance between imaging conditions. This will not have influenced our results since we did not determine skin temperature differences between different imaging conditions (i.e., morning pre-cooling and evening pre-cooling), but determined skin temperature differences between segmentation methods and raters where ROIs were applied to the same image for comparison. Nevertheless, we do recommend to perform these kind of corrections to enable more accurate estimates of supraclavicular skin temperature changes between different imaging sessions. In addition, the detected pixel in the IRT image had a size of 0.2 cm based on the instantaneous field of view (iFOV) of 1.308 mrad and a target distance of 1.5 meters^{18,21}. The thermal measurement area that corresponded to 1 cm² consisted of 25 pixels. It should be taken into account that this measurement area had a minimal variation in the two-dimensional IRT image since the body surface is not flat and the pixel area is not infinitely small. A limitation of the IRT-toolbox is the registration time. However, this step has to be performed only once in the analysis and a built-in function of the program allows users to automatically run the image registration part consecutively on multiple datasets. Another limitation is that the IRT-toolbox can only be used in thermal images, where anatomical regions have a sufficiently different temperature compared to the background, such as in imaging the feet in diabetes²². In this case, an additional color (i.e., Red Green Blue, RGB) image might need to be integrated. The IRT-toolbox may be optimized by automating the method using e.g., skin fiducials, anatomical landmarks and/or artificial networks, and combined with high-end computers. This will further minimize user workload and may fully eliminate the variability between raters.

In conclusion, we introduced a new semi-automated segmentation tool to facilitate temperature analyses of supraclavicular and deltoid skin temperatures. The IRT-toolbox reduced the ROI delineation time and showed a comparable inter-user variability with respect to manual segmentations.

SUPPLEMENTARY DATA

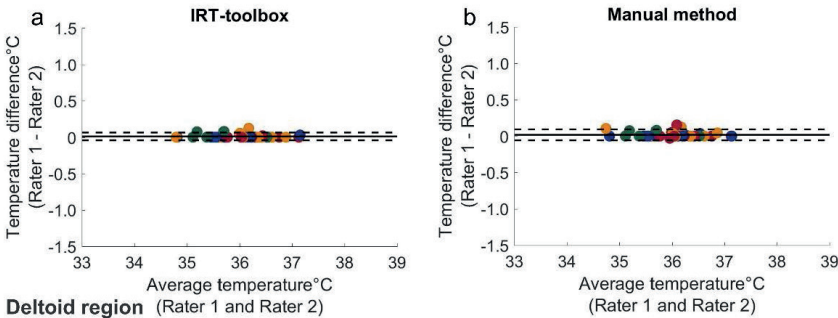
Intra-rater variability in maximum skin temperature



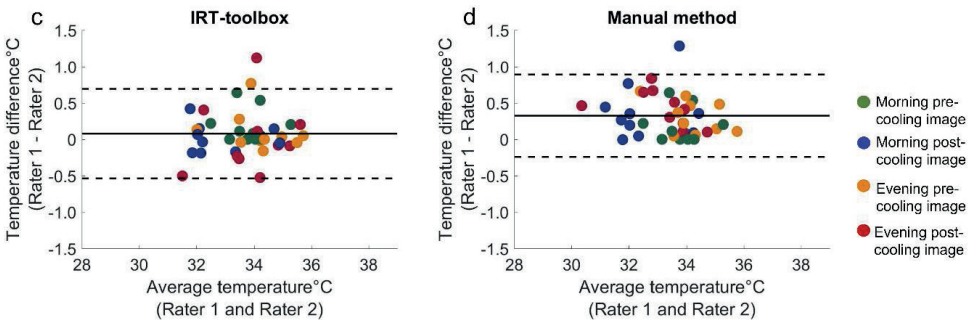
Supplemental Figure 1. The mean difference and variability in maximum skin temperature between methods
 The mean difference and variability in maximum skin temperature between methods for the supraclavicular area (a) and the deltoid area (b) are shown. Data for all ten participants are shown; different colors represent different imaging conditions. The solid line represents the mean difference and the dashed lines represent the upper and the lower 95% limits of agreement.

Inter-rater variability in maximum skin temperature

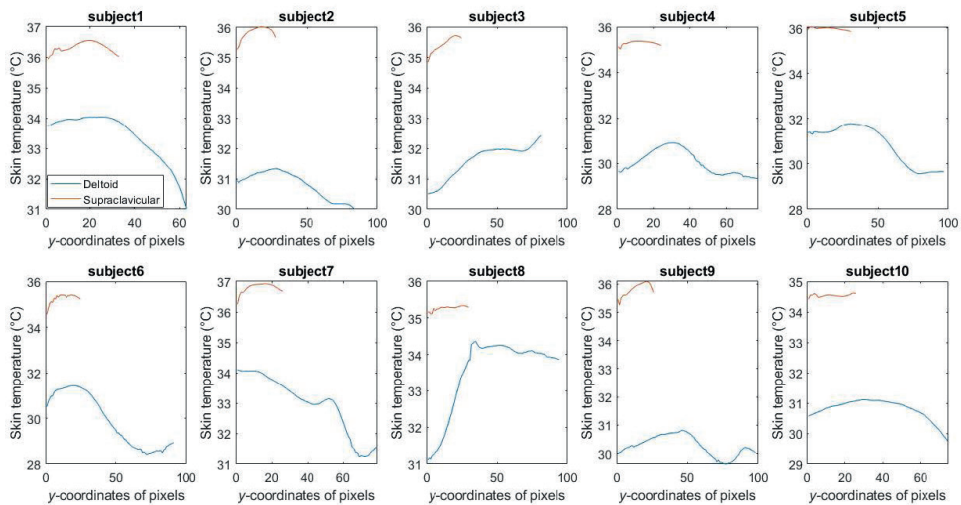
Supraclavicular region



Deltoid region



Supplemental Figure 2. The mean difference and variability in maximum skin temperature between raters
 The mean difference and variability in maximum skin temperature in the supraclavicular area (a, b) and deltoid area (c, d) between two raters using the IRT-toolbox and the manual method is shown. Data for all ten participants are shown; different colors indicate different imaging conditions. The solid line represents the mean difference and the dashed lines represent the upper and the lower 95% limits of agreement.



Supplemental Figure 3. Temperature distribution in the deltoid and supraclavicular regions.

Skin temperature values along a vertical line passing through the deltoid region (blue) and the supraclavicular region (red) are plotted.

REFERENCES

1. Speakman J, Fischer Verlag G, Speakman JR, Ward S. Infrared thermography : principles and applications. *ZOOLOGY*. 1998;101:224-232.
2. Ring FJ. Pioneering progress in infrared imaging in medicine. *Quant Infrared Thermogr J*. 2014;11(1):57-65. doi:10.1080/17686733.2014.892667
3. Lahiri BB, Bagavathiappan S, Jayakumar T, Philip J. Medical applications of infrared thermography: A review. *Infrared Phys Technol*. 2012;55(4):221-235. doi:10.1016/J.INFRARED.2012.03.007
4. Law J, Chalmers J, Morris DE, Robinson L, Budge H, Symonds ME. The use of infrared thermography in the measurement and characterization of brown adipose tissue activation. *Temp Multidiscip Biomed J*. 2018;5(2):147. doi:10.1080/23328940.2017.1397085
5. Cannon B, Nedergaard J. Brown Adipose Tissue: Function and Physiological Significance. *Physiol Rev*. 2004;84(1):277-359. doi:https://doi.org/10.1152/physrev.00015.2003
6. Leitner BP, Huang S, Brychta RJ, et al. Mapping of human brown adipose tissue in lean and obese young men. *Proc Natl Acad Sci U S A*. 2017;114(32):8649-8654. doi:10.1073/pnas.1705287114
7. Sun L, Verma S, Michael N, et al. Brown Adipose Tissue: Multimodality Evaluation by PET, MRI, Infrared Thermography, and Whole-Body Calorimetry (TACTICAL-II). *Obesity*. 2019;27(9):1434-1442. doi:10.1002/oby.22560
8. Jang C, Jalapu S, Thuzar M, et al. Infrared thermography in the detection of brown adipose tissue in humans. *Physiol Rep*. 2014;2(11):e12167. doi:10.14814/PHY2.12167
9. J L, DE M, C I-E, et al. Thermal Imaging Is a Noninvasive Alternative to PET/CT for Measurement of Brown Adipose Tissue Activity in Humans. *J Nucl Med*. 2018;59(3):516-522. doi:10.2967/JNUMED.117.190546
10. Singh J, Arora AS. Automated approaches for ROIs extraction in medical thermography: a review and future directions. *Multimed Tools Appl 2019 7921*. 2019;79(21):15273-15296. doi:10.1007/S11042-018-7113-Z
11. Lahiri BB, Bagavathiappan S, Jayakumar T, Philip J. Medical applications of infrared thermography: A review. *Infrared Phys Technol*. 2012;55(4):221. doi:10.1016/J.INFRARED.2012.03.007
12. Law JM, Morris DE, Robinson LJ, Symonds ME, Budge H. Semi-automated analysis of supraclavicular thermal images increases speed of brown adipose tissue analysis without increasing variation in results. *Curr Res Physiol*. 2021;4:177-182. doi:10.1016/J.CRPHYS.2021.07.001
13. Vardasca R. Template Based Alignment and Interpolation Methods Comparison of Region of Interest in Thermal Images. In: *3rd Research Student Workshop, Faculty of Advanced Technology Glamorgan Business Center, University of Glamorgan, Pontypridd, UK.* ; 2015:5.
14. Venkataramani K, Mestha LK, Ramachandra L, Prasad SS, Kumar V, Raja PJ. Semi-automated breast cancer tumor detection with thermographic video imaging. *Proc Annu Int Conf IEEE Eng Med Biol Soc EMBS*. 2015;2015-November:2022-2025. doi:10.1109/EMBC.2015.7318783
15. Harvey P. ExifTool. 2016. <https://exiftool.org/>.
16. Straat ME, Martinez-Tellez B, Sardjoe Mishre A, et al. Cold-Induced Thermogenesis Shows a Diurnal Variation That Unfolds Differently in Males and Females. *J Clin Endocrinol Metab*. February 2022:1-10. doi:10.1210/CLINEM/DGAC094
17. Klein S, Staring M, Murphy K, Viergever MA, Pluim JPW. Elastix: A toolbox for intensity-based medical image registration. *IEEE Trans Med Imaging*. 2010;29(1):196-205. doi:10.1109/TMI.2009.2035616
18. Teledyne FLIR systems. https://flir.custhelp.com/app/utils/fl_fovCalc/pn/79301-0101/ret_url/%252Fapp%252Ffl_download_datasheets%252Ffid%252F1052. Accessed January 21, 2022.

19. J L, J C, DE M, L R, H B, ME S. The use of infrared thermography in the measurement and characterization of brown adipose tissue activation. *Temp (Austin, Tex)*. 2018;5(2):147-161. doi:10.1080/23328940.2017.1397085
20. Pons C, Borotikar B, Garetier M, et al. Quantifying skeletal muscle volume and shape in humans using MRI: A systematic review of validity and reliability. *PLoS One*. 2018;13(11):e0207847. doi:10.1371/JOURNAL.PONE.0207847
21. Teledyne FLIR systems. How far can you measure. <https://www.flir.eu/discover/instruments/electrical-mechanical/how-far-can-you-measure-spot-size-ratio/>. Published 2021. Accessed September 14, 2022.
22. Liu C, Netten JJ van, Baal JG van, Bus SA, Heijden F van der. Automatic detection of diabetic foot complications with infrared thermography by asymmetric analysis. *J Biomed Opt*. 2015;20(2):026003. doi:10.1117/1.JBO.20.2.026003



Chapter 4

Human brown adipose tissue estimated with magnetic resonance imaging undergoes changes in composition after cold exposure: an in vivo MRI study in healthy volunteers

This chapter has been published in: *Frontiers in Endocrinology* (2020) PMID: 31998233.

Gustavo Abreu-Vieira*
Aashley S.D. Sardjoe Mishre*
Jedrzejj Burakiewicz
Laura G.M. Janssen
Kimberly J. Nahon
Jari A. van der Eijk
Titia T. Riem
Mariëtte R. Boon
Oleh Dzyubachyk
Andrew G. Webb
Patrick C.N. Rensen
Hermien E. Kan
* Shared first authorship

ABSTRACT

Aim: Magnetic resonance imaging (MRI) is increasingly being used to evaluate brown adipose tissue (BAT) function. Reports on the extent and direction of cold-induced changes in MRI fat fraction and estimated BAT volume vary between studies. Here, we aimed to explore the effect of different fat fraction threshold ranges on outcomes measured by MRI. Moreover, we aimed to investigate the effect of cold exposure on estimated BAT mass and energy content.

Methods: The effects of cold exposure at different fat fraction thresholding levels were analyzed in the supraclavicular adipose depot of nine adult males. MRI data were reconstructed, co-registered and analyzed in two ways. First, we analyzed cold-induced changes in fat fraction, T2* relaxation time, volume, mass and energy of the entire supraclavicular adipose depot at different fat fraction threshold levels. As a control, we assessed fat fraction differences of deltoid subcutaneous adipose tissue (SAT). Second, a local analysis was performed to study changes in fat fraction and T2* on a voxel-level. Thermoneutral and post-cooling data were compared using paired-sample t-tests ($p < 0.05$).

Results: Global analysis unveiled that the largest cold-induced change in fat fraction occurred within a thermoneutral fat fraction range of 30-100% ($-3.5 \pm 1.9\%$), without changing the estimated BAT volume. However, the largest cold-induced changes in estimated BAT volume were observed when applying a thermoneutral fat fraction range of 70-100% ($-3.8\% \pm 2.6\%$). No changes were observed for the deltoid SAT fat fractions. Tissue energy content was reduced from 126 ± 33 kcal to 121 ± 30 kcal, when using a 30-100% fat fraction range, and also depended on different fat fraction thresholds. Voxel-wise comparison showed that while cold exposure changed the fat fraction across nearly all thermoneutral fat fractions, decreases were most pronounced at high thermoneutral fat fractions.

Conclusion: Cold-induced changes in fat fraction occurred over the entire range of thermoneutral fat fractions, and were especially found in lipid-rich regions of the supraclavicular adipose depot. Due to the variability in response between lipid-rich and lipid-poor regions, care should be taken when applying fat fraction thresholds for MRI BAT analysis.

4.1 INTRODUCTION

The main function of brown adipose tissue (BAT) is to convert chemical energy stored within lipids into thermal energy (heat). Exposure to low temperatures is the main physiological stimulus for BAT activation¹. Upon adrenergic stimulation by sympathetic nerves, intracellular lipolysis takes place within brown adipocytes², and the resulting free fatty acids bind to uncoupling protein 1 (UCP1), which, in turn, functions as a molecular gate that dissipates the generated mitochondrial proton gradient as heat. To replenish the intracellular lipid stores, BAT takes up glucose and fatty acids from the systemic circulation^{3,4}.

In rodents, visualization of BAT by magnetic resonance imaging (MRI) was first reported almost three decades ago⁵, and soon the technique was shown to accurately reflect the tissue structure⁶ as well as histological changes due to temperature acclimatization⁷. More recently, with research being expanded towards human physiology, several studies explored this ionizing-radiation-free method with the aim of understanding BAT function⁸.

From preclinical models it is known that the chemically-assessed fat content of tissues matches the fat mass estimated by MRI⁹ and that fat fraction (FF) correlates negatively with the amount of UCP1-expressing cells in BAT¹⁰ and positively with adipocyte size¹¹. In the intrascapular BAT of rodents kept on regular chow and at room temperature (circa 21°C), MRI estimations of FF vary between 20% and 50%, depending on the depth of the tissue¹². However, FF can reach up to almost 80% when animals are kept at thermoneutrality¹³. In infants, BAT resembles the classic intrascapular depot found in rodents, both in morphology and function¹⁴. In adults, however, there is a remarkable lack of easily distinguishable borders for e.g. the supraclavicular depot, which makes it difficult for a consensus to be reached on the optimal FF thresholds that should be used for specific BAT imaging¹⁵. As a consequence, FF within human BAT has variously been described as circa 60%¹⁶, 65%¹⁷, 80%^{18,19} and 94%²⁰ in elderly adults and different FF threshold levels have been used to segment BAT^{19,21–24}. Only one recent study explored the effect of specific FF threshold levels (0-100%, 40-100% and 50-100%) on the cold-induced response in FF²⁵, but no analyses on other MR outcome parameters were explored.

The relaxation time T2* has also been studied as an indirect MRI measure of BAT activity^{16,21,24,26,27}. It has been demonstrated that the T2* of BAT is shorter compared to white adipose tissue (WAT), which is most likely due to the abundant iron-rich mitochondria present in brown adipocytes. Cold-induced BAT activation increases oxygen consumption due to increased metabolic activity, which in turn increases blood perfusion. The latter increases T2*, whereas oxygen consumption shortens T2*²¹. Different reports exist on the

direction of changes in T2* during cold exposure, mostly likely due to these conflicting effects²⁸⁻³⁰.

BAT is naturally heterogeneous: on a molecular scale, this is manifested in differences in UCP-1 protein expression of adjacent cells, which after immunostaining create a multicolored pattern termed the “harlequin phenomenon”³¹. The lack of homogeneity between adipose tissue depots within a single organism has also been noted at the functional level³²⁻³⁴. Although structural heterogeneity has been noted in BAT imaging studies³⁵⁻³⁸, it is generally seen as a confounding factor. Moreover, while the major goal of BAT medical research is to understand and manipulate energy fluxes, the quantification of tissue mass as caloric equivalents is rare. There are a few interesting examples of such a concept being applied, e.g. by matching body composition to potential energy storages and predicting whole-body energy expenditure^{39,40} or inferences concerning BAT energy uptake by estimating the energy content in labeled macromolecules⁴¹. To our knowledge, however, an estimation of BAT energy storages in vivo has not been performed yet.

Given the importance of BAT in current metabolic research, we aimed to explore the effect of different fat fraction threshold ranges on multiple outcomes measured by MRI. Moreover, for the first time, we aimed to investigate the effect of cold exposure on BAT mass and energy content. To this end, we first assessed estimated BAT volumes at thermoneutral and cold conditions to establish a lower FF threshold for the exclusion of non-fatty voxels. Subsequently, we determined estimated BAT volume, FF, T2*, mass and energy content, and explored the effect of different FF thresholds on these parameters. Finally, we assessed local changes in FF and T2* upon cold exposure on a voxel-level. We demonstrate the importance of the high-lipid areas of the tissue and suggest that the conceptual framework of this work could further aid investigations on BAT as a target for obesity and metabolic disorders in humans.

4.2 MATERIALS AND METHODS

4.2.1 Subjects

Ten healthy, non-smoking, lean (BMI 18-25 kg/m²) European male volunteers, born in the Netherlands and aged between 18 and 30 years, were recruited as part of a larger intervention study that investigated the effect of cold exposure and the β 3-receptor agonist mirabegron on BAT (Clinical Trials number: NCT03012113). The study was conducted in accordance with the principles of the revised Declaration of Helsinki (reference: General Assembly of the World Medical (2014). World Medical Association Declaration of Helsinki: ethical principles for medical research involving human subjects. *J Am Coll Dent* 81:14-18.) and with approval from the local medical ethics committee. Exclusion criteria were

recent excessive weight change (> 3 kg within the last 3 months), vigorous exercise, use of any medication known to affect lipid and/or glucose metabolism, BAT activity, cardiac function or QT interval time, smoking and any relevant chronic disease. Contraindications for undergoing an MRI scan were the presence of non-MR-safe metal implants or objects in the body (i.e. a pacemaker, neurostimulator, hydrocephalus or drug pump, non-removable hearing aid or large recent tattoos), and a history of claustrophobia, tinnitus or hyperacusis.

4.2.2 Study design and BAT activation protocol

Subjects were instructed to withhold from alcohol and caffeine for 24 hours and to fast overnight for 10 hours, prior to the experiment. Subjects remained fasted until the end of the experiment. To activate BAT, a personalized cooling protocol was conducted as previously described⁴². Each subject was placed between water-perfused temperature-controlled mattresses with water initially circulating at 32°C. The water temperature was gradually reduced during the first hour until reaching 9°C or reporting of shivering by the subject. In either case the temperature was raised by 3°C and the subject laid for one additional hour under these conditions. In the case of renewed shivering, the temperature was raised slightly to stop shivering and to assure that BAT remained the dominant source of heat production². MRI scans were acquired before and after the cooling protocol on a 3T MRI scanner (Philips Ingenia, Philips Healthcare, Best, the Netherlands). Subjects were positioned supine and head-first in the scanner. Scans were conducted in all at the same time of day in all participants (before cooling: in the morning, after cooling: in the afternoon).

4.2.3 Image acquisition

A three-dimensional six-point chemical-shift encoded gradient-echo acquisition using a 16-channel anterior array, 12-channel posterior array and the posterior section of the 16-channel head and neck coil was used to image the supraclavicular adipose depot (**Fig. 1**). The following imaging parameters were used: repetition time TR=15ms, first echo time TE=1.98ms, echo time separation Δ TE=1.75ms, flip angle=8°, field-of-view of 480 × 300 × 90 mm³ (Right-Left, Foot-Head, Anterior-Posterior), 1.1 mm isotropic resolution, four signal averages. Averaging was done post-acquisition; in the case of significant subject motion the corresponding averages were rejected. Bulk motion due to either shivering or subject discomfort was the major source of motion. The total imaging time was 12 minutes. To increase the reproducibility of subject positioning, the participants were asked to reach as far as possible with their fingers towards their feet after being placed on the scanner table and to relax their shoulders afterwards.

4.2.4 Data reconstruction and analysis

Data reconstruction

Quantitative water and fat images were reconstructed off-line using an in-house water-fat separation algorithm based on the known frequencies of the multi-peak fat spectrum and assuming a mono-exponential $T2^*$, combined with a region-growing scheme to mitigate strong main field inhomogeneity effects. Initially, a low-resolution reconstruction was performed by using an estimate for the main magnetic field inhomogeneity. Subsequently, a region growing scheme was used to extrapolate the solution from correctly reconstructed parts in order to acquire the reconstructed water and fat images at high resolution^{43–46}. FF maps were generated according to the following equation, where x , y and z denote the position of a voxel in the image.

$$\text{Signal fat fraction}(x, y, z) = \frac{\text{Signal}_{\text{Fat}}(x, y, z)}{\text{Signal}_{\text{Fat}}(x, y, z) + \text{Signal}_{\text{Water}}(x, y, z)}$$

Image registration and ROI delineation

Registration was performed using the open-source image registration toolbox Elastix^{47,48}. The first echo of the thermoneutral image stack was registered to that of the post-cooling stack by first pre-aligning them in an affine manner followed by deformable registration with a three-dimensional B-spline transform with a $10 \times 10 \times 10$ mm³ grid. In both cases, an adaptive stochastic gradient descent with two resolutions for optimization and Mattes mutual information was used as the similarity measure. Region masks, defined as the sampled part of each image stack, were used during the registration. The parameter files that were used for performing the registration can be downloaded from <http://elastix.bigr.nl/wiki/index.php/Par0048>. Regions of interest (ROIs) encompassing the known location of the left supraclavicular adipose depot⁴⁹ (**Fig. 1**) were drawn manually on the thermoneutral scans by one observer. Additionally, to ensure that potential changes in FF of the supraclavicular BAT depot were specific to this region, regions of interest comprising deltoid subcutaneous adipose tissue (SAT) were manually delineated on both the thermoneutral and post-cooling scans (**Fig. S1**). To exclude potential bias caused by the direction of registration, we also performed the registration in the reverse direction (post-cooling \rightarrow thermoneutral) and obtained results (not shown) that were virtually identical to the ones reported below.

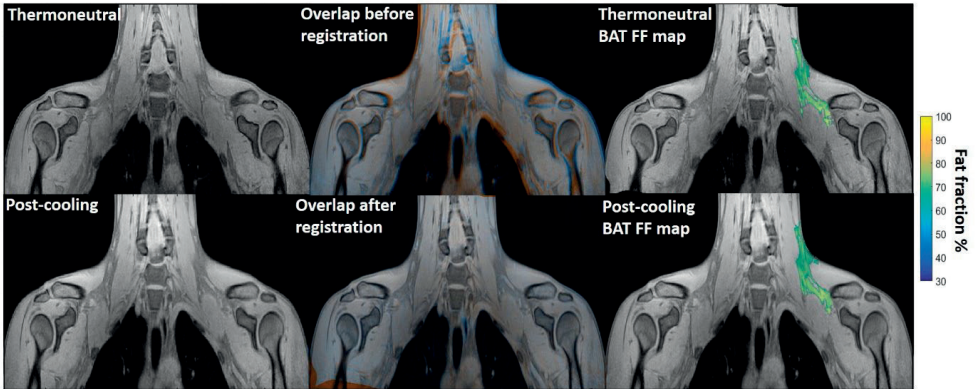


Figure 1. Example of image registration and a reconstructed fat fraction map before and after cooling.

The first column shows thermoneutral and post-cooling images (one slice from the first echo in the acquisition). In the second column, the overlay of the same images before (top) and after registration (bottom) is shown. The images are colored orange (thermoneutral) and blue (post-cooling) for better visualization of differences between the scans. The third column shows the thermoneutral and post-cooling fat fraction maps of the supraclavicular adipose depot, overlaid on the corresponding images. Lipid content in the supraclavicular region is color-mapped over a 30–100% fat fraction range.

Data analysis

Cold-induced changes to the supraclavicular adipose depot were assessed using two complementary analyses. First, changes in FF, $T2^*$, volume, mass and energy content of the supraclavicular adipose depot were assessed using a global analysis. As this analysis only uses the deformation field for ROI mapping on the post-cooling image, this allows not only assessment of FF, but also any changes in estimated BAT volume. Assessment of BAT volume was recently shown to be highly dependent on segmentation criteria in [^{18}F] FDG PET-CT studies⁵⁰. Therefore, we decided to explore the influence of FF segmentation criteria on both estimated BAT volume and FF using MRI.

The estimated BAT volume was determined by multiplying the volume of a single voxel (0.548 μL) by the number of voxels that fall within a certain fat fraction segmentation range (e.g. 30–100% FF). For example: when using a 30–100% FF segmentation threshold range, 93275 voxels were segmented from the thermoneutral image. Multiplied by the volume of a single voxel (0.548 μL), the estimated BAT volume would be 51 mL. Data from this analysis were also used to explore different FF thresholds. Secondly, we performed a local analysis to study changes in FF and the $T2^*$ relaxation time on a voxel-level. As this method directly deforms the thermoneutral images and ROIs to post-cooling image coordinates, no conclusions regarding the true volume can be inferred. Details of the methods are outlined below. Due to excessive movement during image acquisition, MRI data from one participant could not be reconstructed and were excluded from all analyses.

Global analysis : FF_{Glob} , FF_{SAT} , $T2^*_{Glob}$ and Vol_{BAT} .

Global analysis of supraclavicular adipose tissue FF (FF_{Glob}), $T2^*$ relaxation time ($T2^*_{Glob}$) and estimated BAT volume (Vol_{BAT}) was performed by mapping the defined ROIs to the post-cooling image coordinates. To this end, the calculated deformation field from the registration was used to transform the thermoneutral ROIs to the post-cooling scan coordinates. The deformation field of the ROIs was converted to the floating point image type. This enabled performing the analysis on raw (non-interpolated) data. The distribution of thermoneutral and post-cooling Vol_{BAT} across the FF range was assessed using volume histograms with FF bins of 0.5%. This was then assessed statistically by determining at which FF ranges (10% intervals), estimated BAT volume was significantly changed after cold exposure. To explore the effect of different upper and lower FF thresholds for BAT analysis, cold-induced changes in Vol_{BAT} , FF_{Glob} and $T2^*_{Glob}$ were quantified at all FF threshold options. To illustrate these effects, we tested for specific FF ranges: 30–100%, 50–100% and 70–100% whether Vol_{BAT} , FF_{Glob} and $T2^*_{Glob}$ changed significantly after cold exposure. Voxels below the selected lower FF thresholds (i.e., 30%, 50% or 70%) were excluded in both the thermoneutral and post-cooling ROIs.

By plotting the ROIs using different lower FF segmentation thresholds, we observed that voxels within a 10-30% FF interval were mostly located at the boundaries of the supraclavicular adipose depot, which are adjacent to muscle (**Fig. S2**). Therefore, to avoid inclusion of non-fatty tissue and minimize partial volume effects, a lower FF threshold of 30% was adopted for the subsequent analyses.

ROIs comprising deltoid SAT were manually delineated on both thermoneutral and post-cooling scans to preclude analysis bias arising from difficulty registering ROIs located at the interface of tissue and air (**Fig. S1**). The average FF of the deltoid SAT depots (FF_{SAT}) was determined using a 70-100% FF interval before and after cooling to avoid voxels containing muscle and air and to minimize partial volume effects.

Global analysis: estimation of BAT mass and energy content

To estimate BAT mass and energy content, the FF was used to calculate water and fat mass, and, subsequently, the total tissue energy was estimated similarly to³⁹⁻⁴¹. 1 μ L of lipid was assumed to represent 0.92 mg in mass, corresponding to 9.4×10^{-3} kcal. Lean mass measurements were derived from the water MR signal and represent a combination of water-bound structures such as proteins, glucose and intra- extracellular fluids. Lean mass of 1 μ L corresponded to 1.06 mg and 1.0×10^{-3} kcal, correspondingly. Energy variation and lean/fat mass changes were calculated from the FF. Therefore, a voxel of 1 μ L with a FF of 50% is equivalent to 0.5 μ L lean mass and 0.5 μ L fat, which, after adjustments for density, represented 0.455 mg fat and 0.540 mg lean mass.

Voxel-wise analysis: FF_{Loc} and $T2^*_{Loc}$

For voxel-wise analysis of the supraclavicular adipose depot, the deformation field from the registration was used to transform the thermoneutral ROIs, FF and $T2^*$ maps to the post-cooling image coordinates to compare the FF and $T2^*$ on a voxel-level (FF_{Loc} and $T2^*_{Loc}$). To compensate for potential bias due to interpolation of the moving image and small-scale inconsistencies between the co-registered images, each voxel of both thermoneutral and post-cooling image stacks was assigned a mean value from its 3×3 voxel neighborhood.

FF maps were generated to visualize FF composition changes across the supraclavicular adipose depot on a voxel-wise level. Cold-induced FF changes on a voxel level (FF_{Loc}) were further studied using two-dimensional joint histograms. In these plots, for every voxel its initial FF was plotted against its change in FF after cold exposure, and the number of voxels belonging to each combination was added to represent the counts (color scale). Similar voxel density plots were used to assess (i) the relation between thermoneutral $T2^*_{Loc}$ and FF_{Loc} , (ii) the relation between $\Delta T2^*_{Loc}$ after cold exposure and thermoneutral FF measurements, and (iii) the relation between $\Delta T2^*_{Loc}$ and ΔFF_{Loc} after cold exposure. The distributions of thermoneutral FF_{Loc} , ΔFF_{Loc} and $\Delta T2^*_{Loc}$ after cold exposure were assessed using K-means clustering. The Elbow method⁵¹ was used to obtain the optimal cluster number by evaluating the percentage of explained variance as a function of the number of clusters. The explained variance percentage was determined as the ratio of the between-group variance to the total variance. In general, when the explained variance is plotted against cluster number, the first few clusters will add information (explain variance), so these can be observed as jumps from one k-value to another. However, at a certain k-value little information is added, which results in a knee point. For analyzing the voxel distributions, the optimal k-value was determined by visual inspection and implementing a 95% explained variance cut-off value.

4.2.5 Statistical analysis

Data were tested for a normal distribution according to the Shapiro-Wilk test. For the global analysis, comparisons between thermoneutral and post-cooling data were performed by paired Student's t-tests with results deemed statistically significant when $p < 0.05$. No correction for multiple comparisons was performed. For the local analysis we used a voxel-wise comparison, and performed k-means clustering for the analysis. As this approach uses an unsupervised learning algorithm that simply visualizes underlying clusters in the voxel distribution without providing any details regarding the significance of the different clusters, no correction for multiple comparisons is needed⁵¹. Linear regression was used to assess the relation between supraclavicular adipose tissue mass and volume using a 0.05 significance level and the R-squared is given. Data analysis including

statistical analysis was performed in MATLAB (version R2018b). Data are presented as mean±SEM.

4.3 RESULTS

4.3.1 Volumetric changes in estimated BAT volume after cold-exposure

Histogram analysis of the changes in Vol_{BAT} showed an overall shift of the estimated post-cooling BAT volume from higher FFs towards lower FFs (Fig. 2A). When binned into 10% FF intervals, this resulted in significant increases in estimated BAT volume above a FF of 30%, while the estimated BAT volume was significantly decreased above a FF of 80% (Fig. 2B). Interestingly, Vol_{BAT} did not change significantly within the 70-80% FF range, which is at the intersection of the thermoneutral and post-cooling histograms (inset of Fig. 2A).

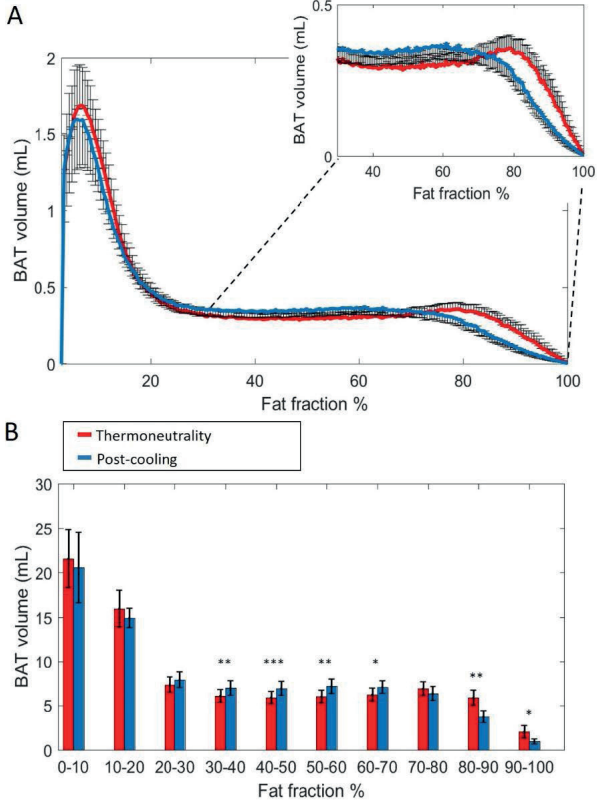


Figure 2. Estimated volumetric BAT analysis
 Thermoneutral and post-cooling volume histograms as a function of fat fraction with bin size 0.5%: thermoneutral volumes are shown in red and post-cooling volumes in blue (A). Cold-induced volume changes plotted as a function of fat fractions (10% FF interval) (B). Data are represented as mean±SEM for n=9. In Figure. 2.B, a paired sample t-test was used to analyze the changes in volume after cold exposure. * p<0.05, **p<0.01 and *** p<0.001.

The effect of different FF threshold options on cold-induced changes in Vol_{BAT} is shown in **Fig. 3A**. For a lower FF threshold of 30% and upper FF threshold of 100%, no clear change in Vol_{BAT} occurred. However, with increasing lower FF threshold values, Vol_{BAT} decreased upon cold exposure. This was subsequently tested for statistical significance for FF ranges with a relatively low (30-100%), intermediate (50-100%) and high (70-100%) lower threshold. For the broadest FF range (30-100%), no significant change was detected in Vol_{BAT} after cold exposure (**Fig. 3B**). For the intermediate FF range (50-100%), Vol_{BAT} lowered from 26.9 ± 2.4 mL to 25.2 ± 2.2 mL (-1.8%; $p=0.031$, **Fig. 3C**) after cold exposure. For the 70-100% FF range, Vol_{BAT} decreased from 14.7 ± 1.8 mL to 11.0 ± 1.5 mL (-3.8%; $p=0.0022$, **Fig. 3D**) after cold exposure.

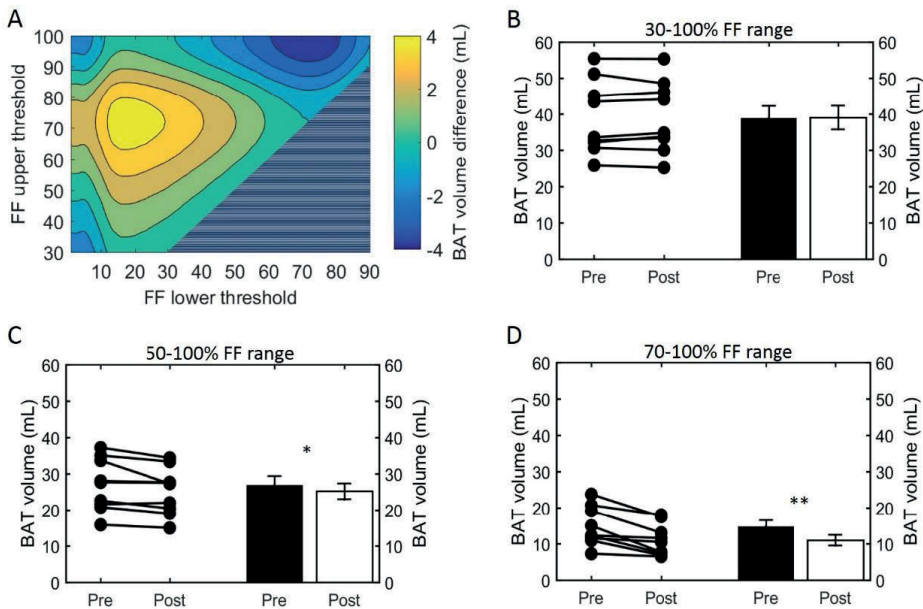


Figure 3. Effect of FF thresholds on estimated BAT volume differences

Heatmap of the effect of different FF segmentation thresholds on estimated BAT volume differences after cooling. The color (second y-axis) depicts the estimated BAT volume difference for each lower (x-axis) and upper left (y-axis) threshold. The largest decrease in estimated BAT volume is present with a lower threshold of 72% and no upper threshold. The triangle in the lower right corner indicates invalid FF threshold options, as we implemented a minimum FF threshold of 30%. (A). Cold-induced volume changes analyzed using the paired sample t-test (* $p<0.05$, ** $p<0.01$) at different threshold ranges: 30-100% (B), 50-100% (C), and 70-100% (D). Data is represented as mean \pm SEM for all participants ($n=9$).

4.3.2 FFSAT and the effect of FF thresholds on global FF and T2*

Next, we studied how lower and upper FF thresholds affected the cold-induced change in FF_{Glob} (ΔFF_{Glob} ; post-cooling minus pre-cooling) and FF_{SAT} (ΔFF_{SAT} ; post-cooling minus pre-cooling), as well as $T2^*_{Glob}$ ($\Delta T2^*_{Glob}$; post-cooling minus pre-cooling). The largest decrease in FF_{Glob} occurred at a lower FF threshold of 34% and upper FF threshold of 100% (Fig. S3). This decrease in FF became smaller when shifting the lower FF threshold towards higher values. This was further tested for statistical significance for the following FF ranges: 30-100%, 50-100% and 70-100%. When applying the 30-100% FF range, FF_{Glob} decreased from $62.0 \pm 1.6\%$ to $58.5 \pm 1.3\%$ (-3.5%; $p=5.0e-4$, Fig. 4A). With an intermediate threshold of 50-100%, FF_{Glob} decreased from $71.6 \pm 1.2\%$ to $68.4 \pm 1.0\%$ (-3.2%; $5.6e-4$, Fig. 4B). When a lower threshold of 70% was assumed, FF_{Glob} decreased from $81.0 \pm 0.7\%$ to $79.3 \pm 0.4\%$ (-1.6%; $p=0.006$, Fig. 4C). In contrast, no significant changes were noted in FF_{SAT} after cold exposure (Fig. S1B). For $T2^*_{Glob}$, no clear changes were seen as a function of different threshold options (Fig. S3;4D-F).

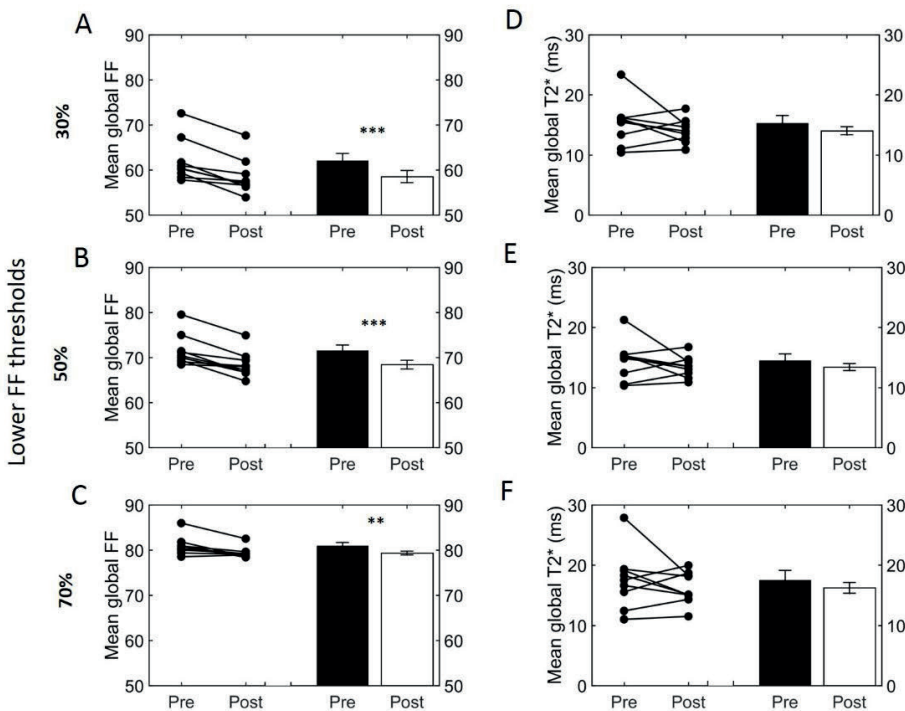


Figure 4. Effect of different FF thresholds on global supraclavicular adipose tissue FF and T2*

Cold-induced FF and T2* changes analyzed using the paired t-test at different threshold ranges: 30–100% (A,D), 50–100% (B,D) and 70–100% (C,F). Data are represented as mean \pm SEM for n=9.

The paired sample t-test was used to analyze the changes in volume after cold exposure (* $p<0.05$, ** $p<0.01$ and *** $p<0.001$).

4.3.3 Estimation of BAT lipid and lean mass after cold

Having defined the effect of cold exposure on Vol_{BAT} , FF_{Glob} and $\text{T2}^*_{\text{Glob}}$, we set out to characterize the subtle changes that take place within the tissue composition. Supraclavicular adipose tissue is composed of two compartments distinguishable by MRI: fat mass and lean mass. While fat mass comprises the accumulated lipid droplets, lean mass corresponds to water-rich structures, a broad category that includes blood, cytoplasm and hydrophilic structures, such as glycogen storages and proteins. Here we used the FF of each voxel to separate the underlying lean and fat masses (Fig. 5A, see “Methods” section for details). Interestingly, we observed a biphasic effect of cold exposure on supraclavicular adipose tissue mass (Fig. 5B). There was an apparent decrease in the number of voxels with a high FF, most pronouncedly observed as a decrease in lipid mass on the right side of the plot (i.e. 70–100% FF). Lean mass was also decreased in this range, albeit to a lesser extent. When the left side of the plot was taken into account (i.e. voxels included in the FF range below 70%), lean and fat masses were increased to a similar extent. Both lean mass and fat mass explained a large part of the variance of the total supraclavicular adipose volume, with slight dominance of lipid mass ($R^2 = 0.92$) over lean mass ($R^2 = 0.85$) (Fig. 5C). The discrepancy between loss and gain was quantified in the total mass variation of the tissue, where total lean mass was increased from 15.7 ± 1.6 g to 17.2 ± 1.7 g ($+1.5$ g; $p=0.001$) and total lipid mass in the supraclavicular depot decreased from 22.1 ± 1.9 g to 21.0 ± 1.7 g (-1.2 g; $p=0.02$) (Fig. 5D).

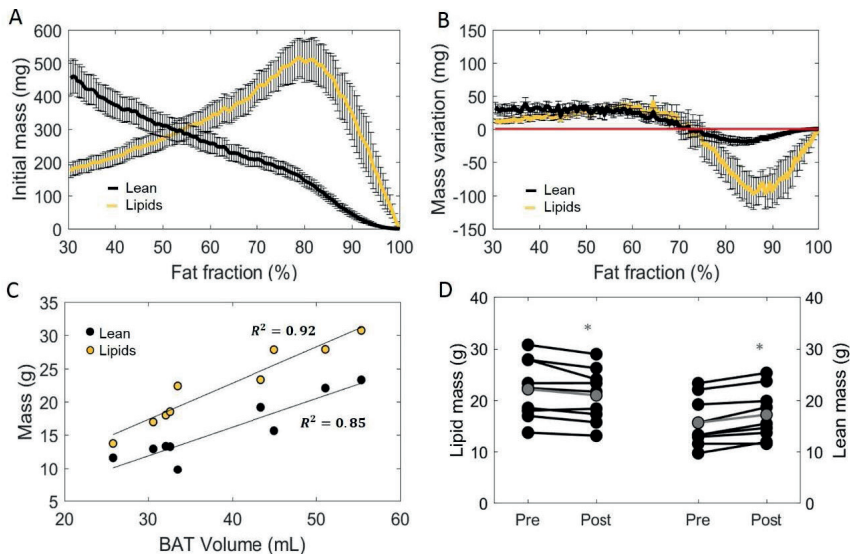


Figure 5. Distinction between lean and lipid masses within supraclavicular adipose tissue.

Lean and lipid masses were estimated as described in the “Methods” section and represented as a function of their specific fat fractions (A). Cold exposure decreased both lean and fat masses to in the upper fat fractions (above 70%) and slightly increased these in the lower fat fractions (B). (C) Correlation between total estimated BAT volume and lipid or lean mass analyzed using linear regression (R^2 is reported). Change in total lipid and lean mass after cold exposure, analyzed with the paired sample t-test(D). Data in A, B and D represent mean \pm SEM for $n = 9$ volunteers. * $p < 0.05$.

4.3.4 Tissue energy storages are decreased after cold exposure

The main function of BAT is to convert chemical energy into thermal energy. Estimation of metabolic energy content in lean and fat masses has been validated in well-controlled experiments measuring whole-body energy intake and expenditure³⁹, and the concept of energy equivalence has been used to quantify the energy influx to BAT during cold exposure⁴¹. In addition, because BAT does not contain significant amounts of bone mineral or air and the tissue water is bound to proteins, its total mass can be taken as the potential energy substrate for heat generation. Therefore, we set out to quantify the cold-induced change in energy storages.

BAT is composed of a mixture of lean and lipid masses, but its chemical energy storage equivalence is largely dominated by the lipid component (**Fig. 6A**). When analyzed from this bioenergetic perspective, the variation in lean mass previously observed by us (**Fig. 5B**) became insignificant, as cold-induced changes in energy content attributed to lean mass was substantially lower compared to energy variations in lipid mass (**Fig. 6B**). Here, the significant decrease in fat mass was reflected in a diminished energy storage in the supraclavicular depot, which decreased from 126 ± 11 kcal to 121 ± 10 kcal (-5 kcal; $p=0.03$, **Fig. 6C**). It was noticeable that this variation was not uniform in the volume histogram, but instead there were losses in the initial high-lipid area and gains in initially leaner parts of the tissue. To better visualize this effect, a contour plot was created to represent different thresholding possibilities for the analysis of energy variation (**Fig. 6D**). When the higher FFs of the tissue were chosen, a large decrease in energy content was inferred. On the other hand, an analysis focusing on the FF interval between 30% and 70%, for example, would have resulted in the opposite conclusion that the tissue increased its chemical energy storage after cold exposure.

4.3.5 Local assessment of the supraclavicular adipose tissue FF distribution after cold exposure

Voxel-wise thermoneutral and post-cooling FF maps unveiled that the supraclavicular adipose tissue is composed of a juxtaposition of low-and high lipid zones, as exemplified in **Figs. 7A,B**. After cold exposure, which is generally shown to decrease BAT lipid content, we found a high spatial variability in responses since several areas presented the expected reduction in lipids, while in contrast, other tissue areas increased their lipid content (**Fig. 7C**). Lipid maps of the other eight subjects are presented in **Fig. S4**.

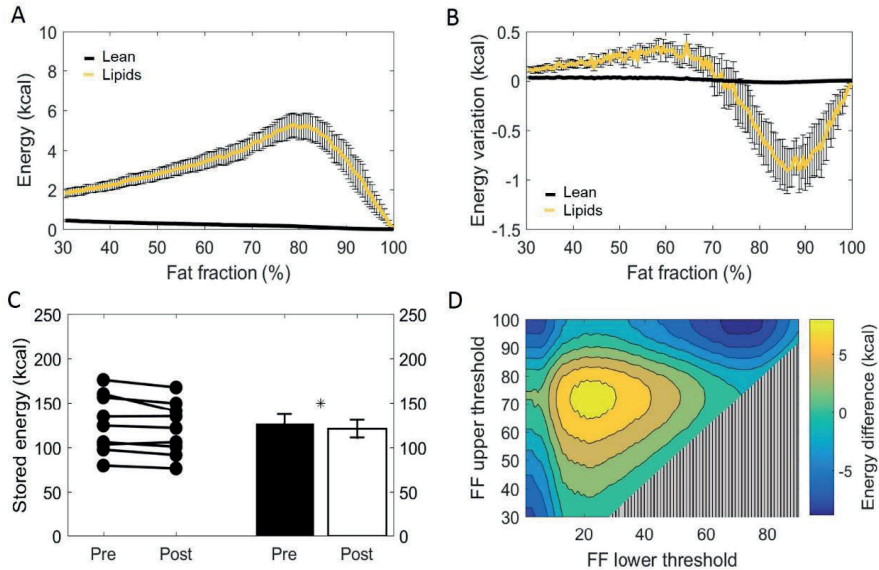


Figure 6. Metabolizable energy content in the supraclavicular adipose depot

Representation of energy content in the supraclavicular depot at thermoneutrality, with specific values attributed to lean tissue or lipids (A). Changes in energy content attributed to lean or fat masses, represented over different fat fraction ranges (B). Total energy storages (kcal) before and after cold exposure analyzed, by using the paired t-test (C). Heatmap of the effect of different FF segmentation thresholds on estimated energy content differences after cooling. The color (second y-axis) depicts the estimated energy content difference for each lower (x-axis) and upper left (y-axis) threshold. The largest decrease in estimated energy is present with a lower threshold of 70% and no upper threshold. The triangle in the lower right corner indicates invalid FF threshold options, as we implemented a minimum FF threshold of 30% (D). Data represent mean \pm SEM of all participants ($n=9$). * $p<0.05$.

Local FF changes were evaluated using a 2D joint histogram, where every voxel had its initial FF used as a reference to define the variation in FF that it underwent upon cold exposure, and the number of voxels belonging to each combination was added to represent the counts (color scale; **Fig. 7D**). Assuming the vertical line as zero change, we observed FF changes along the entire thermoneutral FF range, with a clear increase in voxel-density in the higher FF range. To quantify this, K-means clustering was applied with the optimal cluster number equal to four. The results are shown in Fig. S5. Cluster analysis indeed revealed that for the high thermoneutral FF range, FF decreases were observed especially within cluster C1 (average thermoneutral FF: $76.0 \pm 11.2\%$). The average FF decrease after cold-exposure that corresponded to this cluster was $-3.5 \pm 2.2\%$.

4.3.6 The association between supraclavicular adipose tissue FF and T2* on a local level

Using voxel-wise analysis, we then studied the relation of the baseline T2* relaxation time to tissue FF (**Fig. 8A**). T2*_{loc} values were near 10 ms at the lower FFs and circa 20–25 ms

at the highest FFs. However, there was no clear relation between the baseline FF_{Loc} and $T2^*_{Loc}$ values. Also, when the cold-induced changes in $T2^*_{Loc}$ were plotted against baseline FF_{Loc} , no clear association was observed (**Fig. 8B**). Regarding the changes in $T2^*_{Loc}$ and FF_{Loc} in response to cold exposure, for most voxels FF_{Loc} decreases were accompanied by increases in $T2^*_{Loc}$ (**Fig 8.C**). The voxel distribution was analyzed using k-means clustering. Cluster C1 included the highest voxel counts per data point (**Fig. S5**). For this cluster, the average $T2^*_{Loc}$ and FF_{Loc} changes were 1.4 ± 1.5 ms and $-2.2\% \pm 4.0\%$, respectively.

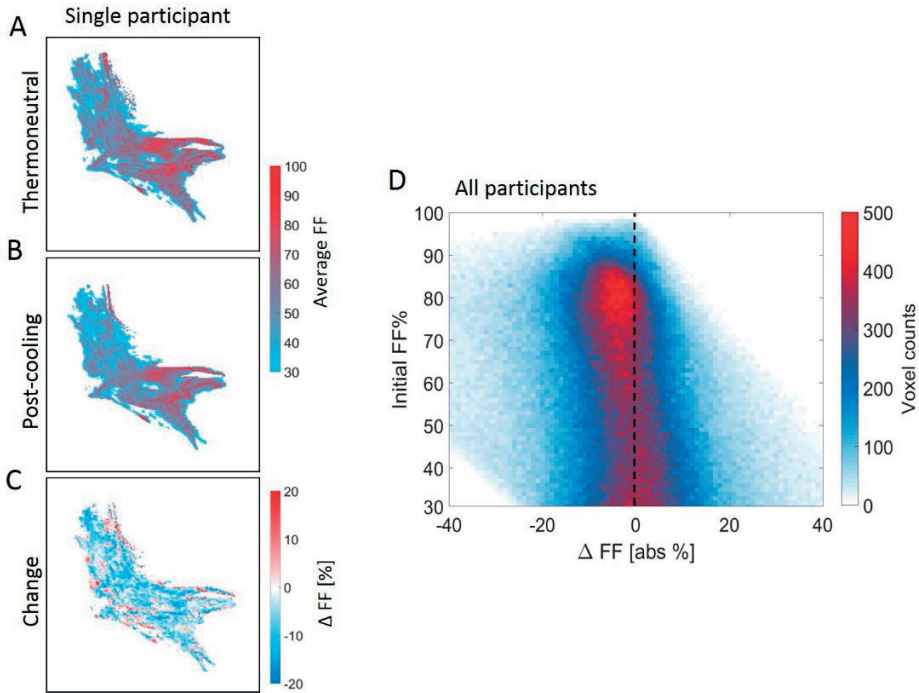


Figure 7. Structural heterogeneity of brown adipose tissue in the supraclavicular region during cold exposure
 Example of a reconstructed fat fraction map with merged z-slices before and after cooling (A,B) and cold-induced change (post minus pre) (C) for $n=1$. The 2D joint voxel histogram representing variation in change in lipid content of each voxel in relation to its thermoneutral FF from the voxel-wise analysis, wherein the colors represent the number of voxels belonging to each combination (D) for all participants ($n=9$). Cold colors indicate decreases in fat fraction and warm colors indicate increases in fat fraction.

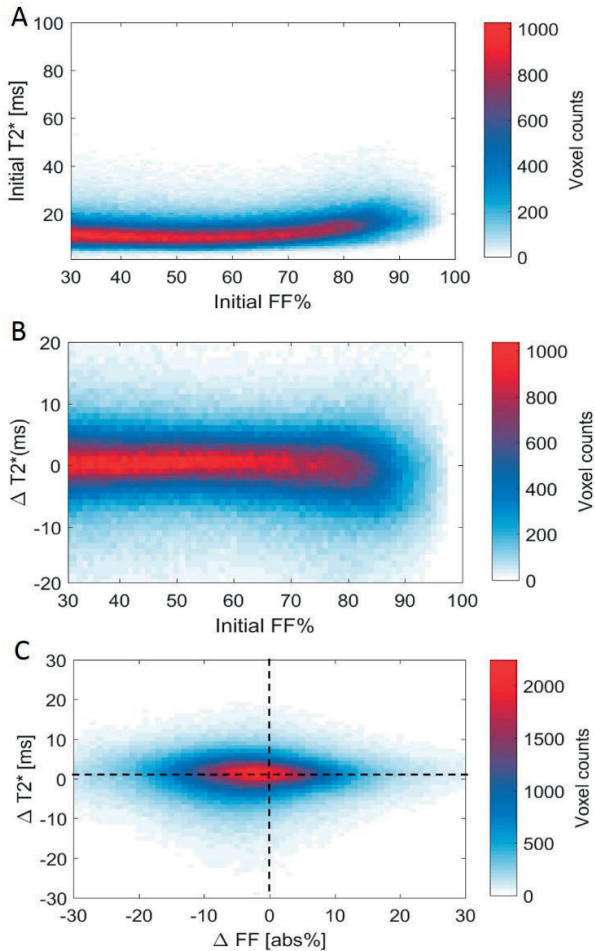


Figure 8. Voxel histograms representing the relation between thermoneutral values and cold-induced changes in T2* and FF

Thermoneutral measurements of T2* against thermoneutral fat fractions (A). Relation between the cold-induced changes in T2* and thermoneutral fat fractions (B). The association between cold-induced changes in both T2* and FF (C). Data is presented as the mean of all participants (n=9).

4.4 DISCUSSION

In this study, we show that reductions in volume, mass and energy of the supraclavicular adipose tissue depot during cold exposure are heterogeneous and take place most prominently within lipid-rich regions of the tissue, whereas no significant changes were observed in the SAT FF. Leaner areas of the supraclavicular adipose tissue depot (defined by a low thermoneutral FF), however, tended to gain volume, mass and energy following cold exposure. We also showed that the location and width of the FF interval can alter the apparent size and direction of cold-induced changes of MRI-derived parameters used for BAT analysis; The maximum FF change to the entire supraclavicular adipose depot was obtained by implementing a 34–100% FF range. Finally, local changes in FF occurred over the entire thermoneutral FF range (30–100%) in both directions (i.e., increase and decrease).

4.4.1 The upper FF threshold range for BAT FF analysis

The classical distinction between unilocular WAT and multilocular BAT suggests that a clear division based on FF should exist between both tissues. From this perspective, the range where FF is higher than 70% has previously been assumed to be above the BAT threshold⁵². For this reason, we found it remarkable that, in our results, these high-lipid areas of the supraclavicular adipose depot actually showed the largest decrease in lipid and energy content after cold exposure, which is in agreement with recent findings²⁵. These data suggest that, in fact, one should not use 70% as an upper threshold, and voxels showing up to 100% FF should be used in the analysis (e.g. as performed in^{22,53}). Unfortunately, it was not possible to infer whether these regions comprised unilocular white adipocytes that partially donated their lipids for combustion by surrounding “leaner” brown adipocytes. Alternatively, this region could englobe unilocular UCP1-expressing cells capable of thermogenesis. In both scenarios, the lobular distribution of high-fat zones, intercalated by regions of lower lipid content, suggests that human BAT should be taken as a morphologically diverse organ, and care should be used before excluding areas from its analysis. T2* analysis did not provide any additional information in establishing lower and upper FF thresholds for BAT segmentation.

4.4.2 The lower FF threshold range for BAT analyses of FF and volume

Both the global and local analyses showed that changes occurred across the entire baseline FF range (30–100%), with the greatest apparent FF decrease when using a 34–100% FF range. The largest FF decrease we observed (i.e. 3.5%) is in the range of values reported in literature^{19,21,23}, but also much smaller²² and larger decreases²⁵ have been reported. This could be due to the use of different thresholds, but also differences in the cooling protocols can play an important role^{54,55}. Raising the lower threshold above 34% decreases the extent of FF differences upon cold exposure, as we excluded voxels that fell

below the threshold in both the thermoneutral and post-cooling scan in order to avoid partial volume artifacts and to enable volumetric analysis. For example, when a lower FF threshold of 70% is used, voxels below 70% FF are excluded in both the thermoneutral and post-cooling ROIs. Hence, regions in the post-cooling ROIs that shifted from high thermoneutral FFs (>70%) to FFs below 70% upon cold exposure are excluded, but are still present in the thermoneutral ROIs. These lower FF regions can, therefore, not contribute to the reduction of FF_{Glob} in the post-cooling ROIs. A recent report where the use of FF thresholds were also explored showed an opposite effect, as a larger effect on FF was shown using a 50% threshold compared to a 40% threshold. In their approach, FF thresholds were only applied to the thermoneutral ROIs²⁵, which could have enabled measuring larger FF differences with increasing lower thresholds because voxels in the post-cooling scans were not excluded. This indicates that care should be taken before excluding low-lipid areas from the analysis. The total estimated BAT volume showed an opposite trend compared to FF, where increasing the lower FF threshold enlarged the differences. This is expected, as most prominent volume reductions take place above a FF of about 70%.

4.4.3 On the heterogeneity of human supraclavicular adipose tissue

In this work, we expanded the idea of supraclavicular adipose tissue heterogeneity by visualizing its structure, its complex distribution of lipids and described the variations in the lipid content (increased and decreased in the same depot) after cold exposure. These data strongly suggest that BAT acutely modulates lipid influx and combustion divergently, here exemplified by the supraclavicular areas that gained lipids after thermogenic activation by cold exposure, which was also shown in a recent study²⁵. This example goes against expectations of BAT only decreasing its lipid content, an idea so broadly accepted that the loss of lipids during cooling has been used as a condition sine qua non for the identification of BAT²³. The guiding factors behind the cold-induced lipid gain in some BAT areas are unclear. We speculate that an increase in lipids is also possible due to de novo lipogenesis taking place after glucose uptake⁵⁶.

4.4.4 Mass quantification within the supraclavicular adipose depot

In the present work, we estimated the absolute amounts of lean and fat masses within the supraclavicular adipose depot. This provided the insight that, at least in our lean young subjects, fat and lean masses (conceptualized as representing the lipid storages and the metabolically-active components of the tissue, respectively) had a high linear correlation with total tissue volume. Therefore, we assume that estimated BAT size in its simplest measure is likely to be correlated to its total potential thermogenic function.

The cold-induced decrease in total lipid mass seen in our study was expected because of the thermogenic activation of BAT, which leads to increased β -oxidation^{57,58}, and is in agreement with other imaging studies using FF as an outcome^{19,21,25,59}. This was ac-

accompanied by an increase in lean mass, which is unlikely to be caused by acute protein synthesis, since our entire experiment took place in a few hours. The increase in blood perfusion expected to happen in BAT during cold exposure^{2,22,60-63} could contribute to an increase in water signal. However, it was recently postulated that FF reductions immediately after cold-exposure are too large to be solely achieved by increasing the blood volume fraction²⁵. Additionally, cold-induced FF decreases were shown to be maintained even after reheating the subject, which does not coincide with the fast dynamics of perfusion^{19,25}. These findings support the rationale that the observed decrease in lipid mass and increase in lean mass are prominently caused by the intracellular lipid depletion in brown adipocytes. This results from the very general classification of lean mass as a collection of structures richly bound to water, which makes it susceptible to acute changes in hydration levels⁶⁴.

In a broader context of metabolic studies, lean mass is generally understood to be the major determinant of whole-body basal metabolic rate. Because the contribution of specific organs to the whole-body basal metabolic rate can be estimated based on their total mass⁶⁵⁻⁶⁷, we predict that the evaluation of the specific lean mass of organs (such as performed in our study) may contribute to the generation of better allometric models to infer on organ-specific metabolic rates and their influence on whole-body energy expenditure.

4.4.5 Energy variation following thermogenic activation

The supraclavicular adipose tissue composition analysis demonstrated the dominance of fat mass on energy dynamics during cold exposure. Critically, although lean mass comprised almost half of the tissue, even significant variations in its mass are not likely to play a major role in metabolic energy storage. We can only speculate on whether this reflects a decreased volume of larger lipid droplets due to combustion, increased lipid droplet formation due to lipid uptake from the bloodstream, or a combination of both phenomena. Based on the principle of energy conservation, it can be postulated that, if the nutrient uptake by the tissue perfectly matches its combustion rates, the fat energy loss and gain within different FF of the organ will be equal to zero. Results differing from zero can be interpreted as an uncompensated or overcompensated lipid (or glucose) uptake from the bloodstream (in relation to BAT expenditure during cooling). Most importantly, while our setup did not allow us to estimate the total energy flux of the tissue, it did provide an important conceptual milestone for the quantification of BAT-specific energy expenditure. Because expenditure can be estimated based on combinatory measurements of glucose and lipid uptake and variations in tissue composition, we predict that the method employed in our study (allied to energy uptake estimations by Virtanen et al.⁴¹) will make it possible to finally infer concerning the energy combusted by BAT during activation and to more accurately quantify the specific contribution of BAT depots to whole-body metabolism.

4.4.6 General conceptual applications of the method

The application of the bioenergetic framework presented here is not confined to the analysis of BAT during cooling. It can also be used for the analysis of metabolic content in any tissue where energy storages are crucial for pathophysiological processes. These include muscles, where changes in energy availability can modify the long-term maintenance of the mass, as well as the liver, where excessive energy storages in the form of lipid droplets are thought to be causal to insulin resistance and metabolic diseases.

4.4.7 Limitations

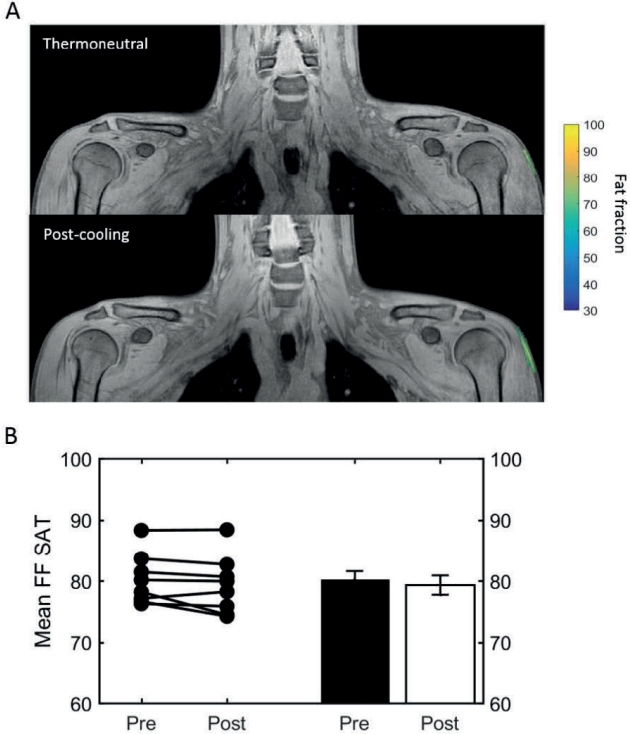
We could only partially infer about the dynamic changes in tissue composition due to the limited number of time-points, i.e., one before and after cooling. Dynamic scans would possibly provide more insights into changes in lipid composition within the supraclavicular adipose depot. In our study, we used six echoes for the mono-exponential T2* fit. Recently, a study has shown that the accuracy of the fit enhances with increasing echo number²⁶, and therefore in future studies the echo number will be increased to improve T2* measurement in BAT. We did not perform respiratory triggering in acquisition, which could have led to motion artefacts. We mitigated this by using a 3x3 smoothing kernel after registration. In addition, a recent study that employed similar MR methodology without respiratory triggering demonstrated an error of less than one pixel after image registration²⁵.

This study included a relatively homogeneous study population (young, male, healthy, lean white Dutch natives). Therefore, caution should be used when extrapolating our results to a more general population. Instead, it is recommended to assume our results as representing those of a control population and as a demonstration of methodological possibilities to track alterations in obesity, disease or drug testing. The extent of cold-induced FF changes that have been reported in literature and in this study, are quite modest. It has been also shown that there is only a small, albeit statistically difference in supraclavicular FF between individuals with and without BAT activity on [¹⁸F]FDG PET-CT⁶⁸. BAT activity assessed by glucose uptake in PET-CT and by FF differences upon cold exposure, however, are not measuring the same exact response. This is not unexpected, as in [¹⁸F]FDG PET glucose is used as a tracer, while in fat-water MRI we are assessing the fat content directly. Future studies including multiple MR sequences each tuned to a different aspect of physiology will hopefully further elucidate this issue.

In conclusion, the supraclavicular adipose depot in humans is highly heterogeneous with respect to basal lipid content, and lipid-rich areas are intercalated with lipid-poor regions. After thermogenic activation by cooling, areas of the tissue with a high FF tend to lose more lipids, while an increase in mass is noticeable in the leaner regions. Cold-induced loss of metabolic energy is more noticeable in the high 70-100% FF range. Overall, cold

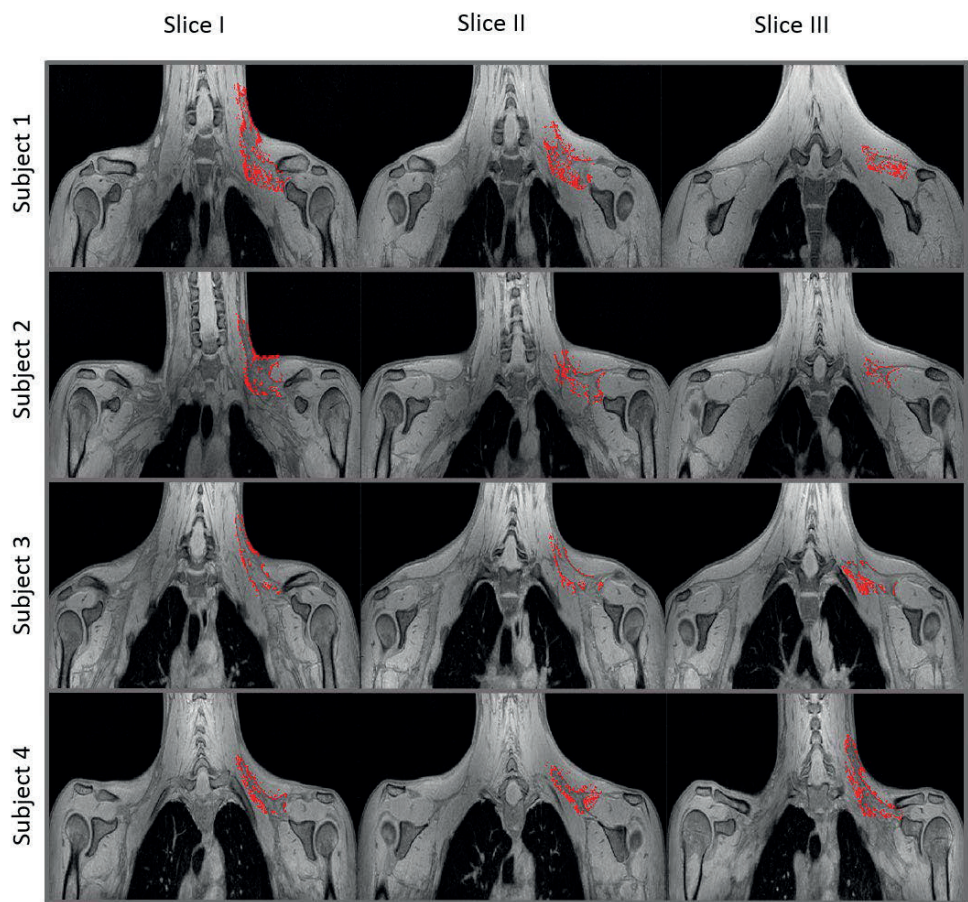
exposure decreases absolute lipid mass and tissue energy content, which is associated with an increase in lean mass, but does not significantly change tissue volume. Due to variability of the supraclavicular adipose depot when responding to cold exposure, the choice of MRI thresholding highly affects the estimated magnitude and direction of changes. Overall, we found that by increasing the lower FF threshold level, global FF differences became less pronounced, whereas estimated BAT volume differences became larger in magnitude. This emphasizes that the selection of FF threshold levels can affect parameters differently.

SUPPLEMENTAL DATA

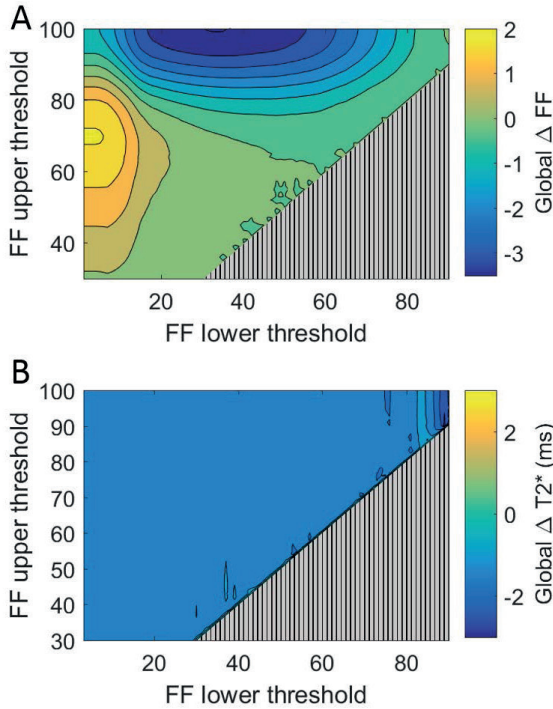


Supplemental Figure S1. Deltoid SAT ROI delineation and SAT FF (FFSAT) analysis

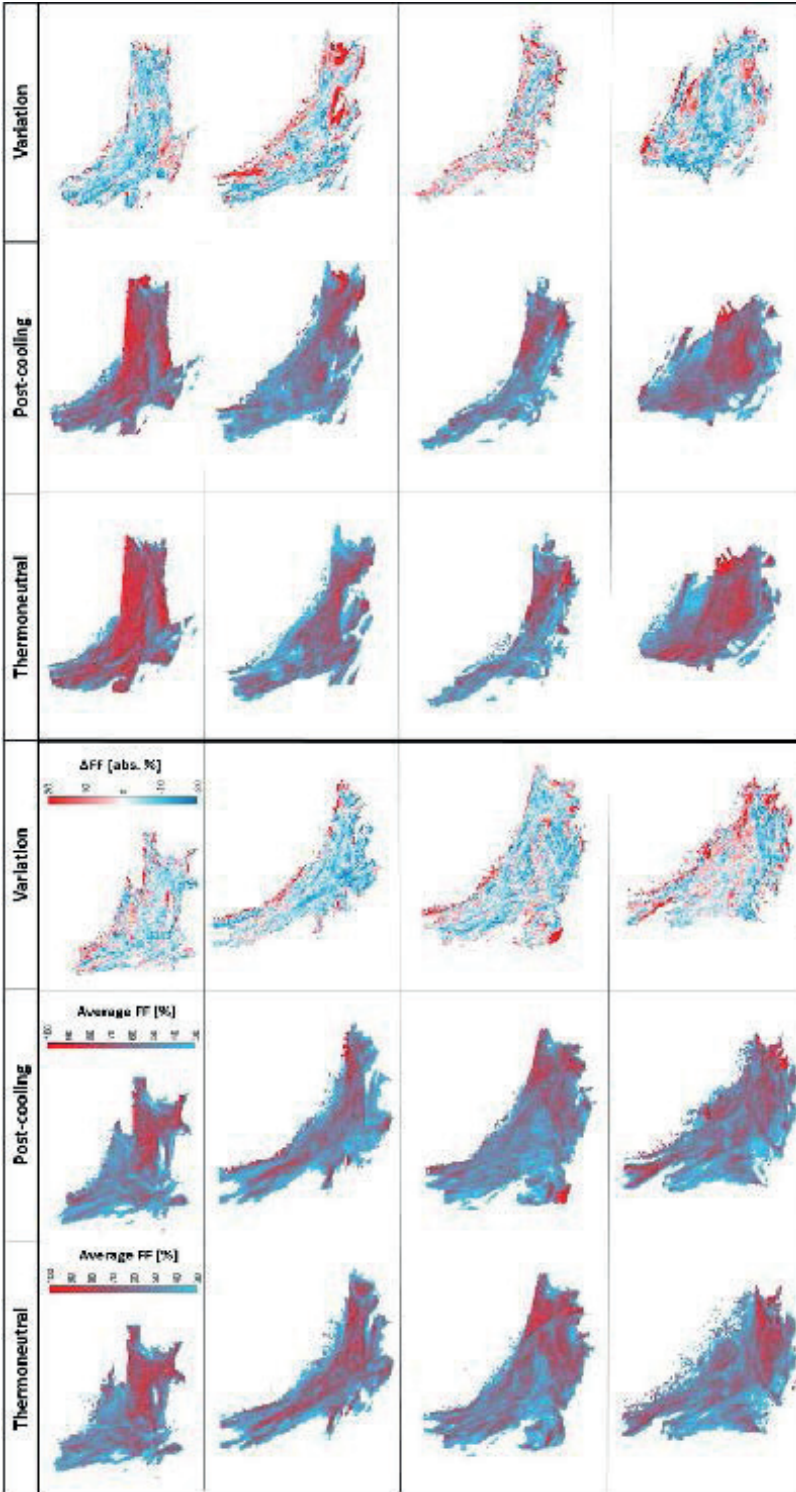
The SAT ROI in the thermoneutral scan (top) and post-cooling scan (bottom) (A). Lipid content in the SAT region is color-mapped over a 30–100% FF range. SAT FF before and after cooling (B). Data are represented as mean±SEM for n=8. Data analysis was performed using the paired t-test.



Supplemental Figure S2. Localization of low FF voxels (10–30%) in the supraclavicular adipose depot
 Voxels within the 10–30% FF range are shown for a selection of the group (n=4). For each participant three slices, ordered in the anterior-posterior direction, are presented. Only voxels above 10% are shown to emphasize the boundaries of the supraclavicular depot.

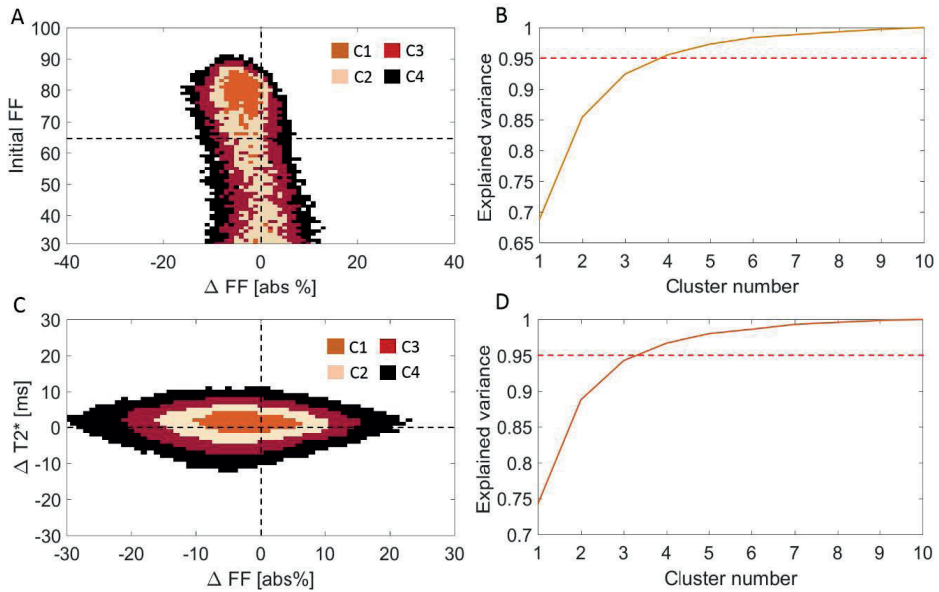


Supplemental Figure S3. Effects of different FF thresholding options on cold-induced global FF and T2* changes
 Heatmap of the effect of different FF segmentation thresholds on FF and T2* changes after cooling. (A) The color (second y-axis) depicts the FF change for each lower (x-axis) and upper left (y-axis) FF segmentation threshold. The largest FF decrease is present with a lower threshold of 34% and no upper threshold. (B) The color (second y-axis) depicts the T2* change for each lower (x-axis) and upper left (y-axis) FF segmentation threshold. The largest T2* decrease is present with a lower threshold of 90% and no upper threshold, however this was not found to be significant. The triangle in the lower right corner indicates invalid FF threshold options, as we implemented a minimum FF threshold of 30%. Data represent the mean of n=9 subjects.



Supplemental Figure 4. Fat fraction maps of the supraclavicular adipose depot with merged z-slices

Average FF value of voxels containing the same (x, y) position was extracted to construct the FF and FF variation maps. Voxels below 30% FF were thresholded in order to avoid inclusion of non-fatty tissue and to minimize partial volume interference. For thermoneutral and post-cooling FF maps, the red color indicates high lipid regions and the blue color — low-lipid regions. Cold-induced changes are represented by the red color for increased lipid content and the blue color for decreased lipid content.



Supplemental Figure S5. K-means cluster analysis for local assessment of supraclavicular adipose tissue baseline FF_{loc} and cold-induced FF_{loc} and $T2^*_{loc}$ changes

The joint voxel distribution from Fig. 7D partitioned into four clusters (A). The optimal number of clusters was obtained by visual inspection of the explained variance plot (cut-off 95%): it was noted that the rise in explained variance became increasingly less after the fourth cluster (B). Clustered joint voxel distribution from Fig. 8C (C). Also for this analysis four clusters were used, based on the explained variance plot shown in (D). Data represent the mean of $n = 9$ subjects.

REFERENCES

1. Cannon B, Nedergaard J. Brown Adipose Tissue: Function and Physiological Significance. *Physiol Rev.* 2004;84(1):277-359. doi:10.1152/physrev.00015.2003
2. Blondin DP, Frisch F, Phoenix S, et al. Inhibition of Intracellular Triglyceride Lipolysis Suppresses Cold-Induced Brown Adipose Tissue Metabolism and Increases Shivering in Humans. *Cell Metab.* 2017;25(2):438-447. doi:10.1016/j.cmet.2016.12.005
3. Bartelt A, Bruns OT, Reimer R, et al. Brown adipose tissue activity controls triglyceride clearance. *Nat Med.* 2011;17(2):200-206. doi:10.1038/nm.2297
4. Olsen JM, Csikasz RI, Dehvari N, et al. β 3-Adrenergically induced glucose uptake in brown adipose tissue is independent of UCP1 presence or activity: Mediation through the mTOR pathway. *Mol Metab.* 2017;6(6):611-619. doi:10.1016/j.molmet.2017.02.006
5. Osculati F, Leclercq F, Sbarbati A, Zancanaro C, Cinti S, Antonakis K. Morphological identification of brown adipose tissue by magnetic resonance imaging in the rat. *Eur J Radiol.* 1989;9(2):112-114. <http://www.ncbi.nlm.nih.gov/pubmed/2743984>.
6. Osculati F, Sbarbati A, Leclercq F, et al. The correlation between magnetic resonance imaging and ultrastructural patterns of brown adipose tissue. *J Submicrosc Cytol Pathol.* 1991;23(1):167-174. <http://www.ncbi.nlm.nih.gov/pubmed/2036625>.
7. Sbarbati A, Baldassarri AM, Zancanaro C, Boicelli A, Osculati F. In vivo morphometry and functional morphology of brown adipose tissue by magnetic resonance imaging. *Anat Rec.* 1991;231(3):293-297. doi:10.1002/ar.1092310302
8. Hu HH. Magnetic resonance of brown adipose tissue: A review of current techniques. *Crit Rev Biomed Eng.* 2015;43(2-3):161-181. doi:10.1615/CritRevBiomedEng.2015014377
9. Hu HH, Li Y, Nagy TR, Goran MI, Nayak KS. Quantification of Absolute Fat Mass by Magnetic Resonance Imaging: a Validation Study against Chemical Analysis. *Int J Body Compos Res.* 2011;9(3):111-122. <http://www.ncbi.nlm.nih.gov/pubmed/23204926><http://www.pubmedcentral.nih.gov/articlerender.fcgi?artid=PMC3509746>.
10. Branca RT, Zhang L, Warren WS, et al. In Vivo Noninvasive Detection of Brown Adipose Tissue through Intermolecular Zero-Quantum MRI. *PLoS One.* 2013;8(9). doi:10.1371/journal.pone.0074206
11. Peng XG, Ju S, Fang F, et al. Comparison of brown and white adipose tissue fat fractions in ob, seipin, and Fsp27 gene knockout mice by chemical shift-selective imaging and ¹H-MR spectroscopy. *Am J Physiol - Endocrinol Metab.* 2013;304(2). doi:10.1152/ajpendo.00401.2012
12. Lunati E, Marzola P, Nicolato E, Fedrigo M, Villa M, Sbarbati A. In vivo quantitative lipidic map of brown adipose tissue by chemical shift imaging at 4.7 tesla. *J Lipid Res.* 1999;40(8):1395-1400. <http://www.ncbi.nlm.nih.gov/pubmed/10428975>.
13. Smith DL, Yang Y, Hu HH, Zhai G, Nagy TR. Measurement of interscapular brown adipose tissue of mice in differentially housed temperatures by chemical-shift-encoded water-fat MRI. *J Magn Reson Imaging.* 2013;38(6):1425-1433. doi:10.1002/jmri.24138
14. Lidell ME, Betz MJ, Leinhard OD, et al. Evidence for two types of brown adipose tissue in humans. *Nat Med.* 2013;19(5):631-634. doi:10.1038/nm.3017
15. Chen KY, Cypess AM, Laughlin MR, et al. Brown Adipose Reporting Criteria in Imaging Studies (BARCIST 1.0): Recommendations for Standardized FDG-PET/CT Experiments in Humans. *Cell Metab.* 2016;24(2):210-222. doi:10.1016/j.cmet.2016.07.014
16. Gifford A, Towse TF, Walker RC, Avison MJ, Welch EB. Characterizing active and inactive brown adipose tissue in adult humans using PET-CT and MR imaging. *Am J Physiol - Endocrinol Metab.* 2016;311(1):E95-E104. doi:10.1152/ajpendo.00482.2015

17. Van Rooijen BD, Van Der Lans AAJJ, Brans B, et al. Imaging cold-activated brown adipose tissue using dynamic T2*-Weighted magnetic resonance imaging and 2-deoxy-2-[18F]fluoro-d-glucose positron emission tomography. *Invest Radiol.* 2013;48(10):708-714. doi:10.1097/RLI.0b013e31829363b8
18. Franssens BT, Hoogduin H, Leiner T, van der Graaf Y, Visseren FLJ. Relation between brown adipose tissue and measures of obesity and metabolic dysfunction in patients with cardiovascular disease. *J Magn Reson Imaging.* 2017;46(2):497-504. doi:10.1002/jmri.25594
19. Lundström E, Strand R, Johansson L, Bergsten P, Ahlström H, Kullberg J. Magnetic resonance imaging cooling-reheating protocol indicates decreased fat fraction via lipid consumption in suspected brown adipose tissue. *PLoS One.* 2015;10(4). doi:10.1371/journal.pone.0126705
20. Franz D, Karampinos DC, Rummeny EJ, et al. Discrimination between brown and white adipose tissue using a 2-point dixon water-fat separation method in simultaneous pet/MRI. *J Nucl Med.* 2015;56(11):1742-1747. doi:10.2967/jnumed.115.160770
21. Deng J, Neff LM, Rubert NC, et al. MRI characterization of brown adipose tissue under thermal challenges in normal weight, overweight, and obese young men. *J Magn Reson Imaging.* 2018;47(4):936-947. doi:10.1002/jmri.25836
22. Holstila M, Pesola M, Saari T, et al. MR signal-fat-fraction analysis and T2* weighted imaging measure BAT reliably on humans without cold exposure. *Metabolism.* 2017;70:23-30. doi:10.1016/j.metabol.2017.02.001
23. Stahl V, Maier F, Freitag MT, et al. In vivo assessment of cold stimulation effects on the fat fraction of brown adipose tissue using DIXON MRI. *J Magn Reson Imaging.* 2017;45(2):369-380. doi:10.1002/jmri.25364
24. Gashi G, Madoerin P, Maushart CI, et al. MRI characteristics of supraclavicular brown adipose tissue in relation to cold-induced thermogenesis in healthy human adults. *J Magn Reson Imaging.* 2019;50(4):1160-1168. doi:10.1002/jmri.26733
25. Coolbaugh CL, Damon BM, Bush EC, Welch EB, Towse TF. Cold exposure induces dynamic, heterogeneous alterations in human brown adipose tissue lipid content. *Sci Rep.* 2019;9(1):13600. doi:10.1038/s41598-019-49936-x
26. Franz D, Diefenbach MN, Treibel F, et al. Differentiating supraclavicular from gluteal adipose tissue based on simultaneous PDFF and T2* mapping using a 20-echo gradient-echo acquisition. *Journal of Magnetic Resonance Imaging.* 2019:424-434. doi: 10.1002/jmri.26661
27. Hui SCN, Ko JKL, Zhang T, et al. Quantification of brown and white adipose tissue based on Gaussian mixture model using water-fat and T2* MRI in adolescents. *J Magn Reson Imaging.* 2017;46(3):758-768. doi:10.1002/jmri.25632
28. Khanna A, Branca RT. Detecting brown adipose tissue activity with BOLD MRI in mice. *Magn Reson Med.* 2012;68(4):1285-1290. doi:10.1002/mrm.24118
29. Chen YCI, Cypess AM, Chen YC, et al. Measurement of human brown adipose tissue volume and activity using anatomic MR imaging and functional MR imaging. *J Nucl Med.* 2013;54(9):1584-1587. doi:10.2967/jnumed.112.117275
30. Van Rooijen BD, Van Der Lans AAJJ, Brans B, et al. Imaging cold-activated brown adipose tissue using dynamic T2*-Weighted magnetic resonance imaging and 2-deoxy-2-[18F]fluoro-d-glucose positron emission tomography. *Invest Radiol.* 2013;48(10):708-714. doi:10.1097/RLI.0b013e31829363b8
31. Cinti S, Cancellato R, Zingaretti MC, et al. CL316,243 and cold stress induce heterogeneous expression of UCP1 mRNA and protein in rodent brown adipocytes. *J Histochem Cytochem.* 2002;50(1):21-31. doi:10.1177/002215540205000103

32. de Jong JMA, Larsson O, Cannon B, Nedergaard J. A stringent validation of mouse adipose tissue identity markers. *Am J Physiol - Endocrinol Metab.* 2015;308(12):E1085-E1105. doi:10.1152/ajpendo.00023.2015
33. Jeffery E, Wing A, Holtrup B, et al. The Adipose Tissue Microenvironment Regulates Depot-Specific Adipogenesis in Obesity. *Cell Metab.* 2016;24(1):142-150. doi:10.1016/j.cmet.2016.05.012
34. Grandl G, Müller S, Moest H, Moser C, Wollscheid B, Wolfrum C. Depot specific differences in the adipogenic potential of precursors are mediated by collagenous extracellular matrix and Flotillin 2 dependent signaling. *Mol Metab.* 2016;5(10):937-947. doi:10.1016/j.molmet.2016.07.008
35. Branca RT, He T, Zhang L, et al. Detection of brown adipose tissue and thermogenic activity in mice by hyperpolarized xenon MRI. *Proc Natl Acad Sci U S A.* 2014;111(50):18001-18006. doi:10.1073/pnas.1403697111
36. Bhanu Prakash KN, Verma SK, Yaligar J, et al. Segmentation and characterization of interscapular brown adipose tissue in rats by multi-parametric magnetic resonance imaging. *Magn Reson Mater Physics, Biol Med.* 2016;29(2):277-286. doi:10.1007/s10334-015-0514-3
37. Hu HH, Smith DL, Nayak KS, Goran MI, Nagy TR. Identification of brown adipose tissue in mice with fat-water IDEAL-MRI. *J Magn Reson Imaging.* 2010;31(5):1195-1202. doi:10.1002/jmri.22162
38. Hu HH, Wu TW, Yin L, et al. MRI detection of brown adipose tissue with low fat content in newborns with hypothermia. *Magn Reson Imaging.* 2014;32(2):107-117. doi:10.1016/j.mri.2013.10.003
39. Ravussin Y, Gutman R, Leduc CA, Leibel RL. Estimating energy expenditure in mice using an energy balance technique. *Int J Obes.* 2013;37(3):399-403. doi:10.1038/ijo.2012.105
40. Heymsfield SB, Peterson CM, Thomas DM, et al. Establishing energy requirements for body weight maintenance: Validation of an intake-balance method NCT01672632 NCT. *BMC Res Notes.* 2017;10(1). doi:10.1186/s13104-017-2546-4
41. u Din M, Raiko J, Saari T, et al. Human brown adipose tissue [15O]O₂ PET imaging in the presence and absence of cold stimulus. *Eur J Nucl Med Mol Imaging.* 2016;43(10):1878-1886. doi:10.1007/s00259-016-3364-y
42. Bakker LEH, Boon MR, van der Linden RAD, et al. Brown adipose tissue volume in healthy lean south Asian adults compared with white Caucasians: A prospective, case-controlled observational study. *Lancet Diabetes Endocrinol.* 2014;2(3):210-217. doi:10.1016/S2213-8587(13)70156-6
43. Yu H, Reeder SB, Shimakawa A, Brittain JH, Pelc NJ. Field map estimation with a region growing scheme for iterative 3-point water-fat decomposition. *Magn Reson Med.* 2005;54(4):1032-1039. doi:10.1002/mrm.20654
44. Reeder SB, Wen Z, Yu H, et al. Multicoil Dixon Chemical Species Separation with an Iterative Least-Squares Estimation Method. *Magn Reson Med.* 2004;51(1):35-45. doi:10.1002/mrm.10675
45. Yu H, McKenzie CA, Shimakawa A, et al. Multiecho reconstruction for simultaneous water-fat decomposition and T₂* estimation. *J Magn Reson Imaging.* 2007;26(4):1153-1161. doi:10.1002/jmri.21090
46. Reeder SB, Pineda AR, Wen Z, et al. Iterative decomposition of water and fat with echo asymmetry and least-squares estimation (IDEAL): Application with fast spin-echo imaging. *Magn Reson Med.* 2005;54(3):636-644. doi:10.1002/mrm.20624

47. Klein S, Staring M, Murphy K, Viergever MA, Pluim JPW. Elastix: A toolbox for intensity-based medical image registration. *IEEE Trans Med Imaging*. 2010;29(1):196-205. doi:10.1109/TMI.2009.2035616
48. Shamonin DP, Bron EE, Lelieveldt BPF, Smits M, Klein S, Staring M. Fast parallel image registration on CPU and GPU for diagnostic classification of Alzheimer's disease. *Front Neuroinform*. 2014;7(JAN):50. doi:10.3389/fninf.2013.00050
49. Sacks H, Symonds ME. Anatomical locations of human brown adipose tissue: Functional relevance and implications in obesity and type 2 diabetes. *Diabetes*. 2013;62(6):1783-1790. doi:10.2337/db12-1430
50. Martinez-Tellez B, Nahon KJ, Sanchez-Delgado G, et al. The impact of using BARCIST 1.0 criteria on quantification of BAT volume and activity in three independent cohorts of adults. *Sci Rep*. 2018;8(1). doi:10.1038/s41598-018-26878-4
51. Madhulatha TS. An Overview on Clustering Methods. *IOSR J Eng*. 2012;2(4):719-725. <http://arxiv.org/abs/1205.1117>.
52. Hu HH, Perkins TG, Chia JM, Gilsanz V. Characterization of human brown adipose tissue by chemical-shift water-fat MRI. *Am J Roentgenol*. 2013;200(1):177-183. doi:10.2214/AJR.12.8996
53. McCallister A, Zhang L, Burant A, Katz L, Branca RT. A pilot study on the correlation between fat fraction values and glucose uptake values in supraclavicular fat by simultaneous PET/MRI. *Magn Reson Med*. 2017;78(5):1922-1932. doi:10.1002/mrm.26589
54. Sun L, Verma S, Michael N, et al. Brown Adipose Tissue: Multimodality Evaluation by PET, MRI, Infrared Thermography, and Whole-Body Calorimetry (TACTICAL-II). *Obesity*. 2019;27(9):1434-1442. doi:10.1002/oby.22560
55. Ong FJ, Ahmed BA, Oreskovich SM, et al. Recent advances in the detection of brown adipose tissue in adult humans: A review. *Clin Sci*. 2018;132(10):1039-1054. doi:10.1042/CS20170276
56. Irshad Z, Dimitri F, Christian M, Zammit VA. Diacylglycerol acyltransferase 2 links glucose utilization to fatty acid oxidation in the brown adipocytes. *J Lipid Res*. 2017;58(1):15-30. doi:10.1194/jlr.M068197
57. Xing Xian YU, Lewin DA, Forrest W, Adams SH. Cold elicits the simultaneous induction of fatty acid synthesis and β -oxidation in murine brown adipose tissue: Prediction from differential gene expression and confirmation in vivo. *FASEB J*. 2002;16(2):155-168. doi:10.1096/fj.01-0568com
58. Blondin DP, Labbé SM, Tingelstad HC, et al. Increased brown adipose tissue oxidative capacity in cold-acclimated humans. *J Clin Endocrinol Metab*. 2014;99(3):E438-46. doi:10.1210/jc.2013-3901
59. Koskensalo K, Raiko J, Saari T, et al. Human brown adipose tissue temperature and fat fraction are related to its metabolic activity. *J Clin Endocrinol Metab*. 2017;102(4):1200-1207. doi:10.1210/jc.2016-3086
60. Abreu-Vieira G, Hagberg CE, Spalding KL, Cannon B, Nedergaard J. Adrenergically stimulated blood flow in brown adipose tissue is not dependent on thermogenesis. *Am J Physiol - Endocrinol Metab*. 2015;308(9):E822-E829. doi:10.1152/ajpendo.00494.2014
61. Muzik O, Mangner TJ, Leonard WR, Kumar A, Granneman JG. Sympathetic Innervation of Cold-Activated Brown and White Fat in Lean Young Adults. *J Nucl Med*. 2017;58(5):799-806. doi:10.2967/jnumed.116.180992
62. Muzik O, Mangner TJ, Leonard WR, Kumar A, Janisse J, Granneman JG. 150 PET measurement of blood flow and oxygen consumption in cold-activated human brown fat. *J Nucl Med*. 2013;54(4):523-531. doi:10.2967/jnumed.112.111336

63. Orava J, Nuutila P, Lidell ME, et al. Different metabolic responses of human brown adipose tissue to activation by cold and insulin. *Cell Metab.* 2011;14(2):272-279. doi:10.1016/j.cmet.2011.06.012
64. Thomsen TK, Jensen VJ, Henriksen MG. In vivo measurement of human body composition by dual-energy X-ray absorptiometry (DXA). *Eur J Surg.* 1998;164(2):133-137. doi:10.1080/110241598750004797
65. Wang Z, Ying Z, Bosy-Westphal A, et al. Specific metabolic rates of major organs and tissues across adulthood: evaluation by mechanistic model of resting energy expenditure. *Am J Clin Nutr.* 2010;92(6):1369-1377. doi:10.3945/ajcn.2010.29885
66. Kaiyala KJ. Mathematical model for the contribution of individual organs to non-zero γ -intercepts in single and multi-compartment linear models of whole-body energy expenditure. *PLoS One.* 2014;9(7). doi:10.1371/journal.pone.0103301
67. Gallagher D, Belmonte D, Deurenberg P, et al. Organ-tissue mass measurement allows modeling of free and metabolically active tissue mass. *Am J Physiol - Endocrinol Metab.* 1998;275(238-2). doi:10.1152/ajpendo.1998.275.2.e249
68. Jones TA, Wayte SC, Reddy NL, et al. Identification of an optimal threshold for detecting human brown adipose tissue using receiver operating characteristic analysis of IDEAL MRI fat fraction maps. *Magn Reson Imaging.* 2018;51:61-68. doi:10.1016/j.mri.2018.04.013



Chapter 5

Image registration and mutual thresholding enable low inter-image variability across dynamic MRI measurements of supraclavicular brown adipose tissue during mild-cold exposure

This chapter has been submitted for publication.

Aashley S.D. Sardjoe Mishre
Borja Martinez-Tellez
Maaike E. Straat
Mariëtte R. Boon
Oleh Dzyubachyk
Andrew G. Webb
Patrick C.N. Rensen
Hermien E. Kan

ABSTRACT

Activated brown adipose tissue (BAT) enhances lipid catabolism, and improves cardio-metabolic health. Quantitative MRI of the fat fraction (FF) of supraclavicular BAT (scBAT) is a promising non-invasive measure to assess BAT activity, but suffers from high scan variability. We aimed to test the effects of co-registration and mutual thresholding on the scan variability in a fast (one-minute) time-resolution MRI protocol for assessing scBAT FF changes during cold exposure. Ten volunteers (age: 24.8 ± 3.0 years; BMI: 21.2 ± 2.1 kg/m²) were scanned during thermoneutrality (32°C; 10 min) and mild-cold exposure (18°C; 60 min) using a 12-point gradient-echo sequence (70 consecutive scans with breath-holds, 1.03 min per dynamic).

Dynamics were co-registered to the first thermoneutral scan, which enabled drawing of single regions of interest (ROIs) in the scBAT depot, and the trapezius muscle and humerus bone as control tissues. Voxel-wise FF changes were calculated at each time point and averaged across ROIs. We applied mutual FF thresholding, where voxels were included if their FF was >30% (scBAT), >0% (muscle) and >70% (bone) in the reference scan and the registered dynamic. The efficacy of the co-registration was determined by using a moving average, and comparing the mean squared error (MSE) of residuals between registered- and non-registered data. Registered scBAT Δ FF was compared to single-scan thresholding using the moving average method. scBAT FF changes were compared to control tissues using a mixed model analysis. Registered scBAT Δ FF had lower MSE values than non-registered data ($0.07\% \pm 0.05\%$ versus $0.16\% \pm 0.14$; $p < 0.05$), and mutual thresholding reduced the scBAT Δ FF variability by 30%. Relative to the control tissues, scBAT FF decreased during the last 30 minutes of cooling by $0.71 \pm 0.83\%$ and $0.74 \pm 0.84\%$ in muscle and bone, respectively.

We demonstrate that co-registration and mutual thresholding improve stability of the data two-fold, enabling assessment of small changes in FF upon cold exposure.

5.1 INTRODUCTION

Brown adipose tissue (BAT) is a thermogenic tissue that combusts fatty acids and glucose into heat. The most potent activator of BAT is cold exposure, upon which norepinephrine (NE) is released by sympathetic nerve endings in BAT: NE binds to β -adrenergic receptors on the brown adipocytes and activates a thermogenic program, including intracellular lipolysis¹. Chemical energy is converted to heat via the BAT-specific uncoupling protein 1 (UCP-1), and BAT activation leads to the combustion of intracellular lipid stores. These lipid stores are subsequently replenished by extracting lipids and glucose from the blood². Since BAT is involved in lipid- and glucose metabolism, many studies have addressed its protective role against obesity and cardiometabolic diseases³⁻⁶. In addition to using cold exposure⁷, pharmacological compounds such as mirabegron can also activate BAT⁸.

BAT activity during such challenges is usually indirectly assessed by quantifying the glucose uptake of the radioactively labelled glucose analogue [¹⁸F]fluorodeoxyglucose, using positron emission tomography/computed tomography (PET-CT)⁹. However, PET-CT suffers from well-recognized limitations: the invasive nature and radiation dose increase the participation burden and hamper longitudinal studies. In addition, this modality visualizes the glucose uptake, while BAT predominantly combusts lipids rather than glucose¹⁰. Most importantly, glucose uptake by BAT is reduced in individuals who are insulin resistant such as in obesity and type 2 diabetes, and therefore the technique is much less reliable in these patients¹⁰.

Magnetic resonance imaging (MRI) is a non-invasive and safe method for estimating supraclavicular BAT (scBAT) activity during cold exposure using chemical-shift-based water-fat separation sequences such as the Dixon technique for quantitative fat fraction (FF) mapping¹¹. In previous studies, cold-induced supraclavicular FF changes between -0.4 and -3.5% have been reported^{11,12}. Most of these studies have either used pre- and post-cooling assessments of scBAT FF¹² or have been performed without the use of image registration¹³⁻¹⁵ or breath-holds¹⁶⁻¹⁸. This may have resulted in increased variability in estimated FF changes over time since scBAT is located in the supraclavicular area, which renders measurements prone to movement artifacts. In addition, most studies acquired images at a relative coarse time resolution of 2.5-5 minutes^{13,18,19}. Since BAT activation occurs within 10 minutes after applying a cold stimulus^{13,20}, this temporal resolution may not be sufficient to study the short-time dynamics of BAT in detail.

Here, we aimed to minimize inter-scan variability by applying breath-holds and non-rigid image registration in a MRI protocol with a high temporal resolution for assessing FF dynamics in scBAT during cold exposure.

5.2 MATERIALS AND METHODS

5.2.1 Subjects

Ten healthy volunteers with an age between 18 and 25 years and a body mass index (BMI) between 18 and 25 kg/m² were recruited from our local healthy volunteer database and by using flyers. Exclusion criteria were the use of any medication known to affect lipid and/or glucose metabolism, recent excessive weight change, smoking and contra-indications for MRI. The study was performed in accordance with the Declaration of Helsinki and approved by the local medical ethics committee. Written consent was obtained from all participants prior to participation.

5.2.2. Study design and cooling protocol

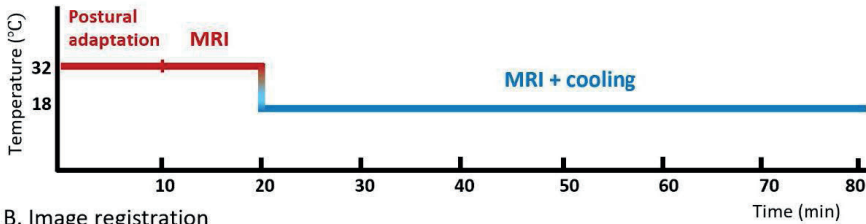
Participants were instructed to fast overnight for 12 hours, and to withhold from alcohol and caffeine consumption for 24 hours prior to the experiment. On the day of the experiment, participants were asked to wear a t-shirt, shorts and slippers. Body weight and height were measured and BMI was calculated by dividing the body weight by height squared (kg/m²). Participants then entered the MRI suite and were positioned on the MR table. A water circulating blanket, Blanketrol® III hyper-hypothermia system (Cincinnati Sub-Zero, Cincinnati, OH, USA), was placed on top of the participant and the temperature was initially set to 32°C. After 10 minutes at thermoneutrality, data were acquired for 10 minutes before the temperature was lowered to 18°C to initiate the standardized cooling protocol for BAT activation (**Fig. 1**). Every 10 to 15 minutes, participants were asked to score their cold perception using a numeric rating scale (NRS; 1=comfortable and 10=extremely cold). The total cooling duration was 60 minutes. The experiment was stopped in case of self-reported shivering. Scans were conducted at the same time of day in all participants (10.30 AM-12.00 PM) between April 16th and July 23rd, 2021.

5.2.3. Image acquisition

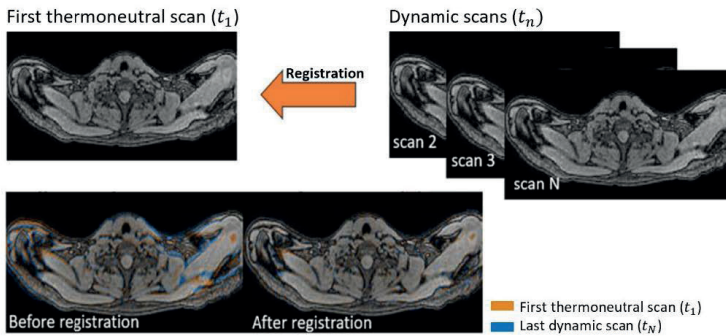
Data were acquired on a 3T MRI scanner (Philips Ingenia Elition X, Philips Healthcare, Best, The Netherlands) using a 16-channel head-and-neck coil, a 12-channel phased array placed on top of the subject, as well as the in-table 16-channel array for signal reception. A three-dimensional multi-gradient-echo sequence with twelve echoes (mDIXON Quant) was used with the following parameters: repetition time TR = 12 ms, first echo time TE = 1.12 ms, echo time separation $\Delta TE = 0.87$ ms, flip angle = 3°, field-of-view of 400×229×134 mm³ (Right-Left, Foot-Head, Anterior-Posterior), 2.1 mm isotropic resolution and breath hold time of 16 s. We used twelve echoes to ensure reliable T2* decay estimation²¹. The acquisition time per scan was 1.03 minutes, which yielded in total 70 scans: 10 scans at thermoneutrality and 60 scans during cooling.

To evaluate the stability of the sequence over time, a commercial phantom that consisted of twelve water-fat emulsion tubes (Calimatrix²¹) with low FFs (0%, 2.7%, 5.3%, 7.8%), intermediate FFs (10.1%, 15.5%, 20.4%, 23.6%) and high FFs (30.2%, 39.9%, 50.1%, 100%) was scanned for one hour at room temperature using a 16-channel head-and-neck coil with the previously described parameter settings.

A. MRI and cooling protocol



B. Image registration



C. ROI delineation and FF thresholding

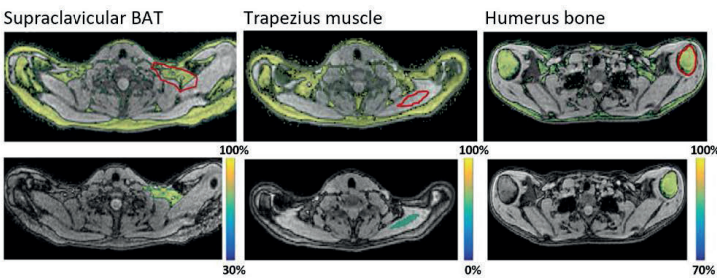


Figure 1. A) Participants underwent a standardized cooling protocol to activate BAT. After 20 minutes at thermoneutrality (32°C), the temperature was set to 18°C for one hour. Images were acquired during the last 10 minutes at thermoneutrality and during cooling. B) The first thermoneutral scan was used as a reference image, and all subsequent dynamic scans were co-registered to the first scan. First echo magnitude images were used for co-registration and the resulting transformation matrix was used to deform the FF map of each dynamic to match the image coordinates of the first thermoneutral scan. C) ROIs were only drawn on the first thermoneutral scan and voxels below 30% FF were mutually excluded in both fixed and dynamic scans to avoid inclusion of non-fatty tissue for scBAT. No FF thresholds were used for muscle and a 70-100% mutual FF threshold range was used for the humerus bone. Fat fraction (FF), Region of interest (ROI).

5.2.4 Water-fat data reconstruction

An in-house developed complex-based fitting algorithm was used to estimate voxel-based water and fat signals based on the known frequencies and amplitudes of the multiphase lipid spectrum²² and a mono-exponential decay of $T2^*$ ²³. The field inhomogeneity map obtained from the mDIXON Quant sequence was used as an initial estimate in the water-fat separation model. FF maps were subsequently calculated by dividing the fat signal by the sum of the water and fat signals in each voxel across the three-dimensional image.

5.2.5 Phantom data analysis

For analysis of the phantom data, a region of interest (ROI) was manually delineated for each phantom tube on the first scan. A single rectangular ROI was placed in the middle of each tube and ROIs were directly transferred to all subsequent dynamic scans. For each tube, voxel-wise FF differences between the first scan and each dynamic scan i , $\Delta FF_i(x,y,z) = FF_i(x,y,z) - FF_1(x,y,z)$, were computed and averaged across the ROI.

5.2.6 In vivo image registration and ROI segmentation

For analysis of the *in vivo* data, first-echo magnitude images of each dynamic were co-registered to the first thermoneutral scan (reference scan) using the open-access registration toolbox Elastix²³ (**Fig. 1B**). Dynamic images were iteratively deformed using a three-dimensional B-spline transform with a $10 \times 10 \times 10$ mm³ grid, adaptive stochastic gradient descent with two resolutions, 4000 iterations, and the Mattes mutual information as the similarity metric²⁴. As a result, ROIs only needed to be delineated on the first thermoneutral scan. ROIs were coarsely delineated in the scBAT depot, and we applied a mutual FF thresholding approach, where voxels were only included in the analysis, if their FF was above 30% in both the reference scan and the registered dynamic. As a control, ROIs were also drawn in the trapezius muscle and the humeral bone using 0–100% and 70–100% mutual FF threshold levels, respectively. Voxel-wise FF differences between the reference scan and each dynamic scan i : $\Delta FF_i(x,y,z) = FF_i(x,y,z) - FF_{TN1}(x,y,z)$ were calculated and averaged across the ROI.

5.2.7 Data analysis and statistics

The following analyses were performed to: i) determine the stability of the high-temporal-resolution MRI protocol, ii) evaluate the validity and added value of image registration, iii) evaluate the added value of mutual FF thresholding, and iv) compare cold-induced scBAT FF changes with control tissues.

Evaluating the stability of our high-temporal-resolution MRI protocol in the phantom

The temporal stability of the MRI protocol was evaluated by assessing FF changes of each phantom tube. For each tube, a trendline was fitted of scBAT FF changes using a linear

regression analysis. To quantify any decreasing or increasing trends, the vertical distance between the last and first point along the fitted trend line was determined.

Next, a moving average was computed along the FF changes of each phantom tube using a [-3,3] time window. As a measure of the variability, the mean squared error (MSE) of residuals between the moving average and the measured FF data was calculated. This method will be further referred to as the “*moving average method*”.

Evaluating the validity and added value of co-registration of in vivo data

The validity of the co-registration was assessed for each subject by registering the first thermoneutral (reference) scan to the dynamics in order to emulate the same extent of motion in the reference scan. This yielded a forward transformation (reference → dynamic) for each dynamic. Each dynamic scan was subsequently registered to the reference scan to obtain the backward transformation matrix (dynamic ← reference). For each dynamic, the forward and backward transformations were composed and applied to the reference scan to evaluate the registration error. FF difference maps were generated between the resulting deformed reference scan and the original one. The registration error was consecutively computed for each dynamic by taking the voxel-wise FF differences between the original reference scan and the deformed one, $\Delta FF_{\text{error}}(x,y,z) = FF_{\text{def}}(x,y,z) - FF_{\text{TN1}}(x,y,z)$, and averaged across the ROI in the scBAT area. To quantify any decreasing or increasing trends of the registration error, a trendline was fitted along the ΔFF_{error} time series for each participant. As a measure of the variability along the ΔFF_{error} time series, MSE values were computed for each participant using the moving average method.

The added value of the co-registration method was determined by comparing scBAT FF changes during cold exposure between registered- and non-registered data. The moving average method was used to determine the variability of scBAT ΔFF obtained from registered and non-registered data for each participant separately, as a measure for the intra-subject variability. Paired t-tests were performed to compare the intra-subject variability between registered and non-registered data.

Evaluating the added value of mutual FF thresholding of in vivo data

The added value of mutual FF thresholding was assessed by comparing scBAT FF changes obtained from mutual and single FF thresholding using the moving average method. Single FF thresholding was performed by applying a 30-100% FF threshold to each individual dynamic. Data were separately analysed for registered and non-registered scBAT FF changes, and paired t-tests were performed to compare the within-subject variability between mutual- and single FF thresholded data.

Comparing the scBAT FF response to control tissues (skeletal muscle and humerus bone)

Next, it was determined whether the scBAT FF changes over time differed from these estimated in control tissues: the trapezius muscle and the humerus bone. The moving average method was used to determine the variability of FF for both control tissues. Afterwards, the ΔFF time series of each control tissues were subtracted from the scBAT ΔFF time series, which yielded two difference curves: $\Delta FF_{scBAT} - \Delta FF_{trapezius}$ and $\Delta FF_{scBAT} - \Delta FF_{humerus}$. To prevent an overestimation of the statistical power, FF differences were averaged across every 10 minutes along the measurement interval resulting in seven temporal measurements. For each control tissue, it was determined whether the difference curve deviated from zero using a mixed model analysis. Thermal perception scores were compared between thermoneutrality and each cooling period using the Wilcoxon signed-rank test. Data analysis was performed using Matlab (version R2021a) and SPSS. Results were considered significant at $p < 0.05$.

5.3 RESULTS

Ten young and lean subjects (age=24.8±3.0 years and BMI=21.2±2.1 kg/m²) participated. Nine participants were female and one participant was male. All participants completed the protocol. Participants reported significantly higher cold perceptions compared to thermoneutrality (NRS=1.5±0.7) after 15 minutes of cooling (NRS=3.7±1.0; $p=0.004$), 30 minutes of cooling (NRS=3.6±0.9; $p=0.005$), 45 minutes of cooling (NRS=3.6±1.1; $p=0.007$) and after 1-h of cooling (NRS=4.1±1.3; $p=0.005$).

5.3.1 Phantom tubes with low, intermediate and high FFs show stable ΔFF measurements

Phantom tubes with low, intermediate, and high FFs showed stable ΔFF measurements over time (**Fig. 2A-C**). The vertical distance along the fitted trendlines were $-0.05\% \pm 0.08\%$ for the low FF tubes, $0.27\% \pm 0.10\%$ for the intermediate FF tubes and $0.05\% \pm 0.20\%$ for the high FF tubes. The MSE values were $0.02 \pm 0.005\%$ for the low FF tubes, $0.02 \pm 0.005\%$ for the intermediate FF tubes and $0.02 \pm 0.01\%$ for the high FF tubes.

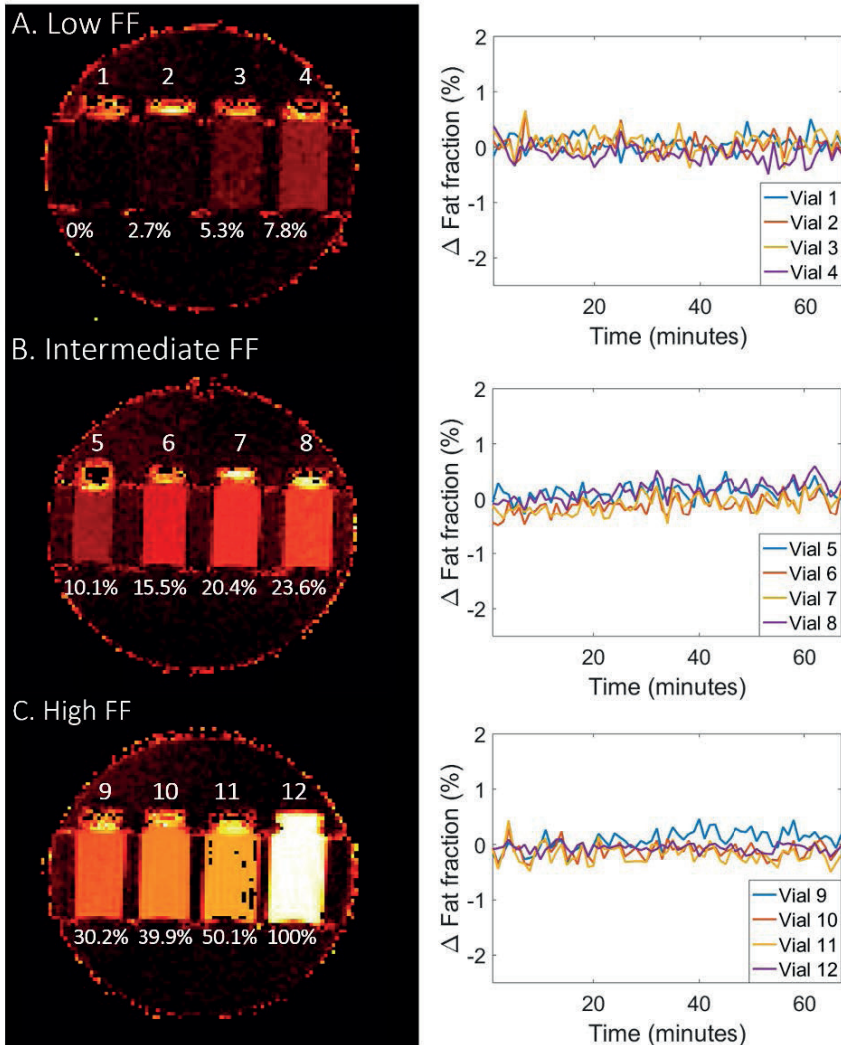


Figure 2. Fat fraction changes are plotted as a function of time for water-fat emulsion tubes in the A) low fat fraction (FF) range (0%, 2.7%, 5.3%, 7.8%), B) intermediate FF range (10.1%,15.5%,20.4%,23.6%) and C) high FF range (30.2%,39.9%,50.1%,100%).

5.3.2 Co-registration of in vivo data shows a negligible registration error over time and reduces the variability compared to non-registered data

The co-registration error caused substantially small FF changes over time (MSE:0.001%±0.002%; **Fig. 3A**), and resulted in a vertical distance of 0.003±0.01% along the fitted trendlines. The within-subject MSE values of registered scBAT Δ FF were lower compared to non-registered data (MSE: 0.07%±0.05% versus MSE:0.16%±0.14% respectively; $p=0.01$; **Fig. 3B-C**), and resulted in an increase in the Δ FF response over time by a factor of two.

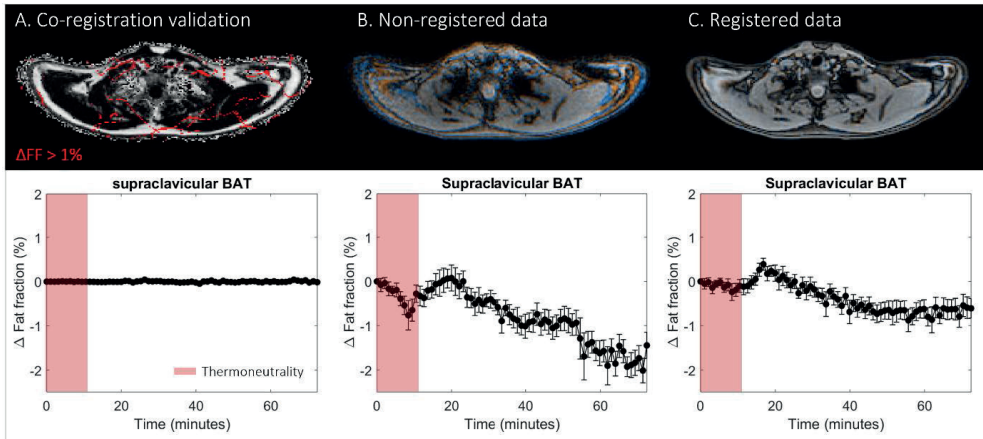


Figure 3. Fat fraction changes for the co-registration validation analysis (A), non-registered data (B) and registered data (C). scBAT fat fraction (FF) changes above 1% are shown in red in (A). Image overlap between the first thermoneutral (reference) scan and the last dynamic are shown for B and C, where the reference scan and the last dynamic are shown in orange and blue, respectively. Red denotes thermoneutrality.

5.3.3. Mutual FF thresholding reduces the variability of registered scBAT Δ FF data compared to single FF thresholding, while it increases the variability for non-registered data

For non-registered data, mutual FF thresholding increased the MSE values compared to single FF thresholding ($0.16\% \pm 0.14\%$ versus $0.13\% \pm 0.13\%$; $p=0.01$; **Fig. 4A**). For registered data, mutual FF thresholding reduced the MSE values compared to single FF thresholding, but this was not significant (MSE: $0.07\% \pm 0.05\%$ versus MSE: $0.10\% \pm 0.10\%$; $p=0.1$; **Fig. 4B**).

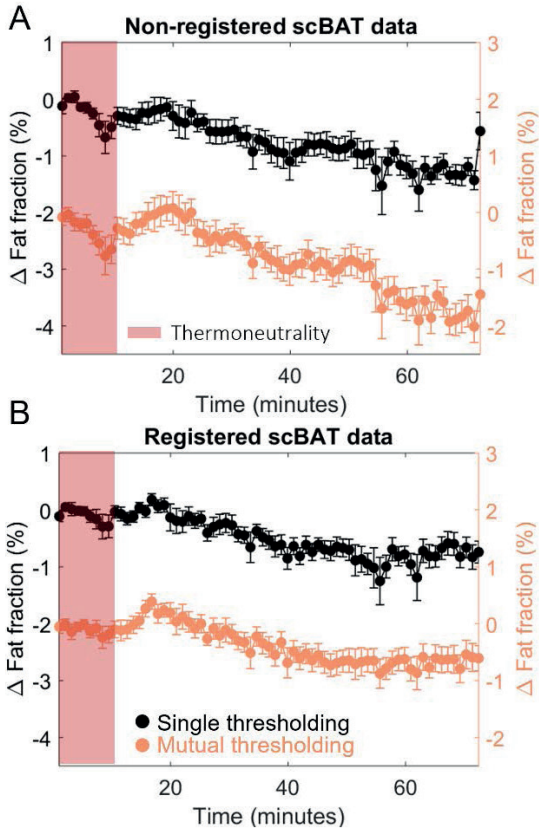


Figure 4. Fat fraction changes are shown for non-registered data (A) and registered data (B) after applying a 30-100% single fat fraction (FF) threshold (black) and mutual FF threshold (orange). Red denotes thermoneutrality.

5.3.4 The FF response in scBAT differs from control tissues during the last 30 minutes of cooling

As expected, FF changes in the trapezius muscle and the humerus bone revealed no specific FF patterns during cooling with small changes over time (skeletal muscle MSE: $0.05 \pm 0.05\%$ and humerus bone MSE: $0.11 \pm 0.06\%$; **Fig. 5A-B**). Δ FF in scBAT was significantly reduced by $-0.68 \pm 0.76\%$, $-0.80 \pm 0.88\%$ and $-0.66 \pm 0.81\%$ compared to Δ FF in the trapezius muscle at time intervals 5 (40-50 minutes), 6 (50-60 minutes) and 7 (60-70 minutes), respectively. Compared to the humerus bone, scBAT Δ FF was significantly reduced by $-0.39 \pm 0.61\%$ and $-0.43 \pm 0.46\%$ at time intervals 5 and 6 (**Fig. 5C**).

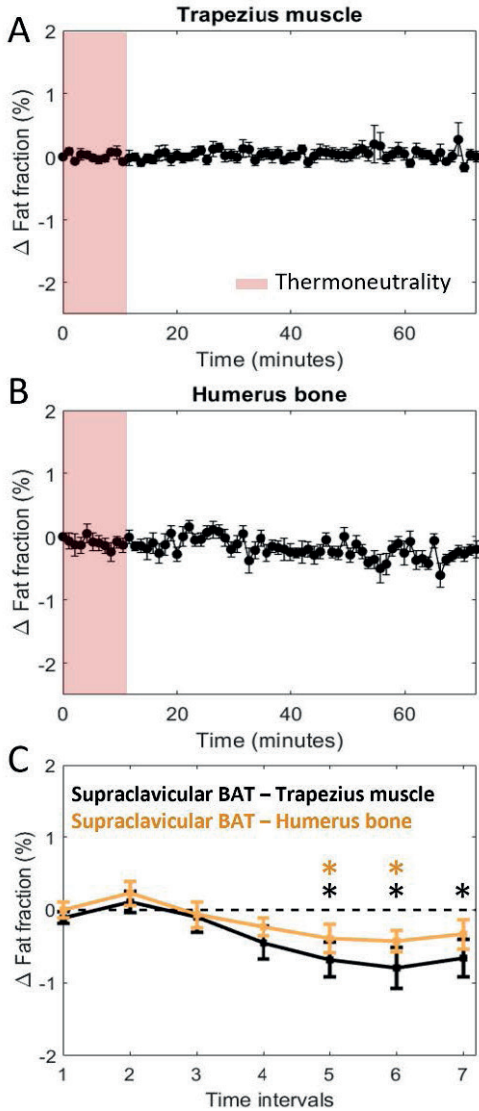


Figure 5. Fat fraction changes for the trapezius muscle and humerus bone are shown in A and B. Fat fraction (FF) difference curves between supraclavicular BAT, the trapezius muscle (black) and the humerus bone (orange) are shown in C. The FF difference curves are averaged across every 10 minutes along the measurement, which yielded seven time intervals. * $P < 0.05$.

5.4 DISCUSSION

In this work, we developed a 1-minute time resolution protocol for the assessment of sc-BAT FF changes using breath-holds and co-registration to minimize motion-induced variation. Our MRI protocol showed a high stability of FF in the phantom, and co-registration and mutual FF thresholding of *in vivo* data improved the stability of scBAT FF changes compared to non-registered data. Upon cold exposure, FF first increased in scBAT, and then decreased compared to control tissues.

Our MRI protocol resulted in a low variability of less than 0.1% FF in all phantom tubes over the entire scan duration of 70 minutes. No FF trend of 0.5% or higher occurred in any of the phantom tubes. In previous work, similar results were found regarding the repeatability of FF measurements in the Calimetrix phantom²¹, where a FF difference of 0.8% or lower between measurements that were performed on three different occasions was shown. Our data additionally show that the stability across FF measurements is maintained while acquiring images consecutively for 1-hour using a 1-minute time resolution. As such, influences from the scanner's hardware, e.g., B_0 drift, seem to have a minimal effect on the temporal stability of the FF measurements.

The validity of the co-registration method revealed a high registration accuracy of the *in vivo* data, indicated by the absence of any temporal pattern of the registration error and small FF changes over time. Due to the location of BAT in the supraclavicular area, the measurements are especially prone to movement artifacts. Indeed, our data show that co-registration reduces the within-subject variability two-fold compared to non-registered data while using mutual FF thresholding. This translated, on average, to double the scBAT FF reduction during cooling for non-registered data compared to registered data.

For non-registered data, mutual FF thresholding increased the within-subject variability by 23% compared to single FF thresholding. This increase is the result of large spatial mismatches between the reference scan and non-registered dynamics, which reduces the number of co-located voxels with a FF above 30% in both the reference scan and dynamic, thereby confirming the presence of motion across the dynamics. For registered data, mutual FF thresholding reduced the within-subject variability by 30% compared to single FF thresholded data. Since the spatial mismatches between the reference scan and registered dynamics are mostly resolved, the mutual thresholding approach only accounts for small spatial mismatches between scans that are still present after the registration, such as partial volume effects.

The added value of the co-registration is less pronounced when comparing registered- and non-registered data obtained with single FF thresholding, where the within-subject

variability was reduced by 23%. Nevertheless, by combining image registration and mutual FF thresholding, the within-subject variability of scBAT Δ FF (MSE: 0.07% \pm 0.05%) was further reduced by almost 2-fold compared to non-registered data obtained with single FF thresholding (MSE:0.13 \pm 0.13%) and mutual FF thresholding (MSE: 0.16 \pm 0.14). Our results, therefore highlight the importance of using both methods for these kind of tissues types that are prone to motion artefacts.

Compared to the literature where scans were obtained during cooling, our scBAT FF changes are generally smaller than those reported previously (-1.9%²⁰, -2.9%¹⁵, -3.0%^{14,18}, -3.5%²⁴, -4.7%¹⁹). This could be due to several reasons, including the lack of breath-holds and/or co-registration or differences in previous study protocols. As a result, the reported scBAT FF changes may have been overestimated as a result of motion. Several studies did use co-registration in their analysis^{13,19,20}, but images were acquired during free breathing. Since the registration error increases with the amount of image displacement²⁴, it cannot be excluded that this may have influenced the outcomes. A previous study by Stahl et al used both image registration and breath-holds in their protocol¹⁵, but images were acquired using a two-echo Dixon protocol. It has been shown that a two-echo sequence overestimates the FF below 60% and underestimates the FF above 60% compared to a six-echo protocol²⁵, which is the result of field inhomogeneities that are not corrected, and may therefore produce misleading scBAT Δ FF outcomes.

Moreover, differences in the applied cooling procedures (e.g., cooling garments, duration, intensity, medium (i.e., water or air) or strategy (i.e., personalized or standardized) may also have contributed to the inconsistency in FF outcomes in the literature. Although participants reported an increased cold perception during cooling, a larger Δ FF scBAT response may have occurred in previous studies^{18,19,24} since participants were exposed to lower temperatures compared to our standardized mild-cooling protocol (18°C). Since no thermal perception scores were reported in these previous studies, this hypothesis should be further tested by comparing thermal perception measurements and scBAT Δ FF outcomes across different cooling procedures.

Overall, scBAT FF changes were found to be significantly reduced with respect to the control tissues during the last 30 minutes of cooling. This gradual decrease in scBAT FF is most likely attributable to the combustion of lipids within the scBAT depot. While an increase in perfusion could produce a change in image intensity leading to an apparent reduction in scBAT FF, this seems unlikely for several reasons. First of all, Blondin et al. showed that BAT perfusion determined by ¹¹C-acetate PET-CT was unaltered after 3 hours of cold exposure in healthy adults, and that intracellular triglycerides were the primary fuel for BAT thermogenesis¹. Secondly, Coolbaugh et al. reported a mean FF decrease of 14% in voxels with a FF in the 90-100% decile after 1-hour of personalized cold exposure¹⁶. The

authors argued that if half of the water signal came from blood at thermoneutrality (e.g., assuming a blood volume fraction of 2.5% at baseline), then the blood volume fraction would have increased by 16.5% to explain this reduction of 14%, which is very unlikely. In addition, Lundstrom et al., showed that the reduction in scBAT FF determined by MRI persisted after the cooling was removed, which argues against perfusion being a dominant factor since it would then be expected that the perfusion would decrease¹⁷. Finally, the gradual FF increase (+0.4% FF) at the onset of cooling is not in line with a major role of perfusion, as increased perfusion would be accompanied by an apparent immediate decrease scBAT FF due to the increased volume fraction of water.

To the best of our knowledge, this increase in FF upon cooling has not been reported before, but could be due to lipid uptake in scBAT from the blood prior to combustion. This would be in line with recent data from Straat et al., who showed that plasma triglyceride (TG) levels transiently decreased in response to cold exposure²⁶. We postulate that soon after the initiation of cold exposure, BAT rapidly increases the uptake of triglyceride-derived fatty acids, resulting in the observed initial scBAT FF increase. Then, after eight minutes, the combustion of intracellular lipids possibly exceeds the uptake of fatty acids, leading to an overall decrease in scBAT FF. Future research could, therefore, combine these measures with repeated blood sampling to experimentally address this hypothesis.

This study has several limitations: in our protocol, 140 breath-holds of 16s were needed from the subject, which involved a high burden for patients. Since our data showed an inter-image variability (MSE) of less than 0.1% in scBAT, this may allow the use of lower time resolutions at intervals for which scBAT FF changes are stable (e.g., thermoneutrality or prolonged cooling¹⁴). Another limitation is that the study population only included young and healthy adults, and thus our results cannot be extrapolated to more general populations.

In conclusion, our MRI protocol and analysis pipeline enables 1-minute resolution measurements of scBAT Δ FF with a small inter-image variability. Co-registration and mutual FF thresholding showed a two-fold lower variability compared to non-registered data, and its use is therefore highly recommended to improve the stability of scBAT Δ FF measurements.

REFERENCES

1. Blondin DP, Frisch F, Phoenix S, et al. Inhibition of Intracellular Triglyceride Lipolysis Suppresses Cold-Induced Brown Adipose Tissue Metabolism and Increases Shivering in Humans. *Cell Metabolism*. 2017;25(2):438-447. doi:10.1016/j.cmet.2016.12.005
2. Bartelt A, Bruns OT, Reimer R, et al. Brown adipose tissue activity controls triglyceride clearance. *Nature Medicine*. 2011;17(2):200-206. doi:10.1038/nm.2297
3. Oikonomou EK, Antoniades C. The role of adipose tissue in cardiovascular health and disease. *Nature Reviews Cardiology*. 2019;16(2):83-99. doi:10.1038/s41569-018-0097-6
4. Becher T, Palanisamy S, Kramer DJ, et al. Brown adipose tissue is associated with cardiometabolic health. *Nature Medicine*. 2021;27(1):58-65. doi:10.1038/s41591-020-1126-7
5. Van Der Lans AAJJ, Hoeks J, Brans B, et al. Cold acclimation recruits human brown fat and increases nonshivering thermogenesis. *Journal of Clinical Investigation*. 2013;123(8):3395-3403. doi:10.1172/JCI68993
6. Yoneshiro T, Aita S, Matsushita M, et al. Recruited brown adipose tissue as an antiobesity agent in humans. *The Journal of Clinical Investigation*. 2013;123(8):3404-3408. doi:10.1172/JCI67803
7. Cannon B, Nedergaard J. Brown Adipose Tissue: Function and Physiological Significance. *Physiological Reviews*. 2004;84(1):277-359. doi:https://doi.org/10.1152/physrev.00015.2003
8. Cypess AM, Weiner LS, Roberts-Toler C, et al. Activation of human brown adipose tissue by a β 3-adrenergic receptor agonist. *Cell metabolism*. 2015;21(1):33-38. doi:10.1016/J.CMET.2014.12.009
9. Chen KY, Cypess AM, Laughlin MR, et al. Brown Adipose Reporting Criteria in Imaging Studies (BARCIST 1.0): Recommendations for Standardized FDG-PET/CT Experiments in Humans. *Cell Metabolism*. 2016;24(2):210-222. doi:10.1016/j.cmet.2016.07.014
10. Schilperoort M, Hoeke G, Kooijman S, Rensen PCN. Relevance of lipid metabolism for brown fat visualization and quantification. *Current Opinion in Lipidology*. 2016;27(3):242-248. doi:10.1097/MOL.0000000000000296
11. Karampinos DC, Weidlich D, Wu M, Hu HH, Franz D. Techniques and Applications of Magnetic Resonance Imaging for Studying Brown Adipose Tissue Morphometry and Function. *Handbook of experimental pharmacology*. 2019;251:299-324. doi:10.1007/164_2018_158
12. Wu M, Junker D, Branca RT, Karampinos DC. Magnetic Resonance Imaging Techniques for Brown Adipose Tissue Detection. *Frontiers in Endocrinology*. 2020;11:421. doi:10.3389/FENDO.2020.00421/FULL
13. Gashi G, Madoer P, Maushart CI, et al. MRI characteristics of supraclavicular brown adipose tissue in relation to cold-induced thermogenesis in healthy human adults. *Journal of Magnetic Resonance Imaging*. 2019;50(4):1160-1168. doi:10.1002/jmri.26733
14. Oreskovich S, Ong F, Ahmed B, et al. Magnetic resonance imaging reveals human brown adipose tissue is rapidly activated in response to cold. *Journal of the Endocrine Society*. Published online October 14, 2019. doi:10.1210/js.2019-00309
15. Stahl V, Maier F, Freitag MT, et al. In vivo assessment of cold stimulation effects on the fat fraction of brown adipose tissue using DIXON MRI. *Journal of Magnetic Resonance Imaging*. 2017;45(2):369-380. doi:10.1002/jmri.25364
16. Reber J, Willershäuser M, Karlas A, et al. Non-invasive Measurement of Brown Fat Metabolism Based on Optoacoustic Imaging of Hemoglobin Gradients. *Cell metabolism*. 2018;27(3):689-701.e4. doi:10.1016/j.cmet.2018.02.002

17. Deng J, Neff LM, Rubert NC, et al. MRI characterization of brown adipose tissue under thermal challenges in normal weight, overweight, and obese young men. *Journal of magnetic resonance imaging : JMRI*. 2018;47(4):936-947. doi:10.1002/jmri.25836
18. Holstila M, Pesola M, Saari T, et al. MR signal-fat-fraction analysis and T2* weighted imaging measure BAT reliably on humans without cold exposure. *Metabolism: Clinical and Experimental*. 2017;70:23-30. doi:10.1016/j.metabol.2017.02.001
19. Coolbaugh CL, Damon BM, Bush EC, Welch EB, Towse TF. Cold exposure induces dynamic, heterogeneous alterations in human brown adipose tissue lipid content. *Scientific Reports*. 2019;9(1):13600. doi:10.1038/s41598-019-49936-x
20. Lundström E, Strand R, Johansson L, Bergsten P, Ahlström H, Kullberg J. Magnetic resonance imaging cooling-reheating protocol indicates decreased fat fraction via lipid consumption in suspected brown adipose tissue. *PLoS ONE*. 2015;10(4). doi:10.1371/journal.pone.0126705
21. Hu HH, Yokoo T, Bashir MR, et al. Linearity and bias of proton density fat fraction as a quantitative imaging biomarker: A multicenter, multiplatform, multivendor phantom study. *Radiology*. 2021;298(3):640-651. doi:10.1148/RADIOL.2021202912/ASSET/IMAGES/LARGE/RADIOL.2021202912.TBL6.JPEG
22. Wang X, Hernando D, Reeder SB. Sensitivity of Chemical Shift-Encoded Fat Quantification to Calibration of Fat MR Spectrum. *Magnetic resonance in medicine*. 2016;75(2):845. doi:10.1002/MRM.25681
23. Abreu-Vieira G, Sardjoe Mishre A.S.D, Burakiewicz J, janssen L.G.M, Nahoj K.J, van der Eijk J.A, Riem T.T, Boon M.R, Dzyubachyk O, Webb A.G, Rensen P.C.N KHE. Human brown adipose tissue estimated with magnetic resonance imaging undergoes changes in composition after cold exposure: an in vivo MRI study in healthy volunteers. *Frontiers in Endocrinology*.
24. Kadoya N, Fujita Y, Katsuta Y, et al. Evaluation of various deformable image registration algorithms for thoracic images. *Journal of radiation research*. 2014;55(1):175-182. doi:10.1093/JRR/RRT093
25. Abreu-Vieira G, Sardjoe Mishre ASD, Burakiewicz J, et al. Human Brown Adipose Tissue Estimated With Magnetic Resonance Imaging Undergoes Changes in Composition After Cold Exposure: An in vivo MRI Study in Healthy Volunteers. *Frontiers in Endocrinology*. 2020;10. doi:10.3389/fendo.2019.00898
26. Cold Exposure Induces Dynamic Changes in Circulating Triacylglycerol Species, Which is Dependent on Intracellular Lipolysis: A Randomized Cross-Over by Maaïke Straat, Lucas Jurado Fasoli, Zhixiong Ying, Kimberly Nahon, Laura Janssen, Mariëtte Boon, Gernot Grabner, Sander Kooijman, Robert Zimmermann, Martin Giera, Patrick C.N. Rensen, Borja Martinez :: SSRN. Accessed July 20, 2022. https://papers.ssrn.com/sol3/papers.cfm?abstract_id=4163695



Chapter 6

Summary, general discussion and
future perspectives



6.1 SUMMARY

The primary aim of this thesis was to improve the overall methodology for assessing supraclavicular BAT (scBAT) activity in human adults to enable evaluation of BAT-targeted therapies against cardiovascular diseases. In **Chapter 1**, we introduced the physiology and morphology of BAT, as well as strategies for BAT activation and imaging techniques for BAT detection in human adults. In **chapter 2**, we assessed how body composition and scBAT activity influenced the human cold tolerance capacity such that cooling strategies may be further optimized to ensure maximal BAT stimulation. In **chapters 3, 4 and 5**, we focused on the development of non-invasive methods to facilitate their translation to clinical research on BAT.

In **chapter 2**, we investigated the association of the shivering threshold time, as a proxy for the cold tolerance capacity, with body composition, scBAT activity and volume as measured with ^{18}F -FDG PET-CT, the perception of shivering and skin temperature in young adults. We showed that interindividual differences in body type attribute to the shivering response: the cold tolerance capacity was related to body composition in females, and to body size in males and females. However, we found that the amount of metabolically activated scBAT did not seem to associate with the cold tolerance capacity, indicating that an individual with a higher amount of metabolically active BAT, and thereby a potentially higher capacity of BAT thermogenesis, could elicit the same cold tolerance capacity as an individual with less metabolically active BAT. Our findings, therefore, suggest that body size and composition should be considered when applying cooling protocols in heterogeneous study populations regardless of the amount of activated BAT.

In the next chapters, we shifted our focus towards non-invasive imaging modalities: IRT (**chapter 3**) and MRI (**chapter 4 and chapter 5**). We developed an open-access semi-automated segmentation tool (the IRT-toolbox) in **chapter 3** for measuring skin temperatures in the thoracic area to estimate scBAT activity. The main features of the IRT-toolbox are image alignment and non-rigid image registration, which enable a full image overlap between all follow-up images and the baseline image within a participant's dataset. As a result, the drawing time the ROIs was substantially reduced to a single image per dataset, while maintaining the inter-user reliability as compared to manual segmentations.

Since IRT only provides two-dimensional surface temperatures, we focused on quantitative MRI fat fraction (FF) mapping for detecting scBAT FF *in vivo* in the next chapters. Previous MRI studies have consistently reported FF reductions after cold exposure, which is most likely attributed to the combustion of lipids with brown adipocytes. Yet, reports on the extent of FF changes vary in the literature. Differences in selected FF threshold ranges for scBAT segmentation could be an explanation for this. Indeed, in **chapter 4**,

we showed that after 2-h of personalized cold exposure, FF predominantly decreased in lipid-rich regions within the scBAT depot, whereas FF increased in lipid-poor regions. We demonstrated that by increasing the lower FF threshold level (e.g., from 30-100% to 50-100%), pre-and post-cooling FF differences became less pronounced, whereas estimated pre-and post-cooling scBAT volume differences became larger in magnitude. Due to the heterogenous nature of the scBAT depot in human adults, the use of FF thresholding influences the magnitude and direction of scBAT outcomes. Therefore, future studies should carefully consider the use of FF thresholds when analyzing scBAT in human adults.

In the study described in **chapter 4**, two MRI scans were acquired per individual: one timepoint before cooling and one timepoint after 2-hours of cooling. This does not provide insight into the time course of scBAT activity. In addition, since scBAT is located in the supraclavicular area, measurements can be prone to motion-induced variability. In **chapter 5**, we aimed to minimize this variability across dynamic FF measurements using a high-time resolution protocol for assessing FF dynamics in scBAT during cold exposure. We used breath-holds in our image acquisition protocol, and image registration and mutual FF thresholding in our analysis to minimize motion artefacts. We used mutual FF thresholding in our analysis to segment scBAT more accurately, and we applied a 30-100% FF range based on results from **chapter 4**. We demonstrated that the use of motion-correcting techniques, such as non-rigid image registration and mutual FF thresholding improve the stability of our data by 30%.

6.2 GENERAL DISCUSSION

To bring our results into perspective with the literature, we date back to 2009, where three different research groups identified metabolically active brown adipose tissue (BAT) in human adults using [^{18}F]FDG-PET-CT¹⁻³. Since then, multiple studies have been performed that confirmed the presence of metabolically active BAT, reinvigorating interest of its implications in cardiovascular health⁴⁻⁷. While activation of BAT emerged as a potential strategy in cardiovascular health, research focused on the development of non-invasive and safer alternatives to [^{18}F]FDG-PET-CT to detect activated BAT, with the ultimate goal to facilitate clinical research on therapies (in)directly targeting BAT.

In 2011, the potential of IRT as an indirect measure of supraclavicular BAT (scBAT) activity was first demonstrated in healthy adults⁸. That study reported a smaller reduction in supraclavicular skin temperature (-0.9°C) after cooling compared to a reference tissue (mediastinal region; -2.0°C) potentially reflecting the thermogenic capacity of BAT. Since then, IRT has been increasingly used for the assessment of BAT activity in response to cold, either in standalone settings⁹⁻¹⁴ or in combination with other techniques, such as

[¹⁸F]FDG-PET-CT¹⁵⁻¹⁹. In most studies, however, ROIs were manually drawn for analysis. This can be very time consuming in large datasets and prone to ROI drawing variability. We developed the semi-automated segmentation tool: *the IRT-toolbox* in **chapter 3** to address these limitations. The most important feature of our toolbox is non-rigid image registration: this post-processing technique enables a stepwise deformation of a target image to fully overlap with a given reference image. We applied this method to enable a full image overlap between all follow-up images and the baseline image within each participant's dataset. As a result, ROI drawing was solely required on the baseline image within each dataset. Our toolbox therefore substantially reduced the ROI drawing time to a single image per dataset, while maintaining the same user reliability compared to manual segmentations. The IRT-toolbox is freely available (https://github.com/AashleySD/IRT_toolbox) and ready for clinical applications.

While IRT has been more frequently applied over the years, MRI fat fraction (FF) imaging concurrently gained interest as an indirect readout for scBAT activity. In 2013, Hu et al²⁰ identified morphological differences between scBAT and WAT using both post-mortem and in vivo MRI in infants, adolescents and adults. Lower FFs were found in the scBAT depot with a more granular appearance compared to WAT. Similarly, van Rooijen et al²¹ reported a FF of approximately 66% in supraclavicular and cervical depots in adults, which was 16.3% lower compared to the FF in white adipose tissue. That study additionally acquired [¹⁸F]FDG-PET-CT images as a reference method, and showed that the FF of the supraclavicular/cervical regions did not correlate with the glucose uptake. Thereafter, several validation studies were performed that simultaneously used [¹⁸F]FDG-PET-CT and MRI to assess the correlation between scBAT FF and [¹⁸F]FDG uptake in scBAT. For instance, McCallister et al showed a good correlation between these parameters only when subjects showed a substantially high glucose uptake²², while Fisher et al²³ and Sun et al²⁴ showed that only 40% of the variation in scBAT [¹⁸F]FDG uptake was explained by MRI FF. These moderate correlations may reflect the underlying difference between the physiological responses of these readouts, as [¹⁸F]FDG-PET-CT measures glucose uptake, and MRI-derived FF reflects lipid metabolism, and indirectly glucose metabolism due to de novo lipogenesis. Meanwhile, studies continued on exploring MRI as a standalone modality, quantifying the change after cold exposure with respect to warm conditions (scBAT ΔFF) as a measure for scBAT activity. These studies reported a relatively small reduction of scBAT FF after cold exposure and with varying magnitude (-0.4%, -4.7%)^{25,26}. In line with the literature, we found a FF decrease of -3.5% after two hours of personalized cold-exposure in **chapter 4**. At the same time, we found that heterogenous changes occurred across the entire depot: lipid-rich regions in the scBAT depot decreased in fat fraction, whereas lipid-poor regions increased in fat fraction. Similar findings were reported by Coolbaugh et al²⁷ where regions in the scBAT depot that were grouped at lower baseline fat fractions (0-30%) exhibited a FF increase after cooling, whereas regions grouped at higher FFs (60-100%) showed a FF

decrease in response to cold. As such, the net balance in scBAT FF is most likely determined by the combustion- and uptake of lipids, which on average, causes a relatively small effect in cold-induced FF outcomes as reported in the literature. In addition, in **chapter 4**, we demonstrated that the selection of FF thresholds for scBAT segmentation influence the magnitude of scBAT MR outcomes. Here, we demonstrated that by increasing the lower FF threshold level (e.g., 30-100% → 50-100%), pre-and post-cooling FF differences became smaller, whereas estimated pre-and post-cooling scBAT volume differences became larger. As such, these results indicate that differences in FF segmentation thresholds could have contributed to the varying magnitude of scBAT FF changes in the literature, and thus care should be taken when selecting FF thresholds for analysis.

The first MRI studies that were performed to assess scBAT usually acquired MRI scans one timepoint before- and one timepoint after cold exposure. Several studies switched to dynamic scanning where MRI scans were repeatedly performed to obtain insight into the time evolution of scBAT activity during cold exposure^{27–31}. Most of these studies performed dynamic MRI measurements without the use of motion-correcting methods such as breath-holds or image registration. Since scBAT is located in the supraclavicular area, and thus prone to motion, scBAT FF results may become more variable when no motion correction is applied. Given the small decrease in scBAT MRI FF upon cold exposure, any variability due to motion should be minimized to ensure a reliable detection of scBAT. We addressed this in **chapter 5**, where we showed a low inter-image variability of less than 0.1% across 1-minute time resolution MRI measurements of scBAT FF changes during cold exposure. To obtain this low variability, we used breath-holds in our acquisition, and non-rigid image registration and an optimized scBAT segmentation procedure in our analysis pipeline. At the same time, we demonstrated that scBAT FF changes can be overestimated by two-fold when motion-induced variability is not taken into account. A lack of these motion-correcting techniques could therefore have produced larger scBAT FF reductions in studies that did not use breath-holds (-4.7%, -1.94)^{27,29} or non-rigid image registration (-3.0%)^{30,31}. Our results therefore highlight the importance of using breath-holds, non-rigid image registration and mutual thresholding in tissues such as scBAT that are prone to movement artefacts.

The small reduction in scBAT FF upon cold exposure additionally requires that the applied stimuli sufficiently activate BAT to measure a detectable FF change. In **chapter 2**, we showed that differences in body size and composition may invoke different cold perceptions between individuals. As a consequence, the magnitude of scBAT FF changes upon cold exposure could be smaller in individuals that experience less cold compared to others due to e.g., better insulation traits. Moreover, results from **chapters 4** and **5** suggest that the amount of activated BAT may depend on the applied cooling procedure. For instance, we used a personalized cooling protocol for BAT activation in **chapter 4**,

resulting in a cold-induced scBAT FF difference of -3.5%, whereas this change was almost 6 times lower (-0.61%) when we applied standardized mild-cooling (18 °C) in **chapter 5**. Interestingly, Oreskovich et al³¹ also applied a mild-cooling procedure at 18°C, but used a liquid-conditioned suit instead of a water circulating blanket. They reported a scBAT FF reduction of -3.0%, which is substantially higher than the results from **chapter 5** (-0.61%). Besides differences in cooling garments, lower cooling intensities most likely cause a larger reduction in scBAT FF. As such, a previous study by Stahl et al²⁸ reported a scBAT FF reduction of -2.9% after 1.5 hours of standardized cooling at 12°C. Coolbaugh²⁷ and Deng³⁰ also reported a FF reduction of -4.7% and -3.0% after applying one hour of personalized cold exposure (down to a minimum temperature of 10°C and 13°C, respectively). Altogether, these results suggest that cooling protocols should be carefully selected to ensure maximal scBAT activation, thereby enhancing the chance for scBAT detection, and especially among individuals with varying body types.

While promising efforts have been made towards the use of IRT and MRI as alternatives for [¹⁸F]FDG PET-CT, tracers other than the glucose analogue [¹⁸F]FDG have been evaluated as well. For instance, U din et al³² used the radiotracers [¹⁵O]O₂, [¹⁵O]H₂O, and [¹⁸F]FTHA to measure oxygen consumption, blood flow, and non-esterified fatty acids (NEFA) uptake, respectively. That study reported an almost two-fold increase in oxygen consumption and blood flow as well as an increase in NEFA uptake in scBAT after cold exposure. The advantages of the [¹⁵O]O₂ tracer are its independency on substrate availability, as well as its non-invasiveness as the tracer is administered via a mask. However, the [¹⁵O]O₂ tracer has a very short half-life of approximately two minutes, which could hamper measurements due to logistical reasons. Moreover, the [¹⁸F]FTHA tracer reflects the uptake of free fatty acids, whereas BAT mainly extracts fatty acids from triglyceride-rich lipoproteins. As such, the development of a lipoprotein-derived FA tracer would be very valuable in this line of research as it could provide a better representation of the lipid uptake by scBAT. Combining this tracer with MRI FF mapping may allow a higher accuracy in detecting the uptake and combustion of lipids considering the high resolution of MRI and its ability to detect lipid changes across the entire scBAT volume (**chapters 4 and 5**).

6.3 FUTURE PERSPECTIVES

Our results demonstrate the potential of using IRT and MR imaging as safer alternatives compared to [¹⁸F]FDG-PET-CT, but future work is needed to establish their use in clinical research. More specifically, the target population for BAT-related research mainly consist of overweight individuals and individuals living with obesity. It remains questionable whether IRT can be used in such subject populations since it has been shown that the thickness of the subcutaneous fat layer inversely relates to skin temperature outcomes³³.

Studies should therefore focus on evaluating the feasibility of IRT for the assessment of supraclavicular skin temperature in individuals with varying body types.

The advantage of MRI is that FF outcomes are not limited to the surface area since this technique enables a three-dimensional assessment of the entire depot. While research on MRI measurements in overweight and obese individuals is limited, Deng et al³⁰ reported a scBAT FF reduction of ~1.0% in four overweight and two obese individuals after personalized cold exposure. Albeit preliminary, this report demonstrates the potential of MRI in detecting small FF changes in overweight and/or obese individuals that have less active BAT compared to lean controls. Prior to extending these measurements towards larger (patient) populations, we would first recommend to further establish the validity of MRI for active BAT detection. Previous studies have compared scBAT FF outcomes to other methods like [¹⁸F]FDG-PET-CT and whole body measures. Gashi et al investigated the correlation between scBAT FF and cold-induced changes in resting energy expenditure (REE)³⁴, where scBAT did not contribute to the change in REE. While BAT comprises of approximately 0.1% of body weight (~70 g), earlier work has estimated that 50 g of activated BAT can increase energy expenditure by 20%¹. However, the contribution of BAT on whole body energy expenditure is under debate. For instance, Din et al showed that BAT contributes only ~1% of whole body energy expenditure³², and that the remaining increase (range 2-47%) in whole-body energy expenditure in response to cold is predominantly mediated by shivering, which is the well-known form of thermogenesis produced by skeletal muscle.

In order to further elucidate the physiological mechanisms that may be associated to the supraclavicular MRI-derived FF changes upon cold exposure, MR imaging could be combined with repeated blood sampling. Since active BAT rapidly replenishes intracellular lipid stores by extracting lipids from the circulation, future work should compare scBAT FF changes to plasma lipid measurements.

In the literature, a wide variety of cooling protocols, imaging protocols and analysis pipelines have been described for both IRT and MRI, which hampers the comparison of BAT outcomes between research centers. In 2018, the BARCIST criteria were established to recommend on the use of protocols and analyses for assessing BAT activity using [¹⁸F]FDG-PET-CT³⁵. As a future perspective, it would be very useful to establish such criteria for IRT and MRI. Focusing on the target population for BAT-related research, this requires that cooling- and imaging protocols are optimized and tailored to individuals with different phenotypical features. For instance, in **chapter 2** of this thesis, 25 out of 110 participants did not report shivering during the personalized cooling procedure, and showed a higher whole-body adiposity compared to the participants that reported shivering. Personalized cooling protocols usually start at an initial temperature followed by a stepwise decrease in

temperature (e.g., 5°C every 10 minutes) until shivering occurs or a minimal temperature is reached. These temperature settings could be further optimized in different subgroups characterized by BMI and/or sex using e.g., larger step sizes when lowering the temperature or a lower minimum temperature for individuals that can preserve heat better compared to others. Another important aspect is to recommend on analysis methods that may affect BAT-related outcomes such as including co-registration in the analysis, or the selection of scBAT FFF segmentation thresholds. Altogether, standardizing protocols may contribute in facilitating the interpretation of BAT-related outcomes between research centers.

6.4 CONCLUSION

The primary aim of this thesis was to improve the overall methodology for assessing scBAT activity in human adults to enable evaluation of therapies (in)directly targeting BAT. The studies in this thesis have improved the feasibility of using non-invasive methods such as IRT and MRI for the assessment of scBAT activity in human adults and have led to a better understanding of the physiological mechanisms that influence the cold tolerance capacity in human adults. We showed the amount of activated BAT could vary among individuals with different body types and that cooling protocols should be carefully selected, especially in heterogenous study populations. With regards to imaging, we strongly recommend to use motion-correcting methods such as non-rigid image registration to correct for motion-induced variability, and to reduce the analysis time. Finally, due to the heterogenous nature of the scBAT depot in human adults, the use of FF thresholds for analysis should be carefully considered.

REFERENCES

1. Cypess AM, Lehman S, Williams G, et al. Identification and importance of brown adipose tissue in adult humans. *N Engl J Med*. 2009;360(15):1509-1517. doi:10.1056/NEJMoa0810780
2. Virtanen KA, Lidell ME, Orava J, et al. Functional Brown Adipose Tissue in Healthy Adults. *N Engl J Med*. 2009;360(15):1518-1525. doi:10.1056/nejmoa0808949
3. Van Marken Lichtenbelt WD, Vanhommerig JW, Smulders NM, et al. Cold-activated brown adipose tissue in healthy men. *N Engl J Med*. 2009;360(15):1500-1508. doi:10.1056/NEJMoa0808718
4. Hanssen MJW, Hoeks J, Brans B, et al. Short-term cold acclimation improves insulin sensitivity in patients with type 2 diabetes mellitus. *Nat Med*. 2015;21(8):863-865. doi:10.1038/nm.3891
5. Becher T, Palanisamy S, Kramer DJ, et al. Brown adipose tissue is associated with cardiometabolic health. *Nat Med*. 2021;27(1):58-65. doi:10.1038/S41591-020-1126-7
6. Takx RAP, Ishai A, Truong QA, MacNabb MH, Scherrer-Crosbie M, Tawakol A. Supraclavicular Brown Adipose Tissue 18F-FDG Uptake and Cardiovascular Disease. *J Nucl Med*. 2016;57(8):1221-1225. doi:10.2967/JNUMED.115.166025
7. Oikonomou EK, Antoniades C. The role of adipose tissue in cardiovascular health and disease. *Nat Rev Cardiol*. 2019;16(2):83-99. doi:10.1038/s41569-018-0097-6
8. Lee P, Ho KKY, Lee P, Greenfield JR, Ho KKY, Greenfield JR. Hot fat in a cool man: infrared thermography and brown adipose tissue. *Diabetes, Obes Metab*. 2011;13(1):92-93. doi:10.1111/J.1463-1326.2010.01318.X
9. Symonds ME, Henderson K, Elvidge L, et al. Thermal imaging to assess age-related changes of skin temperature within the supraclavicular region co-locating with brown adipose tissue in healthy children. *J Pediatr*. 2012;161(5):892-898. doi:10.1016/J.JPEDI.2012.04.056
10. Robinson L, Ojha S, Symonds ME, Budge H. Body Mass Index as a Determinant of Brown Adipose Tissue Function in Healthy Children. *J Pediatr*. 2014;164(2):318-322.e1. doi:10.1016/J.JPEDI.2013.10.005
11. Hadi H El, Frascati A, Granzotto M, et al. Infrared thermography for indirect assessment of activation of brown adipose tissue in lean and obese male subjects. *Physiol Meas*. 2016;37(12):N118. doi:10.1088/0967-3334/37/12/N118
12. Ang QY, Goh HJ, Cao Y, et al. A new method of infrared thermography for quantification of brown adipose tissue activation in healthy adults (TACTICAL): a randomized trial. *J Physiol Sci*. 2017;67(3):395-406. doi:10.1007/S12576-016-0472-1
13. Ong FJ, Ahmed BA, Oreskovich SM, et al. Recent advances in the detection of brown adipose tissue in adult humans: A review. *Clin Sci*. 2018;132(10):1039-1054. doi:10.1042/CS20170276
14. Hartwig V, Guiducci L, Marinelli M, et al. Multimodal Imaging for the Detection of Brown Adipose Tissue Activation in Women: A Pilot Study Using NIRS and Infrared Thermography. *J Healthc Eng*. 2017;2017. doi:10.1155/2017/5986452
15. Jang C, Jalapu S, Thuzar M, et al. Infrared thermography in the detection of brown adipose tissue in humans. *Physiol Rep*. 2014;2(11):e12167. doi:10.14814/PHY2.12167
16. Gatidis S, Schmidt H, Pfannenber CA, Nikolaou K, Schick F, Schwenzer NF. Is It Possible to Detect Activated Brown Adipose Tissue in Humans Using Single-Time-Point Infrared Thermography under Thermoneutral Conditions? Impact of BMI and Subcutaneous Adipose Tissue Thickness. *PLoS One*. 2016;11(3). doi:10.1371/JOURNAL.PONE.0151152
17. J L, DE M, C I-E, et al. Thermal Imaging Is a Noninvasive Alternative to PET/CT for Measurement of Brown Adipose Tissue Activity in Humans. *J Nucl Med*. 2018;59(3):516-522. doi:10.2967/JNUMED.117.190546

18. Salem V, Izzi-Engbeaya C, Coello C, et al. Glucagon increases energy expenditure independently of brown adipose tissue activation in humans. *Diabetes, Obes Metab.* 2016;18(1):72-81. doi:10.1111/DOM.12585
19. Martínez-Tellez B, Perez-Bey A, Sanchez-Delgado G, et al. Concurrent validity of supraclavicular skin temperature measured with iButtons and infrared thermography as a surrogate marker of brown adipose tissue. *J Therm Biol.* 2019;82:186-196. doi:10.1016/J.JTHERBIO.2019.04.009
20. Hu HH, Perkins TG, Chia JM, Gilsanz V. Characterization of human brown adipose tissue by chemical-shift water-fat MRI. *Am J Roentgenol.* 2013;200(1):177-183. doi:10.2214/AJR.12.8996
21. Van Rooijen BD, Van Der Lans AAJJ, Brans B, et al. Imaging cold-activated brown adipose tissue using dynamic T2*-Weighted magnetic resonance imaging and 2-deoxy-2-[18F]fluoro-d-glucose positron emission tomography. *Invest Radiol.* 2013;48(10):708-714. doi:10.1097/RLI.0b013e31829363b8
22. McCallister A, Zhang L, Burant A, Katz L, Branca RT. A pilot study on the correlation between fat fraction values and glucose uptake values in supraclavicular fat by simultaneous PET/MRI. *Magn Reson Med.* 2017;78(5):1922-1932. doi:10.1002/mrm.26589
23. Fischer JGW, Maushart CI, Becker AS, et al. Comparison of [18F]FDG PET/CT with magnetic resonance imaging for the assessment of human brown adipose tissue activity. *EJNMMI Res.* 2020;10(1):1-12. doi:10.1186/S13550-020-00665-7/TABLES/2
24. Sun L, Verma S, Michael N, et al. Brown Adipose Tissue: Multimodality Evaluation by PET, MRI, Infrared Thermography, and Whole-Body Calorimetry (TACTICAL-II). *Obesity.* 2019;27(9):1434-1442. doi:10.1002/oby.22560
25. Karampinos DC, Weidlich D, Wu M, Hu HH, Franz D. Techniques and Applications of Magnetic Resonance Imaging for Studying Brown Adipose Tissue Morphometry and Function. *Handb Exp Pharmacol.* 2019;251:299-324. doi:10.1007/164_2018_158
26. Wu M, Junker D, Branca RT, Karampinos DC. Magnetic Resonance Imaging Techniques for Brown Adipose Tissue Detection. *Front Endocrinol (Lausanne).* 2020;11:421. doi:10.3389/FENDO.2020.00421/FULL
27. Coolbaugh CL, Damon BM, Bush EC, Welch EB, Towse TF. Cold exposure induces dynamic, heterogeneous alterations in human brown adipose tissue lipid content. *Sci Rep.* 2019;9(1):13600. doi:10.1038/s41598-019-49936-x
28. Stahl V, Maier F, Freitag MT, et al. In vivo assessment of cold stimulation effects on the fat fraction of brown adipose tissue using DIXON MRI. *J Magn Reson Imaging.* 2017;45(2):369-380. doi:10.1002/jmri.25364
29. Lundström E, Strand R, Johansson L, Bergsten P, Ahlström H, Kullberg J. Magnetic resonance imaging cooling-reheating protocol indicates decreased fat fraction via lipid consumption in suspected brown adipose tissue. *PLoS One.* 2015;10(4). doi:10.1371/journal.pone.0126705
30. Deng J, Neff LM, Rubert NC, et al. MRI characterization of brown adipose tissue under thermal challenges in normal weight, overweight, and obese young men. *J Magn Reson Imaging.* 2018;47(4):936-947. doi:10.1002/jmri.25836
31. Oreskovich S, Ong F, Ahmed B, et al. Magnetic resonance imaging reveals human brown adipose tissue is rapidly activated in response to cold. *J Endocr Soc.* October 2019. doi:10.1210/2019-00309
32. u Din M, Raiko J, Saari T, et al. Human brown adipose tissue [15O]O₂ PET imaging in the presence and absence of cold stimulus. *Eur J Nucl Med Mol Imaging.* 2016;43(10):1878-1886. doi:10.1007/s00259-016-3364-y
33. Neves EB, Vilaça-Alves J, Regina I, et al. Influence of Subcutaneous Fat Layer in Skin Temperature. *Motricidade.* 2016;11(4):120-126. doi:10.6063/motricidade.5999

34. Gashi G, Madoerin P, Maushart CI, et al. MRI characteristics of supraclavicular brown adipose tissue in relation to cold-induced thermogenesis in healthy human adults. *J Magn Reson Imaging*. 2019;50(4):1160-1168. doi:10.1002/jmri.26733
35. Chen KY, Cypess AM, Laughlin MR, et al. Brown Adipose Reporting Criteria in Imaging Studies (BARCIST 1.0): Recommendations for Standardized FDG-PET/CT Experiments in Humans. *Cell Metab*. 2016;24(2):210-222. doi:10.1016/j.cmet.2016.07.014



Chapter 7

List of abbreviations

Nederlandse samenvatting

List of publications

Curriculum vitae



7.1 LIST OF ABBREVIATIONS

[¹⁸F]FDG: ¹⁸F-fluorodeoxyglucose
ASHRAE: American society of heating, refrigerating, and air-conditioning engineers
ATP: adenosine triphosphate
BAT: brown adipose tissue
BMI: body mass index
BSA: body surface area
cAMP: cyclic adenosine monophosphate
CIT: cold induced thermogenesis
DEXA: dual energy x-ray absorptiometry
FA: fatty acid
FATP: fatty acid transporter
FF_{Glob}: global fat fraction
FF_{Loc}: local fat fraction
FF_{SAT}: subcutaneous white adipose tissue fat fraction
FF: fat fraction
FM: fat mass
GLUT: glucose transporter
HU: Hounsfield units
IRT: infrared thermography
LM: lean mass
MRI: magnetic resonance imaging
MSE: mean squared error
NE: norepinephrine
NRS: numeric rating scale
NST: non-shivering thermogenesis
PET-CT: positron emission tomography – computed tomography
PKA: protein kinase A
ROI: Region of interest
scBAT: supraclavicular brown adipose tissue
SUV: standardized uptake value
T2*_{Glob}: global T2*
T2*_{Loc}: local T2*
UCP-1: uncoupling protein 1
WAT: white adipose tissue

7.2 NEDERLANDSE SAMENVATTING

Bruin vet is een beperkte hoeveelheid weefsel dat zich vooral in de nek en langs de grote vaten bevindt en dat vetten en glucose kan verbranden tot warmte. In pasgeborenen speelt bruin vet een cruciale rol bij het behoud van de kerntemperatuur van het lichaam. Pasgeborenen hebben namelijk onvoldoende spiermassa waardoor ze niet kunnen rillen en een hoge lichaamsoppervlak- lichaamsgewicht ratio wat leidt tot snel warmteverlies.

Studies hebben aangetoond dat bruin vet ook actief is in volwassenen¹⁻³. Door het unieke vermogen om energie uit vetten en glucose om te zetten in warmte wordt bruin vet activatie gezien als een veelbelovende behandeling tegen obesitas en hart- en vaatziekten. Het is aangetoond dat bruin vet activiteit gerelateerd is aan de insulinegevoeligheid⁴ en een betere cardiometabole gezondheid^{5,6}.

De fysiologische stimulus voor bruin vet activatie is blootstelling aan kou. Na activatie wordt bruin vet vaak gemeten met behulp van de beeldvormingstechniek: Fluor-18 fluordeoxyglucose positronemissietomografie/computertomografie ($[^{18}\text{F}]\text{FDG}$ PET-CT) waarbij de opname van glucose in het bruin vet depot in kaart kan worden gebracht. Een nadeel van deze methode is echter het gebruik van schadelijke straling. De methode is ook invasief en onderschat bruin vet activiteit wanneer deelnemers insulineresistent zijn. Daarnaast wordt de glucoseopname gemeten met $[^{18}\text{F}]\text{FDG}$ PET-CT terwijl bruin vet voornamelijk vetten verbrandt⁷. Een grote limitatie binnen het klinisch onderzoek naar bruin vet is dus dat er geen gouden standaard beschikbaar is.

Het hoofddoel van dit proefschrift is het verbeteren van huidige technieken voor het meten van bruin vet activiteit in volwassenen om vervolgstudies naar bruin vet en ontwikkelingen van activerende strategieën te bevorderen. In de eerste instantie wilden wij de rol van de lichaamssamenstelling en bruin vet activiteit op de tolerantie voor kou onderzoeken, zodat dit meer inzichten zou kunnen bieden voor verdere optimalisatie van koelingsprotocollen. Vervolgens hebben wij ons gefocust op het optimaliseren van non-invasieve en veiligere technieken dan $[^{18}\text{F}]\text{FDG}$ PET-CT, zoals infrarood thermografie (IRT) en beeldvorming door magnetische resonantie (MRI). IRT is een techniek die de temperatuur van de huid afbeeldt waarbij gebruik wordt gemaakt van een infrarood camera. Aangezien bruin vet warmte produceert wordt deze methode gebruikt voor het meten van de huidtemperatuur rondom het bruin vet depot. MRI is een beeldvormingstechniek waarmee de organen in het lichaam zichtbaar kunnen worden gemaakt door een combinatie van een sterk magnetisch veld en radiogolven. De Dixon methode is een MRI techniek die de relatieve hoeveelheid vet afbeeldt in het lichaam. Deze MRI uitkomstmaat wordt de vetfractie genoemd en heeft een waarde tussen de 0% en 100%. De vetfractie wordt gebruikt

in MRI onderzoek naar bruin vet omdat een vetfractie afname na blootstelling aan kou mogelijk de verbranding van vetten weerspiegelt.

In **hoofdstuk 2** hebben we eerst onderzoek gedaan naar het verband tussen de tolerantie tegen kou en de lichaamssamenstelling waaronder bruin vet. Deelnemers gaven zelf aan wanneer ze rilden tijdens gepersonaliseerde blootstelling aan kou. Om bruin vet zo optimaal mogelijk te activeren, werden deelnemers gekoeld bij een temperatuur die 4°C hoger was dan de temperatuur waarbij deelnemers begonnen te rillen. Het rilpunt werd gebruikt als een maat voor de tolerantie tegen kou en is gedefinieerd als de verstreken tijd waarbij deelnemers begonnen met rillen. De resultaten van dit hoofdstuk laten zien dat de lichaamsgrootte en -samenstelling gerelateerd zijn aan het rilpunt terwijl bruin vet activiteit geen invloed lijkt te hebben voor de tolerantie tegen kou. Doordat het rilpunt gebruikt wordt als een referentiemaat voor optimale bruin vet activatie, is het van belang dat deelnemers een vergelijkbare intensiteit aan kou ondervinden. Indien dit niet het geval is, zou de detectie van bruin vet minder gevoelig kunnen worden vanwege onvoldoende stimulatie. Aangezien bruin vet therapie voornamelijk gericht is op individuen met overgewicht of obesitas, zouden de lichaamsgrootte en samenstelling dus overwogen moeten worden voor optimale bruin vet activatie.

In de volgende hoofdstukken hebben we ons gefocust op non-invasieve en veilige beeldvormingsmodaliteiten zoals IRT (hoofdstuk 3) en MRI (**hoofdstuk 4** en **hoofdstuk 5**). In **hoofdstuk 3** hebben wij ons gericht op het optimaliseren van huidtemperatuur analyses in het bruin vet dat zich net boven de sleutelbeenderen bevindt (het zogenaamde supraclaviculaire gebied). De eerste stap in het analyseren van de huidtemperatuur in het supraclaviculaire gebied is het intekenen van een *region of interest* (ROI) om het supraclaviculaire gebied af te bakenen van omliggende weefsels. De temperatuurwaarden binnen de ROI worden vervolgens gebruikt om de maximale of gemiddelde temperatuur in het bruin vet te bepalen. De analyse kan veel tijd kosten als de dataset van een deelnemer uit meerdere IRT beelden bestaat, omdat de ROI op elk plaatje handmatig moeten worden ingetekend. Wij hebben daarom een methode (de IRT-toolbox) ontwikkeld om op een efficiëntere manier de activiteit van bruin vet te analyseren. De belangrijkste kenmerken van de IRT-toolbox zijn beeldtranslatie en non-rigide beeldregistratie die resulteren in een volledige overlap tussen een referentieplaatje (bijv. het eerste plaatje in een dataset) en de resterende plaatjes in de dataset. Onze resultaten laten zien dat de ROI intekentijd aanzienlijk verkort kan worden met de IRT-toolbox en dat de temperaturen in het bruin vet depot vergelijkbaar zijn met handmatig analyses. De software kan kosteloos worden gedownload (https://github.com/AashleySD/IRT_toolbox) en is beschikbaar voor klinische applicaties.

Alhoewel IRT makkelijker in gebruik is en veel goedkoper is dan PET-CT, kan de gemeten huidtemperatuur worden beïnvloed door de onderhuidse vetlaag waardoor deze methode niet geheel betrouwbaar is in individuen met overgewicht⁸. Daarnaast is het niet mogelijk om het bruin vet volume te meten omdat de thermale camera tweedimensionale beelden maakt. In de laatste twee hoofdstukken van dit proefschrift hebben we ons daarom gericht op MRI vetfractie metingen als een mogelijk alternatief voor [¹⁸F]FDG PET-CT. In het supraclaviculaire gebied in volwassenen is er geen duidelijke scheiding tussen bruin vet en ander weefsel, zoals wit vet, spieren en bloedvaten. In **hoofdstuk 4** hebben wij geprobeerd om het bruin vet zo optimaal mogelijk van andere weefsels te scheiden door verschillende vetfractie drempelwaarden (bijv. 30-100%) toe te passen om weefsels met een lage vetfractie, zoals spieren en bloedvaten en een hoge vetfractie zoals wit vet uit te sluiten van de analyse. We hebben laten zien dat de vetfractie na koelen van het lichaam tot de riltemperatuur voornamelijk afnam in vetrijke gebieden waarbij de vetfractie in deze gebieden varieerde tussen de 70% en 100%, terwijl de vetfractie toenam op plekken waar aanvankelijk minder vet aanwezig was en de vetfractie op die plekken varieerde tussen de 30% en 70%. Daarnaast hebben we laten zien dat bij hogere drempelwaarden (bijvoorbeeld 30-100% → 50-100%), de vetfractieveranderingen ten gevolge van blootstelling aan kou kleiner werden. Op basis van onze resultaten raden wij daarom aan om een vetfractiebereik van 30-100% te hanteren voor het analyseren van de vetfractie om te voorkomen dat de mogelijke mate van bruin vetactivatie onderschat zal worden.

De consequente afname van de vetfractie van bruin vet na kou in de literatuur en resulterend uit **hoofdstuk 4** is veelbelovend voor de toepassing van MRI in bruin vet onderzoek^{9,10}. Voor klinisch onderzoek naar bruin vet en ontwikkeling van activatie strategieën zou het echter nuttig zijn om meer inzicht te krijgen in de tijdsverloop van bruin vet activiteit. Daarnaast bevindt bruin vet zich in het supraclaviculaire gebied net boven de sleutelbeenderen waardoor vetfractiemetingen beïnvloed kunnen worden door beweging van het lichaam. Door gebruik te maken van technieken als beeldregistratie en geoptimaliseerde segmentatiemethoden gebaseerd op de bevindingen uit **hoofdstuk 4**, hebben we in **hoofdstuk 5** aangetoond dat het mogelijk is om supraclaviculaire vetfractieveranderingen te meten met een relatief lage variabiliteit (<0.1%) in opeenvolgende meetmomenten. In dit hoofdstuk hebben wij ook aangetoond dat er mogelijk eerst opname van vetten plaatsvindt voordat de vetten worden verbrand. In een vervolgstudie zal worden bepaald of de vetfractieveranderingen tijdens koelen gerelateerd zijn aan stofwisselingswaarden gemeten in bloed. Aangezien geactiveerd bruin vet vetten aanvult voor verbranding, zouden vetfractieveranderingen mogelijk gerelateerd kunnen zijn aan veranderingen in plasmalipidenwaarden. Vervolgstudies zouden zich daarom kunnen richten op het verband tussen de vetfractie en stofwisselingswaarden ter validatie van de MRI vet fractie als uitkomstmaat in bruin vet onderzoek.

De centrale bevindingen uit dit proefschrift hebben bijgedragen aan de ontwikkeling en bevordering van niet-invasieve technieken voor het meten van bruin vet in klinisch onderzoek. In **hoofdstuk 2** hebben wij aangetoond dat de lichaamsgrootte en -samenstelling overwogen zouden moeten worden bij het toepassen van koelingsprotocollen, zodat de mate van BAT activatie en BAT detectie minimaal afhankelijk zijn van interindividuele verschillen in de mate van de tolerantie tegen kou. In **hoofdstukken 3** en **5** hebben wij laten zien dat technieken zoals non-rigide beeldregistratie, de analysetijd aanzienlijk kan verkorten en de variabiliteit van vetfractiemetingen verlaagt. In **hoofdstuk 4** hebben wij ons gericht op het segmenteren van het bruin vet depot op MRI vetfractieplaatjes om de vet fractie veranderingen beter in te schatten. Wij hebben laten zien dat de vetfractieveranderingen door het gehele bruin vet depot plaatsvinden en dat het depot erg heterogeen is. De vetfractie drempelwaarden voor het segmenteren van het supraclaviculaire bruin vet depot zou dus zorgvuldig uitgekozen moeten worden aangezien de MRI uitkomstmaten voor bruin vet activiteit kunnen variëren.

REFERENTIES

1. Cypess AM, Lehman S, Williams G, et al. Identification and importance of brown adipose tissue in adult humans. *N Engl J Med*. 2009;360(15):1509-1517. doi:10.1056/NEJMoa0810780
2. Van Marken Lichtenbelt WD, Vanhommerig JW, Smulders NM, et al. Cold-activated brown adipose tissue in healthy men. *N Engl J Med*. 2009;360(15):1500-1508. doi:10.1056/NEJMoa0808718
3. Virtanen KA, Lidell ME, Orava J, et al. Functional Brown Adipose Tissue in Healthy Adults. *N Engl J Med*. 2009;360(15):1518-1525. doi:10.1056/nejmoa0808949
4. Hanssen MJW, Hoeks J, Brans B, et al. Short-term cold acclimation improves insulin sensitivity in patients with type 2 diabetes mellitus. *Nat Med*. 2015;21(8):863-865. doi:10.1038/nm.3891
5. Oikonomou EK, Antoniadou C. The role of adipose tissue in cardiovascular health and disease. *Nat Rev Cardiol*. 2019;16(2):83-99. doi:10.1038/s41569-018-0097-6
6. Becher T, Palanisamy S, Kramer DJ, et al. Brown adipose tissue is associated with cardiometabolic health. *Nat Med*. 2021;27(1):58-65. doi:10.1038/S41591-020-1126-7
7. Schilperoort M, Hoeke G, Kooijman S, Rensen PCN. Relevance of lipid metabolism for brown fat visualization and quantification. *Curr Opin Lipidol*. 2016;27(3):242-248. doi:10.1097/MOL.0000000000000296
8. Neves EB, Vilaça-Alves J, Nogueira IRA, Reis VMH. Influence of Subcutaneous Fat Layer in Skin Temperature. *Motricidade*. 2015;11(4):120-126. doi:10.6063/MOTRICIDADE.5999
9. Karampinos DC, Weidlich D, Wu M, Hu HH, Franz D. Techniques and Applications of Magnetic Resonance Imaging for Studying Brown Adipose Tissue Morphometry and Function. *Handb Exp Pharmacol*. 2019;251:299-324. doi:10.1007/164_2018_158
10. Wu M, Junker D, Branca RT, Karampinos DC. Magnetic Resonance Imaging Techniques for Brown Adipose Tissue Detection. *Front Endocrinol (Lausanne)*. 2020;11:421. doi:10.3389/FENDO.2020.00421/FULL

7.3 LIST OF PUBLICATIONS

In 2019

1. Nahon KJ, Janssen LGM, **Sardjoe Mishre ASD**, Bilsen MP, van der Eijk JA, Botani K, Overduin LA, Ruiz JR, Burakiewicz J, Dzyubachyk O, Webb AG, Kan HE, Berbée JFP, van Klinken JB, van Dijk KW, van Weeghel M, Vaz FM, Coskun T, Jazet IM, Kooijman S, Martinez-Tellez B, Boon MR, Rensen PCN. The effect of mirabegron on energy expenditure and brown adipose tissue in healthy lean South Asian and European men. *Diabetes, Obesity and Metabolism*. 2020 Nov;22(11):2032-2044. doi: 10.1111/dom.14120.

In 2020

2. Janssen LGM, Nahon KJ, Bracké KFM, van den Broek D, Smit R, **Sardjoe Mishre ASD**, Koorneef LL, Martinez-Tellez B, Burakiewicz J, Kan HE, van Velden FHP, Pereira Arias-Bouda LM, de Geus-Oei LF, Berbée JFP, Jazet IM, Boon MR, Rensen PCN. Twelve weeks of exenatide treatment increases [¹⁸F]fluorodeoxyglucose uptake by brown adipose tissue without affecting oxidative resting energy expenditure in nondiabetic males. *Metabolism*. 2020 May;106:154167. doi: 10.1016/j.metabol.2020.154167.

3. Abreu-Vieira G, **Sardjoe Mishre ASD**, Burakiewicz J, Janssen LGM, Nahon KJ, van der Eijk JA, Riem TT, Boon MR, Dzyubachyk O, Webb AG, Rensen PCN, Kan HE. Human Brown Adipose Tissue Estimated With Magnetic Resonance Imaging Undergoes Changes in Composition After Cold Exposure: An in vivo MRI Study in Healthy Volunteers. *Frontiers in Endocrinology*. 2020 Jan 9;10:898. doi: 10.3389/fendo.2019.00898.

4. Nahon KJ, Janssen LGM, **Sardjoe Mishre ASD**, Bilsen MP, van der Eijk JA, Botani K, Overduin LA, Ruiz JR, Burakiewicz J, Dzyubachyk O, Webb AG, Kan HE, Berbée JFP, van Klinken JB, van Dijk KW, van Weeghel M, Vaz FM, Coskun T, Jazet IM, Kooijman S, Martinez-Tellez B, Boon MR, Rensen PCN. The effect of mirabegron on energy expenditure and brown adipose tissue in healthy lean South Asian and European men. *Diabetes, Obesity and Metabolism*. 2020 Nov;22(11):2032-2044. doi: 10.1111/dom.14120.

In 2021

5. van de Velde NM, Hooijmans MT, **Sardjoe Mishre ASD**, Keene KR, Koeks Z, Veeger TTJ, Alleman I, van Zwet EW, Beenakker JM, Verschuuren JJGM, Kan HE, Niks EH. Selection Approach to Identify the Optimal Biomarker Using Quantitative Muscle MRI and Functional Assessments in Becker Muscular Dystrophy. *Neurology*. 2021 Aug 3;97(5):e513-e522. doi: 10.1212/WNL.0000000000012233.

6. Naarding KJ, Keene KR, **Sardjoe Mishre ASD**, Veeger TTJ, van de Velde NM, Prins AJ, Burakiewicz J, Verschuuren JJGM, van der Holst M, Niks EH, Kan HE. Preserved thenar

muscles in non-ambulant Duchenne muscular dystrophy patients. *Journal of Cachexia, Sarcopenia and Muscle*. 2021 Jun;12(3):694-703. doi: 10.1002/jcsm.12711.

In 2022

7. **Sardjoe Mishre ASD**, Martinez-Tellez B, Acosta FM, Sanchez-Delgado G, Straat ME, Webb AG, Kan HE, Rensen PCN, Ruiz JR. Association of shivering threshold time with body composition and brown adipose tissue in young adults. *Journal of Thermal Biology*. 2022 Aug;108:103277. doi: 10.1016/j.jtherbio.2022.103277.

8. Straat ME, Martinez-Tellez B, **Sardjoe Mishre ASD**, Verkleij MMA, Kemmeren M, Pelsma ICM, Alcantara JMA, Mendez-Gutierrez A, Kooijman S, Boon MR, Rensen PCN. Cold-Induced Thermogenesis Shows a Diurnal Variation That Unfolds Differently in Males and Females. *The Journal of Clinical Endocrinology and Metabolism*. 2022 May 17;107(6):1626-1635. doi: 10.1210/clinem/dgac094.

9. **Sardjoe Mishre ASD**, Straat ME, Martinez-Tellez B, Mendez Gutierrez A, Kooijman S, Boon MR, Dzyubachyk O, Webb A, Rensen PCN, Kan HE. The Infrared Thermography Toolbox: An Open-access Semi-automated Segmentation Tool for Extracting Skin Temperatures in the Thoracic Region including Supraclavicular Brown Adipose Tissue. *Journal of Medical Systems*. 2022 Nov 2;46(12):89. doi: 10.1007/s10916-022-01871-7.

7.4 CURRICULUM VITAE

Aashley Siromeni Devi Sardjoe Mishre was born on the 2nd of February 1995, and grew up in The Hague, the Netherlands. After graduating from Lyceum Ypenburg in the Hague in 2013, she continued with the bachelor medical natural sciences at the Vrije Universiteit van Amsterdam. After obtaining her bachelor's degree, she studied the research master medical natural sciences and she chose the medical physics track. As part of her master, she followed internships at the VU medical center and Philips. After finishing her master in July 2018, Aashley started her PhD training at the Leiden University Medical Center at the department of Radiology and the division of Endocrinology at the department of Medicine. During her PhD project, she focused on improving the methodology for studying supraclavicular brown adipose tissue (BAT) activity in human adults. Her findings provided further insight into the role of BAT and body composition during cold exposure in human adults, as well as the development of non-invasive methods to improve the reliability of supraclavicular BAT assessments.

7.4 CURRICULUM VITAE

Aashley Siromeni Devi Sardjoe Mishre was born on the 2nd of February 1995, and grew up in The Hague, the Netherlands. After graduating from Lyceum Ypenburg in the Hague in 2013, she continued with the bachelor medical natural sciences at the Vrije Universiteit van Amsterdam. After obtaining her bachelor's degree, she studied the research master medical natural sciences and she chose the medical physics track. As part of her master, she followed internships at the VU medical center and Phillips. After finishing her master in July 2018, Aashley started her PhD training at the Leiden University Medical Center at the department of Radiology and the division of Endocrinology at the department of Medicine. During her PhD project, she focused on improving the methodology for studying supraclavicular brown adipose tissue (BAT) activity in human adults. Her findings provided further insight into the role of BAT and body composition during cold exposure in human adults, as well as the development of non-invasive methods to improve the reliability of supraclavicular BAT assessments.

7.5 DANKWOORD

Graag wil ik iedereen bedanken die heeft meegewerkt aan dit proefschrift. Ik ben erg dankbaar voor de fijne samenwerking binnen de afdeling Radiologie en de sectie Endocrinologie van de afdeling Interne Geneeskunde. Ik wil alle proefpersonen bedanken voor hun deelname aan de studies. Zonder hun deelname waren de studies in dit proefschrift niet mogelijk geweest. Ik wil mijn copromotor Hermien Kan en promotoren Andrew Webb en Patrick Rensen bedanken voor de begeleiding, ondersteuning en ervaring die ik heb opgedaan tijdens mijn PhD traject. Ik wil graag al mijn collega's bedanken voor de leuke en gezellige tijd in het LUMC alsmede de wetenschappelijke ondersteuning. Tenslotte wil ik mijn ouders (Premood & Sandra), mijn zus en zwager (Maresha & Satiesh), mijn nichtje en neefje (Soedharseni & Avinesh) en mijn man Wiresh, bedanken voor de steun, motivatie en liefde.

